論文 / 著書情報
Article / Book Information

題目(和文)	
Title(English)	The unsteady flow field induced by tidal action and its effect on sedimentation in the Yangtze Estuarine Channel
著者(和文)	ｵｳﾁｮｳｷｮｳ
Author(English)	Zhangjiao Wang
出典(和文)	学位:博士(工学), 学位授与機関:東京工業大学, 報告番号:甲第9307号, 授与年月日:2013年9月25日, 学位の種別:課程博士, 審査員:石川 忠晴,山中 浩明,木内 豪,中村 恭志,浅輪 貴史
Citation(English)	Degree:Doctor (Engineering), Conferring organization: Tokyo Institute of Technology, Report number:甲第9307号, Conferred date:2013/9/25, Degree Type:Course doctor, Examiner:,,,,
学位種別(和文)	博士論文
Type(English)	Doctoral Thesis

The unsteady flow field induced by tidal action and its effect on sedimentation in the Yangtze Estuarine Channel

Doctoral Dissertation

WANG Zhangjiao

Supervisor: ISHIKAWA Tadaharu

2013

Department of Environmental Science and Technology

Interdisciplinary Graduate School of Science and Engineering

Tokyo Institute of Technology

Abstract

The Yangtze River is one of the largest rivers in the world, carrying large amount of fresh water and fine sediment. The estuarine topography is complicated including meandering thalweg and a number of large shoals. This reach is strongly influenced by the tide, because of the large tidal range and gentle river bed slope. The flow field is highly unsteady with obvious cross-sectional flow, which is supposed to be the main control factor in sediment transport. The flow field has seasonal characteristics due to the variation in flow rate. However, due to the difficulty in systematic observation, the tidal influence on sediment transport and its seasonal characteristic has not been well understood. Therefore, the objective of this study is to understand the relationship between sediment transport and its control factors by using numerical experiments.

The present study was composed by two parts. The first part (Chapter 2 and 3) mainly focus on the tidal influence to the flow field and sediment transport in flood season, when the tidal effect the weakest in a year. The flow field is reproduced by a quasi-3D model, and a tracer experiment is designed to exhibit the characteristics of suspended sediment transport. The calculation result suggested that the flow field is highly pulsatile with remarkable cross-sectional component above the underwater shoals. The bed sediment is suspended in thalweg and transport to downstream in maximum ebb, and deposit on the shoals in high water slack when the flow is in stagnation. This fact suggested the development of meandering thalweg in flood season.

The second part (Chapter 4 and 5) mainly focus on the different characteristics of flow structure and the corresponding topographic change by the changes of flow rate. A 2DH model on the base of unstructured triangular mesh system is used to modeling the topography change process, and the total sediment load is used to calculate the sediment transport rate. The calculation result suggested that in dry season with the stronger reverse flow, the sediment transport is seaward in thalweg and landward above the underwater shoals. The sandspits develop at the edge of underwater shoals. This small scale topography feature further develops in the subsequent seasons and changes the flow field entirely, which can also be found in the historical recorded collected from references.

The present study provided a new explanation on the topographic change process in the Yangtze Estuarine channel. The numerical experiments were proved to be an efficient way to clarify the flow structure and resulting sediment transport in detail. The results implied that the small-scale sandspits developed during the dry season may be a key point in topographic change process in this channel.

Contents

Chapter 1 Introduction

1.1 Research background

Estuarine channel is a part of river estuary, serving as a connection of river and open sea. The morphology of estuarine channel is similar to the river, which is restricted by the side banks. Normally, the estuarine channel is influenced by the tide. The topography changes frequently and anabranch channels develop. The estuarine channel may or may not be influenced by the salty water intrusion, depending on the interaction of flow rate and tide.

Estuarine channel locates at the transition zone between river environment and ocean environment. It is one of the most productive regions of the world, not only referring to the abundant biological diversity, but also the social and economic importance for human being. Of the 32 largest cities in the world, 22 are located on navigable estuaries, serving as shipping centers and financial centers (Ross, 1995). For the convenience of navigation, the channel needs to be stable and keep the depth for a certain degree. However, due to the interaction of flow rate and tide, the sediment transport process in the estuarine channel is always unstable and fickle. The topography changes frequently with the alternation of flood-ebb channel and shoals, which interferes the development of navigation.

The above mentioned conflict appears obvious in the case of Yangtze Estuarine Channel. It is one of the several rivers with good navigation condition, so called “Golden waterway”, in which the 10,000 ton ships can go directly to Nanjing. The nearby city Shanghai is one of the economic centers of China on the base of navigation since 19th century. Meanwhile, the Yangtze Estuarine Channel is also suffered from the estuarine processes. That is: the existence of mouth bars, the insufficient depth of waterway, the frequently change of river channel and underwater shoals, which threaten the stability of navigation channel profoundly. Therefore, in order to reconcile the conflict of natural estuarine processes and human activities such as navigation and harbor siting, the proper management should be applied to maintain the sustainable exploitation of the Yangtze Estuarine Channel. And the understanding of natural estuarine processes by the interaction of flow rate and tide is the basic premise for the management.

However, the understanding of sediment transport process under the condition of unsteady tide is still limited in the Yangtze Estuarine Channel, because of its complexity and because it

involves a wide range of temporal and spatial scales. In spatial scale, the reach is so huge that systematic field observations on channel morphology cannot be applied frequently. Till now, the studies on morphology evolution of Yangtze Estuarine Channel is mainly derived from the inference by limited field observations, comparison of nautical maps with 5-10 years interval and text descriptions in the almanacs (Chen et al, 1988; Yun, 2004; Wang, 2008). In the temporal scale, periodical fluctuation of hydrological condition is obvious (including daily change of tide and seasonal change of flow rate) in the Yangtze Estuarine Channel. The complexity of morphology evolution in temporal scale is hard to be exposed by traditional methods. New methods should be introduced to handle the above mentioned difficulties in both temporal and special scales. In the present study, the numerical simulation is challenged in this field, trying to analyze the relationship between morphology evolution and hydrological condition of flow rate and tide. The result of analysis is compared to the historical topography records to make sure it is not conflict with each other.

1.2 Existing study review

The same as the other water environment, the morphology evolution in estuarine is also controlled by the sediment transport in flow (Guo and Jin, 1999). Normally, at the aspect of methodology, the study on sediment transport can be divided into observation and numerical simulation. At the aspect of spatial scale, it can be roughly divided into experimental channel, small river system and large river system. Although both the latter two refer to the real condition, due to the complexity in topography and uncertainty in hydrological condition, the research methodology and understanding of sediment transport in the large river system is completely different from the small river system.

1.2.1 Sediment transport process

Although the study on sediment transport related to irrigation channel can be traced to ancient China, Mesopotamia, Egypt and Roman Empire, the modern research on sediment transport process is started from the observations on physical process in experimental channels, due to its

controllable condition and simplified morphology. According to van Rijn, 1993, the first modern researcher was DuHuat (1734-1809) in France. He compared the resistance of various soil materials (clay to stone) by experiments, and proposed the first shear-resistance concept. The framework of modern sediment transport theory is formed about 80 years ago, contributed by Shields, Rouse, Kalinske, and Einstain. They established several empirical equations to describe the relationship of flow and sediment by numerous laboratory experiments.

i.e., Shields (1936) defined the critical bed-shear stress for the initiation of motion of sediment particles. The curve proposed is well known as the "Shields curve".

$$\tau_{*c} = func\left(R_{e*c}\right) \tag{1.1}$$

$$\tau_{*} \equiv \frac{u_{*}^{2}}{(\sigma/\rho - 1)gd}; \quad R_{e*} \equiv \frac{u_{*}d}{\nu} \tag{1.2}$$

where τ_* and τ_{*c} are shear stress and critical shear stress, respectively; R_{e*} and R_{e*c} are particle Reynolds number and critical particle Reynolds number, respectively; u_* is shear velocity; σ and ρ are density of sediment and fluid; g is gravitational acceleration; d is sediment particle diameter; ν is fluid kinematic viscosity.

Rouse (1937) established the vertical distribution of suspended sediment concentration, which is a relative value on the base of bottom concentration of suspended sediment at a reference level a.

$$\frac{c}{C_a} = \left(\frac{h-z}{z}\frac{a}{h-a}\right)^{Z} \tag{1.3}$$

where c is sediment concentration; C_a is bottom concentration at the reference level a; h is water depth; z is height from river bed; Z is fluid and sediment mixing coefficient $Z=w_0/\beta\kappa u_*$; w_0 is settling velocity; β describe the difference between the diffusion of fluid and the discrete of sediment; κ is Kármán constant.

Lane・Kalinske (1939) estimated the bottom concentration of suspended sediment by the rate of settling velocity and shear velocity.

$$C_a = 5.55\Delta F(w_0)\left[\frac{1}{2}\left(\frac{u_*}{w_0}\right)\exp\left\{-\left(\frac{w_0}{u_*}\right)^2\right\}\right]^{1.61} \tag{1.4}$$

where $\Delta F(w_0)$ is the percentage of the particle with the settling velocity w_0 in bed material.

Einstein (1950) synthesized the bed-load movement and suspended movement. The bed-load discharge is calculated by shear stress, while the bottom concentration of suspended sediment can be calculated by assuming the velocity of bed-load movement is $11.6u_*$.

$$q_b = 8(\tau_* - 0.047)^{1.5}\sqrt{(\sigma/\rho - 1)gd^3} \tag{1.5}$$

$$C_a = \frac{q_b}{11.6u_* a} \tag{1.6}$$

where q_b is volume bed-load transport rate per unit width; a is height of reference level, which is set to be twice of the grain size $a=2d$.

On the base of their contributions, numerous researchers validate, modify and develop the theories by applying these equations to real rivers or experimental channels in different scales. A variety of empirical expressions have been proposed. In the bed-load transport, we have Meyer-Peter and Muller equation (1948), Ashida・Michiue equation (1972), van Rijn equation (1984). In the suspended load transport, we have Ashida・Michiue equation (1970), Itakura・Kisi equation (1980), Ashida, Okabe and Fujida equation (1982), van Rijn equation (1984). In the total sediment transport, which combine the bed-load and suspended load, we have Einstein equation (1942), Laursen equation (1958) and Yoshikawa・Ishikawa equation (1978) (Ashida and Michiue 1970, Ashida, Okabe and Fujida, 1982, Japan Society of Civil Engineers 1999, Garcia and Parker, 1991). Although these equations are differ with each other, they have similar trend and most of them use the rate of settling velocity w_0 and shear velocity u_* to evaluate sediment transport rate.

By applying these equations, the morphology change of channel is possible to be simulated. If the river bank is fixed, the erosion and deposition occurs with regular interval. The alternating bars develop, and transport to downstream (Simizu et al, 1987). If bank erosion is considered, the phenomenon that erosion at concave bank and deposition at convex bank occurs, the meandering channel develops (Duan et al, 2001). These studies obtained good results in the morphology change of river system with uni-direction flow. They are rarely applied in the estuarine study. The complexity of flow field and the scarce of available observational data for validation are supposed to be the main reason.

1.2.2 Estuaries in small river system

The morphological change studies on estuaries in small river system have been studied extensively in Japan and European countries. In these countries, the distances of most rivers are short and their drainage basins are quite small. So the flow rate at estuary area is very sensitive to the heavy rain events. The flood duration is short. The flooding flow rate may be several times higher than the normal one. Consequently, strong erosion occurs during these short-term flood events and fine sediment is flushed into the adjacent sea. When the flow rate returns to normal, the fine sediment moves back into the estuarine channel by the tidal pumping effect. The estuarine sediment transport process is mainly discussed separately from erosion with regard to flooding events, although sediment deposition continues long after the flood season has passed.

In Japan, the typical studies on flooding erosion include Chikugogawa River of 143km and Tone River of 322km. By long-term field observation on Chikugogawa River estuary, Yokoyama et al, 2005, 2006, 2008, 2010 and Irie et al, 2009 suggested: 1) the cohesive sediment at the estuarine channel is eroded and transported to Ariake Sea to deposite. 2) after the flood, the riverbed decrease 1-1.5m. Sand layer appears and sand wave can be observed. 3) after half a year with low flow rate, sandy bed will be covered by muddy layer about 1-2m thick. By sampling bed material before and after flood event, in Tone River Estuary, Siziki et al, 2003 suggested: 1) after a flood of 8000m^3/s, the bed material becomes sand; 2) three month after the flood event, the sandy bed is covered by fine silt and clay. Kobayashi et al 2010 proposed similar conclusion and suggests the small flooding event with high frequency have the same influence with one big flood event to coarser the bed material.

The tidal pumping effect to the sediment transport process is also studied in the above mentioned two rivers. The field observation in Chikugogawa River estuary by Yokoyama et al 2007, 2008, 2009 and Hiragawa et al, 2009 suggested: 1) tide induces landward suspended sediment (SS) movement. The concentration of SS in spring tide is 50 times larger than that of neap tide; 2) the flood tide carries SS to estuarine channel to deposit, especially in convex bank; The observation in Tone river estuary (Siziki et al, 2004 and Simizu et al, 2004) suggested the repeating cycle of re-suspension in ebb tide and deposition in flood tide induce the fine silt deposition with high water content. Other studies includes Shiragawa River (74km) estuary and

Tamagawa River (138km) estuary (Yokoyama et al 2001), Ohtagawa River (103km) estuary (Kawanisi et al, 2005), Rokkakugawa River (47km) estuary (Futawatari et al, 1992). They are all small river system and the landward deposition of fine sediment in observed by tidal pumping effect.

Besides, long-term observation includes flooding events on SS transport and topography change is also applied in Shiragawa River estuary and Ohtagawa River estuary. Uno et al 2002 discussed the long-term sediment budget and the morphologic change at the estuary area of Shiragawa River by yearly observation of turbidity, bed material analysis and topography change. But the tidal effect in flooding events did not been mentioned. The observation in Ohtagawa (Kawanisi, et al 2005) includes two flood events (about 3 days) in a month. But the peak flow rate is not large enough to reform the topography in the whole estuarine channel.

In other countries, the tide induced landward transport of sediment has been paid more attention in small river system. i.e. Vale and Sundby 1987 in the study of Tagus River (716km) estuary in Spanish, Lindsay et al 1996 in the study of Forth River (47km) Estuary in Scotland, Fugate et al 2007 in the study of Chesapeak River (322km) Estuary in USA, Baugh et al 2012, in the study of Thames River (346km) Estuary in England. A word of "tidal pumping" is created to describe the tide induced the near-bed landward sediment transport due to the asymmetry in the magnitude and duration of currents during flood and ebb tide. In their studies, the flow rate distribution does not show obvious peaks by flooding events. The above mentioned tidal pumping effect is regarded as the characteristics in normal flow rate.

In the countries other than Japan, the studies on flow rate impact are rare to be seen. Some field observations covered one or two flooding events. The observational data includes flow velocity and suspended sediment concentration (SSC) in the study of Dalaware River (484km) Estuary in USA (Cook et al, 2007) and the sediment core sampling in the study of Hudson River (507km) Estuary in USA (Woodruff et al, 2001). They suggested that bed sediment is flushed to downstream and deposit in flooding events; when flow rate return to normal levels sediment initially deposited downstream is re-suspended and transported back upstream by tidal pumping.

1.2.3 Estuaries in large river system

In the large river system, the drainage basin is very huge. One flooding event at certain location does not change much of the flow rate in the estuary area. Normally, the estuarine flow rate is controlled by longer climate process like monsoon with long period of precipitation or snow melting with large influence region. The flooding period can extend to several months and there is less variation in the flow rate compared to small river systems. Therefore, the periodic tide affects the sediment transport process throughout the year, with seasonal characteristics of flood season and dry season. Due to the complexity of estuarine topography, each estuary of large river system has its unique characteristic.

i.e. The Fraser River is one of the longest rivers on the North American, with the length of 2657km. The estuary flow rate comes from snow melting. As a result, the flood season is spring from May to mid-July with the average flow rate >4000m^3/s. From autumn to spring is the dry season, with the flow rate <1500 m^3/s. Field observations in mid-estuary suggested in flood season, the SSC was > 60 mg/l in low tide and <5-10 mg/l in high tide. The main SS component is sand, which suggested the re-suspension of bed material in low tide and deposition (or transferred to bedload transport) in high tide. In dry season, the sediment load was small and dominated by silt and clay-size materials. The estuary is partially mixed with the saline water intrusion to mid-estuary. Due to the tidal effect in mid-estuary, the net transit of bedload is landward while the net transit of suspended load (mostly washload) is seaward. (Milliman, 1980).

The Columbia River is also a large river in North American with the length of 1950km. The flow rate is controlled by both precipitation (peak in January, ~10000 m^3/s) and snow melting (peak from late April to July, >13000 m^3/s). In dry season, the flow rate is less than 4000 m^3/s. It is a partially mixed estuary and a turbidity maximum is developed in the mid-estuary in a whole year. The SSC at the turbidity maximum is 10 times greater than the SSC in the river and 10-20 times greater than that in the ocean, which suggests the turbidity maximum is developed by re-suspension function of the tide. In response to the semidiurnal tides, the turbidity maximum is adverted landward and seaward in each tidal period with an excursion distance of about 20km. In response to the fortnightly tidal variations, the turbidity maximum degenerates during neap tides and regenerates during spring tides. In response to the seasonal flow rate

variation, the SSC at the turbidity maximum increase and pushed seaward during flood season while the characteristic of semidiurnal tide and fortnightly tidal variation still exists. (Gelfenbaum, 1983).

The Mekong River is one of the longest rivers in Southeast Asia, with the length of 4200km influenced by both East Asia Monsoon and Southwest Monsoon. The Mekong River drainage basin is one of the most productive regions of the world. The suspended sediment taken from Mekong estuary is fine silt and abundant with organic matters. The observation in flood season (November) suggested that in the estuarine channel, the suspended sediment is flocculated and deposit at high slack while re-entrained when current speed >0.5m/s (about half of the velocity in maximum flood and 1/3 of the velocity in maximum ebb). The suspended sediment is transported to downstream. A salty wedge appears at the end of the estuary only in flood tide, which restricted the re-suspension due to highly stratified in the bottom. Large amount of suspended sediment is deposited in this location. Meanwhile, in dry season, the tide intruded to the estuarine channel, causing partially-mixed estuarine dynamics, which lead to tidal pumping of sediment into estuarine channel (Wolanski, 1996).

In these large river systems, the estuarine flow rate has obvious seasonal characteristics. Normally the flow rate in flood season is 4-5 times higher than dry season and the duration of flood season continues to several months. In contrast to the small river system, the peak flow rate might 10-20 times higher than non-flood period. Therefore, in large river system, the flow rate difference between high flow condition and low flow condition is not as obvious as in small river system. In the above mentioned examples, although the relative strength of flow rate and tide is different inducing different level of tidal intrusion and salty water mixing. The sediment transport process is influenced by the tide profoundly. The periodical process of re-suspension in maximum flood and deposition in high water slack is observed in all three rivers in flood season. The net transit of bed material is basically seaward. On the other hand, the re-suspension is not obvious in dry season, which also infer the estuarine topography is basically determined in flood season with slightly change in dry season. It should be noted that although the tidal influenced sediment transport process is observed in these studies, the observation range is scattered and locally comparing to the scale of estuary. Its relationship with estuarine topographic changes has not been clarified. To be honest, the overall understanding of topographic change characteristics is hard to be grasped by field observation only, due to the

spatial scale of estuary in the large river systems. The same situation also occurs in the case of Yangtze Estuary.

1.3 Introduction on Yangtze Estuary

Yangtze River is the longest river of Asia and third longest one in the world with the length of 6300 km. The drainage basin is 1,800,000km^2 (Figure 1.1). Based on the hydrological data taken from Datong Station of 624KP (KP: distance from river mouth), which is the last hydrological station on the Yangtze River, the river transport 8.89×10^{11} m^3/year water and 4.59×10^8 m^3/year of suspended sediment into the East China Sea (Yang et al, 2001). The drainage basin below Datong Station is <5% of the whole basin of Yangtze River, the estuarine flow rate is roughly caught by the Datong Station. Besides, the Datong Station is the tidal wave end of Lower Yangtze in dry season. It is not influenced by the tide throughout the year.

The flow rate of Datong is open to the universities and research institutes from 1950 to 1988 (Yangtze Water Conservancy Committee, 1950-1988). After that, only the monthly flow rate is opened in the form of "Changjiang Sediment Bulletin" (Changjiang Water Resources Committee, 1988-). The blue line in Figure 1.2 is the monthly averaged flow rate and standard deviation summarized from 1950 to 2007. The daily flow rate of 1962 (large flow rate in flood season, green line) and 1985 (small flow rate in flood season, red line) are also shown in the same figure. Due to the large drainage basin of the Yangtze River, a single rainy event does not change much of the estuarine flow rate. The whole middle and Lower Yangtze Reach is under the control of East Asia Monsoon with obvious seasonal characteristics. The flow rate at Datong station has high values from summer to autumn (flood season) and low values from winter to spring (dry season). Based on the averaged flow rate for the period 1950-2007, the peak flow rate occurs in July, and lasts approximately 1 month. The monthly average flow rate for July has been ~55,000m^3/s for the past 56 years. The flow rate from December to March corresponds to the lowest value, <15,000m^3/s.

The semi-diurnal tide with high amplitude in the East China Sea controls the flow field in the estuary. As shown in Figure 1.3, the tidal range at the tidal station Sheshan out of the estuary is about 3.5m in both flood season (July) and dry season (January). Meanwhile, the horizontal slope of lower Yangtze to the estuary area is very gentle <1/100,000). As a result, the tide

intrudes to Nanjing of 300KP in non-flood season and Xupu of 100KP in flood season. The tidal waves travel further towards upstream. At the Jiangyin tidal station, the tidal range is ~2.5 m in both July and January. However, due to the changes in the flow rate, the water level in January is ~2 m lower than in July (Figure 1.4).

From Jiangyin, the Yangtze River flow through the huge delta plain. The river width extended to a certain degree (about 90km at the river mouth) and bifurcated to several branches. The first bifurcation is Chongming Island (Figure 1.1). From there, the estuarine channel is divided into the North Branch and the South Branch. The flow in the North Branch is dominated by tide with little net outflow to the sea. The channel is in severe siltation at present. The South branch is the main one. It is wide and discharges most freshwater from the Changjiang to the sea. The South branch is further bifurcated into the South channel and the North Channel. Due to the lack of topography database, the further bifurcation of the South branch does not included in our study.

Our study area is the estuarine channel of Yangtze River from Jingyin (175KP) to Wusong (30KP), about 145km in length. In this area, the river flow and tidal current interact and induce highly unsteady flow field and complicated sediment transport process. As a result, the morphologic changes in this area are frequent and unstable. 2000 years ago, The Yangtze Estuary is a drown valley. The distance between side banks is very wide of ~180km, with multiple sand bars and shoals appears in the valley (including the embryo of the present Chongming Island, which was first found as small intertidal shoal in 7^{th} century). With large scale sediment deposition, the estuary is narrowed and extended to the ocean. In 11^{th}-14^{th} century, the main channel is the South Branch, the South bank of the estuary enlarges very quickly. In 17^{th}-18^{th} century, the main channel move to the North Branch, the North bank of the estuary experienced large scale erosion. In the mid-18^{th} century, main channel move back to the South Branch (Chen and Yun, 1988). From 19^{th} century, due to the extraordinary position connecting Yangtze River and Pacific Ocean, Yangtze estuary area has been developed one of the most economic active and productive region of China. In order to protect the agriculture and industry, the side banks of Yangtze Estuarine Channel is protected by artificial dyke since then. Although in history, the artificial dyke used to be collapsed due to strong erosion at some locations, they are local and soon a new dyke was constructed. Recently, the banks of Yangtze estuarine channel are stable. But the topographic change inside the river is strong. So in our

study, we mainly focus on the topographic change inside the channel, and the side boundaries are set to be unmovable.

1.4 Studies on Yangtze Estuarine Channel

Hydrological stations including above mentioned Datong station is set up in the beginning of 20th century to meet the development of inland waterway transport in Yangtze River. From 1952, the daily flow rate and sediment load was listed as "Historical record on water and sediment" and published every year (Yangtze Water Conservancy Committee, 1950-1988). From 1988, the daily data were not open to the public. Every year, the monthly averaged flow rate and sediment load together with the topography change description is summarized as "Changjiang Sediment Bulletin" (Changjiang Water Resources Committee, 1988-). At beginning, the bulletin was in paper form. From 2000, the Bulletin can be downloaded from internet freely. (http://www.cjh.com.cn). The tidal stations in the estuary area were set also from the beginning of 20th century, which is used to provide reference for navigation and flood prevention. From 1954, the tide forecast table was published in hourly resolution. With the accumulation of original observation data and the development of simulation, the forecast is basically fit the real condition with the temporal difference of 5-10minutes and tidal height difference in 10-20cm. The tidal data we used in our study is from the tide forecast table.

The first systematic field observation in the Yangtze Estuary is a joint study of U.S. and Chinese scientists during 1980-1981 (Milliman et al, 1985: Beardsley et al, 1985; Larsen et al, 1985; Sternberg et al, 1985). After that, numerous field observations are conducted mainly for the port constructions or navigation maintenance. On the base of these observational data and corresponding analysis, in 1988, a book named "Processes of Dynamics and Geomorphology of the Changjiang Estuary" is published, which laid the foundation of current Yangtze River study (Chen et al, 1988). Their studies cover from tidal current limit Jiangyin to the suspended sediment dispersion limit out of the river mouth. The result is summarized as following: 1) semi-diurnal tidal current control the flow field of the Yangtze Estuary. In the estuarine channel from Jiangyin to Wusong, the flow show highly pulsating. Close to the river mouth, the flow rotates clockwise, with southeast-ward at maximum ebb and northwest-ward at maximum flood. 2) Strong mixing occurs in both South Branch and North Branch in non-flood season with the

intrusion of salty water. In flood season, the freshet pushed the salty wedge out of the estuarine channel. Partially mixing occurs 5-50km out of the river mouth, the turbidity maximum develops there. 3) The suspended load is mainly composed of fine silt with the grain-size of 8μm-16μm while the bedload is much coarser. In the estuarine channel, the bedload is composed of well-sorted fine sand, with the mean grain-size of 100μm -200μm. Out of the river mouth, with the large scale deposition, the bedload becomes finer and bad sorted. After that, the field observation is mainly focus on the complicated hydrological condition from river mouth to the continent shelf. The part of estuarine channel is seldom mentioned.

The studies on the topography change in the Yangtze Estuary mainly rely on geological boring, nautical maps and the text description in almanacs along the Yangtze estuary. Therefore, although the estuary development in 2000 years is clarified integrated, the relationship between hydrological dynamics is far from quantified (Chen et al, 1988). The current morphologic change study still mainly relies on comparison of nautical charts, which started from 1840 by British Admiralty, and published in 5-10 years interval (Wang et al, 2008). These studies have established the long-term evolution of topographic change in Yangtze Estuary, however, the seasonal changes in the sediment transport process and corresponding topographic changes are not been well understood.

Recently, numerical simulations have been used to study the characteristics of the flow structure or salinity, and some attempts have already been done in Yangtze Estuary and adjacent sea including 2D and 3D structure (Wu, et al., 2006; Wang et al, 2010; Shi et al, 2011). Their studies were mainly focus on the huge area out of the river mouth, and the models they used were mainly derived from the oceanic models like POM and COHERENS, with an orthogonal mesh system and rough mesh system (1km in longitude direction and 300-500m in cross-sectional direction). Although they got good results in the reproduction of flow structure and salinity distribution, the detail of the topography could not be expressed well, which limited their usefulness for modeling the complicated topography of estuarine channel. Numerical studies on sediment transport and topographic changes of the Yangtze Estuarine Channel are still limited. Hence, in the present study, we investigated the unsteady tidal effect and its seasonal characteristics on the flow field and topographic changes in the Yangtze Estuarine Channel by using numerical analysis with a finer mesh system.

1.5 Outline of this study

1.5.1 Research purpose

From the understanding of other estuaries of large river system, the tidal effect is strong throughout the year including flood season and dry season. The sediment transport is also influenced by both the tide and seasonal variation in flow rate. This phenomenon is supposed to be common in the large river systems. However, it has not been exposed in the Yangtze Estuarine Channel due to the lack of observational data.

In the present study, we try to use the numerical simulation to obtain the main characteristic of flow field and sediment transport process under the unsteady hydrological conditions in both flood season and dry season in the Yangtze Estuarine Channel. In the part of methodology, I have to mention two things:

1) Because the observational data is insufficient and far from systematic, in this study we will mainly use the data taken from hydrological station and tidal stations to do the simulation. I have not collected the observational current velocity and sediment load to verify the calculation results. So I prefer to call this study a "numerical experiment", which is used to obtain the main characteristic of sediment transport and most possible topographic change tendency.

2) The morphology of Yangtze Estuarine Channel is very complicated, with several sand islands, underwater shoals and channels. If we use the long-term real condition in calculation, the main characteristic of sediment transport and topography change trend is hard to be extracted. Therefore, we picked up two typical periods of flood season and dry season, and create two ideal periodical conditions for calculation. Then, the typical characteristic of sediment transport is proposed and we believe it is the controlling factors in morphological development of Yangtze Estuarine Channel.

1.5.2 Thesis contents

The influence of tide is discussed firstly. It covers Chapter 2 and 3. In the case of Yangtze Estuarine Channel, the tidal range is similar throughout the year, but the river flow rate changes

greatly. We chose the flood season to discuss the impact of tide because: 1) in flood season, the tidal effect should be the weakest. Due to the extensively mild gradient in longitudinal direction, the tidal effect in our study area is strong even in flood season, which makes it different from the small river system; 2) with the maximum flow rate input from upstream end, the topography change is supposed to be the maximum in flood season.

In Chapter 2, the tidal influenced flow field in flood season is reproduced by a quasi-three-dimensional (quasi-3D) model. The content also includes the data processing and the discussion of boundary condition influence.

In Chapter 3, a tracer experiment is applied to display the characteristic of sediment transport by the above reproduced flow field. By using the bottom concentration of bed sediment and the frequency distribution of shear velocity, the change of sediment transport mode is discussed at first. Then, the particle with neutral buoyancy is used to express the movement of suspended sediment with water. The movement of tracer can express the main characteristic of sediment transport in a tidal period in flood season.

Next, the influence of flow rate is discussed in Chapter 4 and 5. Two spring tide periods in both flood season and dry season are selected as hydrological conditions, which were used as to compare the characteristics of flow field, sediment transport process and the topographic changes under different hydrological conditions.

In Chapter 4, a horizontal two-dimensional (2DH) model on the base of unstructured triangular mesh system was used to reproduce the flow field in both flood season and dry season, considering the uniform structure of vertical velocity distribution.

In Chapter 5, after the discussion of sediment transport mode in different season, the transport rate of total sediment load is combined to the 2DH model to model the topographic change process in both seasons to investigate the seasonal characteristic of topographic change tendency. Finally, a simplified long-term topographic change process was proposed and the calculation result was compared with the historical records collected from references for qualitative validation.

In Chapter 6, the main results and the conclusions of the study are summarized.

REFERENCE

Baugh, J., Feates, N., Littlewood, M. and Spearman, J.: The fine sediment regime of the Thames Estuary – A clearer understanding, Ocean & Coastal Management, Article in Press, pp.1-10, 2012.

Beardsley, R.C., Limeburner, R., Yu, H. and Cannon, G.A.: Discharge of the Changjiang (Yangtze River) into the East China Sea, Continental Shelf Research, Vol. 4, pp. 57-76, 1985.

Changjiang Water Resources Committee: Changjiang Sediment Bulletin (in Chinese), http://www.cjh.com.cn.

Chen, J.Y. and Yun, C.X.: The evolution process of estuarine channel of Changjiang between Nanjing and Wusong (in Chinese), Processes of Dynamics and Geomorphology of the Changjiang Estuary, Chen, J.Y, Shen, H.T., Yun, C.X eds., Shanghai Scientific & Technical Publishers, pp. 323-339, 1988.

Chen, J.Y., Yun, C.X., Xu, H.G. and Dong, Y.F.: The model of development of the Changjiang Estuary during the last 2000 years (in Chinese), Processes of Dynamics and Geomorphology of the Changjiang Estuary, Chen, J.Y, Shen, H.T., Yun, C.X eds., *Shanghai Scientific & Technical Publishers*, pp. 454, 1988.

Cook, T., Sommerfield, C. and Wong, K,: Observations of tidal and springtime sediment transport in upper Delaware Estuary, Estuarine, Coastal and Shelf Science Vol.72, pp. 235-246, 2007.

Duan, J.G., Wang, S.S.Y. and Jia, Y.: The application of the enhanced CCHE2D model to study the alluvial channel migration process, *Journal of Hydraulic Research*, Vol. 39, No. 5, pp. 469-480, 2001.

Fugate, D., Friedrichs, C. and Sanford.: Lateral dynamics and associated transport of sediment in the upper reaches of a partially mixed estuary, Chesapeake Bay, USA, Continental Shelf Research, Vol. 27, pp. 679-698, 2007.

Garcia, M. and Parker, G.: Entrainment of bed sediment into suspension, Journal of Hydraulic Engineering, Vol. 177, No. 4, pp. 414-435, 1991.

Gelfenbaum, G.: Suspended-sediment response to semidiurnal and fortnightly tidal veriations in a mesotidal estuary: Columbia River, U.S.A., Marine Geology, Vol. 52, pp.39-57, 1983

Guo, Q.C. and Jin, Y.C.: Modeling sediment transport using depth-averaged and moment equations, *Journal of Hydraulic Engineering*, Vol. 125, No. 12, pp. 1262-1269, 1999.

Larsen, L.H., Cannon, G.A. and Choi, B.H.: East China tide current, Continental Shelf Research, Vol. 4, pp. 77-103, 1985.

Lindsaya, P., Ballsb, P.W. and Westa, J.R.: Influence of Tidal Range and River Discharge on Suspended Particulate Matter Fluxes in the Forth Estuary (Scotland), Estuarine, Coastal and Shelf Science, Vol.42, pp.63-82, 1996.

Milliman, J. D., Shen, H. T., Yang, Z. S. and Meade, R. H.: Transport and deposition of river sediment in the Changjiang estuary and adjacent continental shelf, Continental Shelf Research, Vol. 4, pp. 37-45, 1985.

Milliman, J.D.: Sedimentation in the Fraser River and its Estuary, Southwestern British Columbia (Canada). Estuarine and Coastal Marine Science, Vol. 10, pp. 609-633, 1980.

Ross, D.A.: Introduction to Oceanography, *Harper Collins College Publishers*, New York, pp. 512, 1995.

Shi, J. and Zhang, H.L.: Note on a 2DH finite element model of tidal flow of the North Passage of the partially-mixed Changjiang River estuary, China. Journal of Hydro-averment Research, Vol. 5, pp. 49-62, 2011

Sternberg, R.W., Larsen, L.H. and Miao, Y.T.: Tidally driven sediment transport on the East China continental shelf. Continental Shelf Research, Vol. 4, pp. 105-120, 1985.

Vale, C. and Sundby, B: Suspended sediment Fluctuation in the Tagus Estuary on Semi-diurnal and Fortnightly Time Scales, Estuarine, Coastal and Shelf Science, Vol.25, pp.495-508, 1987.

Wang, Y., Shen, J. and He, Q.: A numerical model of the transport time-scale and change of estuarine circulation due to waterway construction in the Changjiang Estuary, China, Journal of Marine system, vol. 82, pp. 154-170, 2010

Wang, Y.H., Ridd, P.V., Wu, H.L., Wu, J.X. and Shen, H.T.: Long-term morphodynamic evolution and the equilibrium mechanism of a flood channel in the Yangtze Estuary (China), *Geomorphology*, Vol. 99, pp. 130-138, 2008.

Wang, Y.H., Ridd, P.V., Wu, H.L., Wu, J.X. and Shen, H.T.: Long-term morphodynamic evolution and the equilibrium mechanism of a flood channel in the Yangtze Estuary (China). Gepmorphology, Vol.99, pp. 130-138, 2008.

Wolanski, E., Nguyan, N.H., Le, T.D., Nguyan, H.N. and Nguyan, N.T: Fine-sediment Dynamics in the Mekong River Estuary, Vietnam, Estuarine, Coastal and Shelf Science, Vol. 43, pp. 565-582, 1996

Woodruff, J., Geyer, W., Sommerfield, C. and Driscoll, N.: Seasonal variation of sediment deposition in the Hudson River estuary, Marine Geology, Vol. 179, pp. 105-119, 2001.

Wu, H., Zhu, J.R., Chen, B.R. and Chen, Y.Z.: Quantitative relationship of runoff and tide to saltwater spilling over from the North Branch in the Changjiang Estuary: a Numerical study. Estuarine, Coastal and Shelf Science, Vol.69, pp.125-132, 2006.

Yang, S.L., Ding, P.X. and Chen, S.L.: Changes in progradation rate of the tidal flats at the mouth of the Changjiang (Yangtze) River, China, Geomprphology, Vol. 38, pp. 167-180, 2001.

Yangtze Water Conservancy Committee: Historical record on water and sediment (internal, in Chinese). 1950–1988.

Yun, C.X: recent developments of the Changjiang Estuary (in Chinese), *Ocean press*. pp.290, 2004.

芦田和男，岡部健士，藤田正治: 粒子の浮遊限界と浮遊砂量に関する研究，京大防災研究所年報，第 25 号 B-2, pp. 401-416, 1970.

芦田和男，道上正規: 浮遊砂に関する研究（1）河床付近の濃度，京大防災研究所年報，第 13 号 B, pp. 233-242, 1970.

宇野誠高，横山勝英，森下和志，高島創太郎，大角武志: 熊本県白川河口域における土砂動態，海岸工学論文, Vol.49, pp.561-565, 2002.

横山勝英，宇野誠高: 河川感潮域における高濁度水塊の挙動―強混合河川の場合，海岸工学論文, Vol.48, pp.631-635, 2001.

横山勝英，河野史郎，山本浩一: 有明海湾奥部の地形・底質分布に関する現地調査，海岸工学論文, Vol.52, pp.936-940, 2005.

横山勝英，宮崎晃一，河野史郎:　筑後川感潮河道と有明海奥部における高濁度水塊の広域移動に関する現地観測，水工学論文集, Vol.52, pp.1339-1344, 2008.

横山勝英，山本浩一，一寸木朋也，金子祐: 筑後川感潮河道における底泥の堆積過程に関する調査,，海岸工学論文, Vol.54, pp.451-455, 2007.

横山勝英，山本浩一，一寸木朋也: 筑後川感潮河道における地形・底質の季節変動に関する研究，海岸工学論文, Vol.53, pp.471-475, 2006.

横山勝英，山本浩一，金子祐，高島創太郎：筑後川感潮河道における底泥の横断堆積構造，水工学論文集, Vol.53, pp.1405-1410, 2009.

横山勝英，山本浩一，金子祐：筑後川感潮河道における洪水時の底質浸食過程と有明海への土砂輸送現象，土木学会論文集 B，　Vol.64, No.1, pp.71-82, 2008.

横山勝英，長屋光彦，金子祐，山本浩一，高島創太郎：筑後川感潮河道における河床地形・材料の変動特性に関する長期連続調査，水工学論文集, Vol.54, pp.685-690, 2010.

小林侑，佐々木努，石川忠晴，箕浦靖久：利根川感潮域における底質特性の季節変動について，水工学論文集, Vol.54, pp.679-684, 2010.

清水健司，入江光輝，石川忠晴：利根川感潮域におけ　る乱流と底泥の巻上げに関する現地観測，水工学論文集, Vol.48, pp.769-774, 2004.

清水康行，板倉忠興，山口甲：2 次元モデルを用いた河床形態変化のシミュレーション，第 31 回水理講演会論文集, pp. 689-694, 1987.

川西澄，筒井孝典，西牧均：河川感潮域における流動と懸濁粒子の動態，海岸工学論文集, Vol.50, pp.411-415, 2003.

川西澄，筒井孝典，中村智史，西牧均：大田川放水路における河川流量と潮差変動に伴う浮遊砂泥の輸送特性，水工学論文集, Vol.49, pp.649-654, 2005.

川西澄，筒井孝典，中村智史，西牧均：大田川放水路における土砂動態と底質変動，海岸工学論文, Vol.52, pp.906-910, 2005.

土木学会編：水理公式集　平成 11 年版, pp.156-192, 1999.

二渡了，楠田哲也，大石京子：強混合河川六角川感潮部における懸濁物質濃度の変動特性，土木学会論文集，　Vol.452, pp.71-79, 1992.

入江靖，石川博基，前田昭浩，山口広喜，坂本哲治，福岡捷二，渡辺明英：筑後川感潮域における洪水流と土砂移動，河川技術論文集, Vol.15, pp.297-302, 2009.

平川隆一，速水祐一，山本浩一，横山勝英，大串浩一郎，濱田孝治：筑後川感潮域における水理特性と物質輸送，水工学論文集, Vol.53, pp.1399-1404, 2009.

鈴木伴征, Arthur Simanjuntak，石川忠晴, Jorg Imberger，横山勝英：利根川河口堰下流部における潮汐流動に伴う微細粒子の運動，水工学論文集, Vol.48, pp.775-780, 2004.

鈴木伴征，大作和弘，石川忠晴：洪水に伴う利根川感潮域の底質変化，河川技術論文集, Vol.9, pp.265-268, 2003.

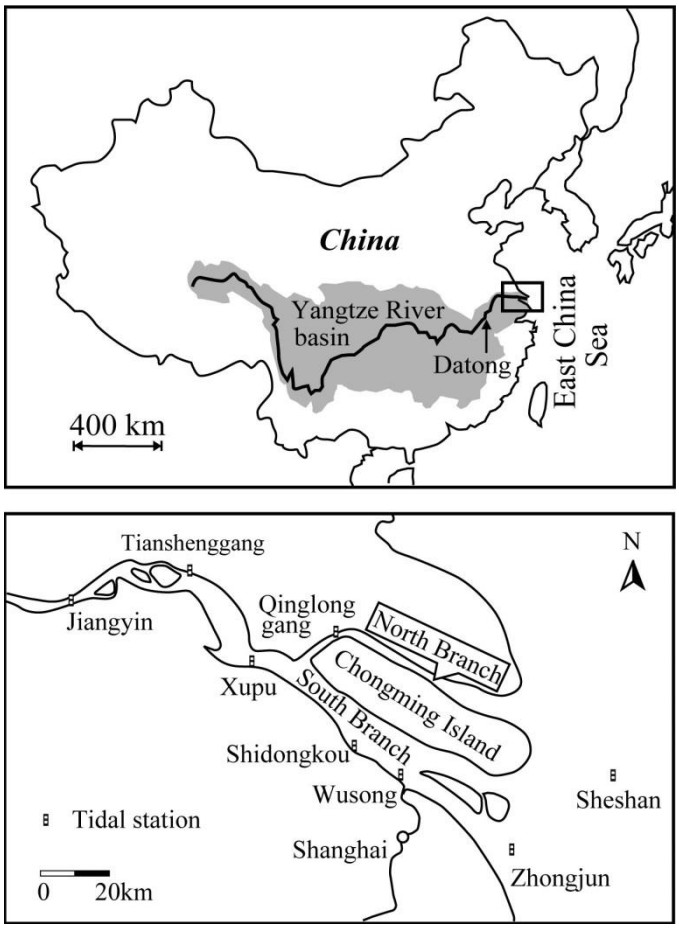

Figure 1.1 The study area and the tidal stations in the Yangtze Estuary

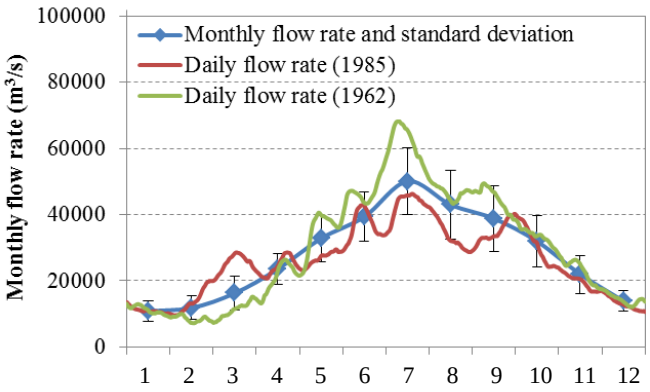

Figure 1.2 The Monthly flow rate and standard deviation (1950-2007), with two series of daily flow rate examples (1985 and 1962)

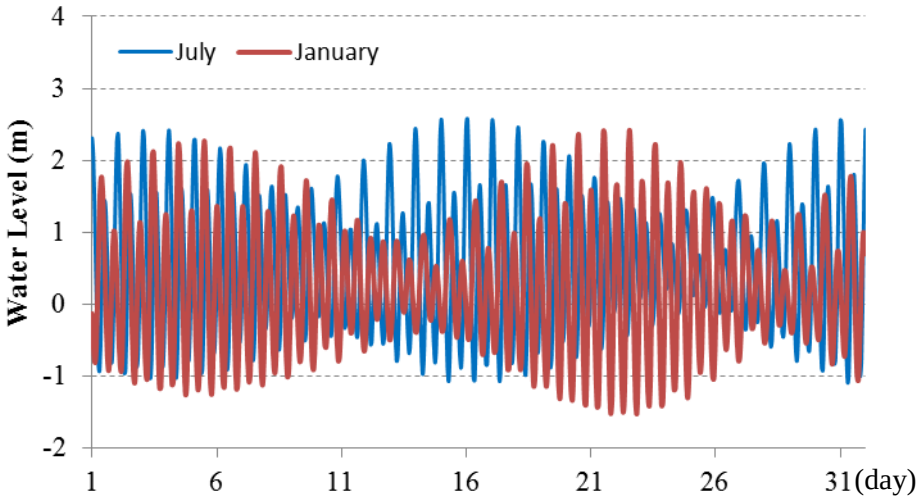

Figure 1.3 The water level at Sheshan (July and January of 2003)

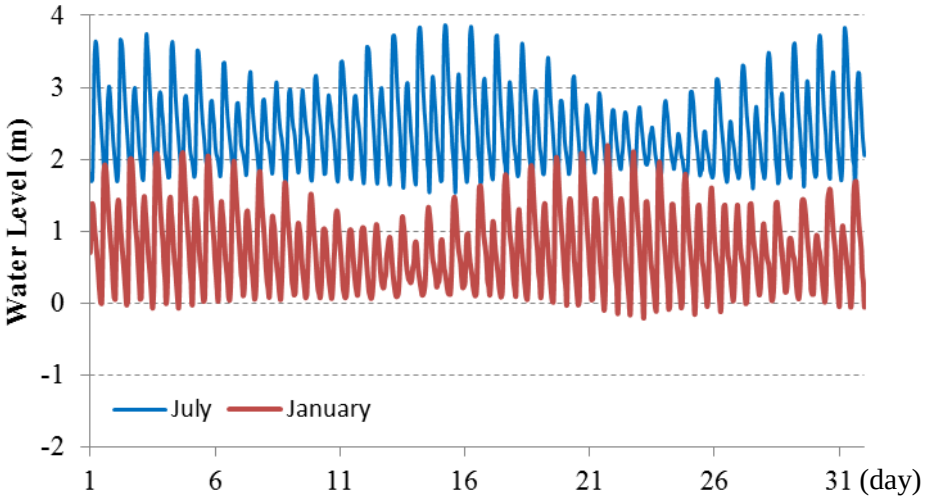

Figure 1.4 The water level at Jiangyin (July and January of 2003)

Chapter 2 Unsteady flow field induced by tidal action

2.1 Consideration

The flood season was selected to investigate the tidal effect in the estuarine channel of Yangtze River, due to its maximum sediment transport tendency and minimum influence of tide. The average water depth in the estuarine channel of Yangtze River is about 10m. Comparing to the huge river width of 2km (Jiangyin) to 15km (Wusong), the topography is quite shallow in the study area. The observations on salinity also suggested well mixing occurs in the whole reach of study area (Shen et al, 2003). The density effect is negligible and the flow field can be simplified to shallow water. However, the study area is very wide with complicated topography. The surface velocity might be the same as the bottom one due to the influence of secondary flow. The horizontal two-dimension (2DH) model on the base of shallow water equations could not expose the influence of secondary flow. Besides, the topography is very complicated in our study area. A fine mesh system is necessary in horizontal 2 dimensions, by which the short time step is required. If we add the vertical dimension to make a full three-dimensional (3D) model, the calculation time and storage of calculation results will become a heavy burden for common personal computers. In this consideration, a quasi-3D model was applied, which can catch the difference of surface and bottom velocity and relief the burden of computation.

2.2 Introduction of quasi-3D model

The quasi-3D model developed by Yoshida and Ishikawa (2008) was used to reproduce the flow field. The equations were derived by applying Galerkin integral to the continuity and momentum equations in vertical. Two modes of trial function were considered for vertical profile of velocity, the depth-averaged component and the linear deviation component. They were placed on the orthogonal curvilinear coordinates (s, n, z) with s direction along the channel, the n direction normal to the s axis (Figure 2.1). The model equations obtained by the above mentioned operation are written as follows:

[Continuity equation]:

$$\frac{\partial h}{\partial t}+\frac{\partial M}{\partial x}+\frac{\partial N}{\partial y}=0 \tag{2.1}$$

[Momentum equation]:

$$\frac{\partial M}{\partial t}+\frac{\partial}{\partial x}(MU)+\frac{\partial}{\partial y}(MV)+\gamma\frac{\partial}{\partial x}(mu')+\gamma\frac{\partial}{\partial y}(mv')=-g\frac{\partial H}{\partial x}+\frac{\tau_{bx}}{\rho}+\frac{\partial h\tau_{uu}}{\partial x}+\frac{\partial h\tau_{uv}}{\partial y} \quad (2.2)$$

$$\frac{\partial N}{\partial t}+\frac{\partial}{\partial x}(NU)+\frac{\partial}{\partial y}(NV)+\gamma\frac{\partial}{\partial x}(nu')+\gamma\frac{\partial}{\partial y}(nv')=-g\frac{\partial H}{\partial y}+\frac{\tau_{by}}{\rho}+\frac{\partial h\tau_{uv}}{\partial x}+\frac{\partial h\tau_{vv}}{\partial y} \quad (2.3)$$

$$\frac{\partial m}{\partial t}+\frac{\partial}{\partial x}(mU)+\frac{\partial}{\partial y}(mV)+\frac{\partial}{\partial x}(Mu')+\frac{\partial}{\partial y}(Mv')=\frac{1}{\gamma}\left(\tau_{f,u}+g_u+\frac{\partial h\tau_{f,uu}}{\partial x}+\frac{\partial h\tau_{f,uv}}{\partial y}\right) \quad (2.4)$$

$$\frac{\partial n}{\partial t}+\frac{\partial}{\partial x}(nU)+\frac{\partial}{\partial y}(nV)+\frac{\partial}{\partial x}(Nu')+\frac{\partial}{\partial y}(Nv')=\frac{1}{\gamma}\left(\tau_{f,v}+g_v+\frac{\partial h\tau_{f,uv}}{\partial x}+\frac{\partial h\tau_{f,vv}}{\partial y}\right) \quad (2.5)$$

In the above, $(M,N)=(Uh,Vh)$, (U,V) are the depth-averaged velocity; h is the water depth; $(m,n)=(u'h,v'h)$, (u',v') are the intensity of deviation velocity components; H is the water surface level; γ is a coefficient relate to the linear distribution (in this study, $\gamma=1/12$ is taken); ρ is the density of water (1000kg/m^3); g is gravity acceleration (9.8m/s^2); τ_{bx} and τ_{by} are the bottom shear stress; τ_{uu}, τ_{uv}, τ_{vv} and $\tau_{f,uu}$, $\tau_{f,uv}$, $\tau_{f,vv}$ are the vertically averaged Reynolds stresses for depth-average velocity and deviation component, respectively.

To maintain the accuracy of the calculation for complicated topography of meandering channel, the CIP-Soroban scheme in a local cylindrical coordinate was adopted in the advection calculation while the Boundary fitted coordinate (BFC) was applied in the non-advection calculation. Details can reference Yoshida and Ishikawa 2006, 2008.

2.3 Data processing

2.3.1 Topography

The topography data was constructed by digitizing a series of navigation maps published by Changjiang Waterway Bureau (2001). The scale of the maps are 1/100,000 and 1/80,000. Each map contains contour lines of 0, -2, -5 and -10 meters and numerous depth points of ~1200m interval in longitudinal direction and ~500m in cross-sectional direction. To maintain the safety in navigation, the datum plane used here are the lowest tidal level. We unified the datum planes of the maps to the average sea level (A.S.L) at first and construct a consistent bathymetry by following Wu et al (2002). In this study, the calculation range was the estuarine channel of

145km long from Jiangyin at 175KP to Wusong at 30KP, where tidal effect is obvious. The North Branch is very narrow and shallow due to the long terms of deposition. According to Yun, 2004, the water volume ratio of North Branch/South Branch in a tidal period is less than 7%. So it was not included in the calculation. The location of our calculation area is marked in Figure 2.2 (a)

The topography under the A.S.L is shown in Figure 2.2(b). Inside the wide channel of 2-15 km in width, large sand islands and underwater shoals exist. The deep part is relatively narrow and quite meandering. For convenient, the deep part of the channel (>10m) is called "thalweg". The mesh system is constructed by interpolating the original survey points. However, if we apply the simple interpolation method only by latitude/longitude coordinates, the thalweg becomes discontinues and differs from the real one (Figure 2.3). In this study, we interpolated the topography along the deepest line of the channel. The deepest point on each survey line was obtained at first. Then, the topography was interpolated at its left and right side separately. If central shoal exists, 2 deepest points at the left and right side of the shoal were obtained. The channel was separated to 3 parts for interpolation (Figure 2.4). Finally, the interpolated mesh system was converted to regular interval for the whole reach. The constructed mesh system has 1,130 cross-sectional lines with 100 grid points on each line. The mean longitudinal grid size is 130m, and the transverse grid size is 15-110m.

2.3.2 Calculation period

The calculation period is July 15-16, 2003 for the typical high flow rate condition. 36 hours in total. As shown in Figure 1.2, the peak flow rate appears in July. Figure 2.5 is the monthly flow rate of July from 1950 to 2007. Although it fluctuates with time, the one in July-2003 is close to the average value among 56 years. On the other hand, because the tidal influence is stronger in spring tide duration than neap tide, the calculation period was selected in spring tide, as shown in Figure 1.3 and 1.4. In other words, the calculation was made for a typical spring tide period in the average flood flow condition.

2.3.3 Water level condition

5 tidal level stations locate inside the study area (Figure 1.1). They are Jiangyin (175KP), Tianshenggang (125KP), Xupu (100KP), Shidongkou (40KP) and Wusong (30KP). Their base levels of tidal height were unified to the A.S.L following Wu et al (2002). The time series of water level at Wusong was used as downstream boundary. The calibration on the Manning's roughness coefficient used the water level records from the other 4 stations from Jiangyin to Shidongkou. Besides, in order to get the flow rate at Jiangyin for the upstream boundary, the water level at Jiangyin was used to deduce the tidal influenced flow rate there.

2.3.4 Flow rate condition

The estuarine flow rate is measured at Datong of 624KP, which is not influenced by the tide. If we set the calculation range from Datong to river mouth, the length will be close to 600km. For the quasi-3D model construction, the fine mesh system is necessary to describe the exact location of thalweg and shoals. The calculation burden (calculation time, storage memory) for the whole tidal influenced reach is too heavy.

The flow rate does not recorded officially in Jiangyin because the water level fluctuates by tide there as shown in Figure 1.4. The flow rate is also influenced by the tide. The private observation is also unaffordable. Because even it is a narrowest channel at the Yangtze Estuarine Channel, it is still 2km in width. The traditional method of flow rate measurement is hard to be achieved. Here we used the numerical calculation to solve this problem. A one-dimensional (1D) flow model was applied to get the time series flow rate at Jiangyin. This model was proposed by Zhao et al, 2007. The shape of the channel was considered with trapezoidal cross-section (Figure 2.6). The side slope was set to be 1/50, which is taken from the cross-section of Jiangyin. The reach from Datong to Jiangyin is quite narrow and slightly meandering with only a few anabranch locations. We believe the trapezoidal shape could catch the main characteristic of the topography in this reach. The channel width was obtained from the satellite images by using Google Earth.

The governing equations are as follows:

[Continuity equation]

$$\frac{\partial A}{\partial t}+\frac{\partial Q}{\partial x}=0 \tag{2.6}$$

[Momentum equation]

$$\frac{\partial Q}{\partial t}+\frac{\partial UQ}{\partial x}=-gA\frac{\partial H}{\partial x}-gA\frac{\tau}{\rho gR}+\frac{\partial}{\partial x}\left(\kappa\frac{\partial U}{\partial x}A\right) \tag{2.7}$$

where t is time (sec); x is distance from upstream point (m); A is cross-sectional area (m^2); Q is flow rate (m^3/s); $U(=Q/A)$ is flow velocity (m/s); g is gravity acceleration; H is water level (m); ρ is density of water; R is hydraulic radius; κ is dispersion coefficient (m^2/s); $\tau\left(=fU|U|\right)$ is bottom shear stress (kg/ms^2) ; coefficient $f=gn^2/h^{1/3}$; n is Manning's coefficient, derived from the calibration.

The equations were solved numerically by applying the Finite Difference Method (FDM) with staggered grid. The flow rate at Datong and water level at Jiangyin were input to the modal as boundary condition. Then the tidal influenced flow rate was caught in the reach from Datong to Jiangyin. The calculation result was verified by the observational water level at Zhenjiang of 270KP (Figure 2.7). The calculated flow rate at Jiangyin was input to the quasi-3D model as upstream boundary. The yearly change of flow rate is shown as the blue line in Figure 2.8. The red line is the selected calculation periods. Figure 2.9 shows the boundary conditions for calculation.

2.3.5 Roughness coefficient

The estuarine channel of Yangtze River is very wide. The roughness coefficient of Manning's equation for the calculation of bottom shear stress might be different. We have not collected enough information on it. For convince, a single value of n was used in our calculation. The value of n was determined by comparing the calculated water level and the observational one. For the calculation, the flow rate distribution at the upstream boundary followed the Manning's equation that the flow rate per width is proportion to 5/3 power of water depth. At the downstream boundary, the water level was the same in the last cross-section. The tidal height

recorded at the tidal stations of Jiangyin, Tianshenggang, Xupu and Shidongkou were used for calibration. After several attempts, the *n* was set to 0.024, which fits best between the calculated water level and the observational one (Figure 2.10). Although the amplitude of calculated water level is a little bit smaller than the observational one at Tianshenggang and Xupu, it is the best one for the single roughness coefficient. So *n*=0.024 is adapted.

2.4 Influence of boundary condition

In small river system like Japanese rivers, the horizontal slope is steep. In consequence, the influence of boundary condition is limited, and the flow field is mainly controlled by topography. In the case of Yangtze Estuarine Channel, the river width is very large (2km-15km) and the slope is very gentle (<1/100,000), the cross-sectional difference may transport very far and influence the calculated flow field. Since the long-term cross-sectional distribution of flow rate and water level at the two boundaries is not available, we used a sensitivity analysis to evaluate the influence of boundary condition to the calculation result.

2.4.1 Flow rate at upstream boundary

As mentioned in 2.3.4, the time series of flow rate at Jiangyin was calculated in the upstream reach by a 1D unsteady flow model. By this means, only the total volume of flow rate in the upstream boundary was obtained. Here, 2 methods were proposed to distribute the total flow rate to every mesh. The first method was based on the Manning's equation, which the flow rate per width is proportional to 5/3 power of water depth, which is widely used in calculation. The other method distributed the flow rate per width with the same value, which means the flow velocity is reverse proportional to the water depth. The velocity distribution by 2 methods is shown in Figure 2.11. Actually, the second method is unrealistic. It is just be used to investigate the influence of boundary condition by such an extremely condition. In these 2 calculations, the downstream boundary was set to be flat by using the water level record in Wusong.

An index was defined to evaluate the difference of results by 2 methods:

$$Index = \frac{\sum_{i=1}^{N}\left(\sum_{t=1}^{T}\left(\frac{\left(u_{1i}^{t}-u_{2i}^{t}\right)+\left(v_{1i}^{t}-v_{2i}^{t}\right)}{T}\right)\right)}{\sum_{i=1}^{N}\left(\sqrt{\left(\frac{\sum_{t=1}^{T}\left(u_{1i}^{t}+u_{2i}^{t}\right)}{2T}\right)^{2}+\left(\frac{\sum_{t=1}^{T}\left(v_{1i}^{t}+v_{2i}^{t}\right)}{2T}\right)^{2}}\right)} \tag{2.8}$$

where u^{t}_{1j} and v^{t}_{1j} is the eastward velocity (u) and northward velocity (v) at mesh number i of every cross-section on moment t by Method 1; u^{t}_{2j} and v^{t}_{2j} is that of Method 2. If the velocities taken from two methods are completely the same, the value of *Index* is equal to 0. The time series t has 5 minutes interval referring to the calculation output.

The calculation result is shown in Figure 2.12. The influence of lateral flow rate distribution decreases quickly along distance. At about 20km downstream from Jiangyin, the influence disappears. A small peak is observed around 160KP. There is a confluence of two branches bifurcated by a sand island (referring Figure 1.1). The difference of lateral flow rate distribution changes the rate of inflow volume at 2 inlets of branches. It is also influence the flow field at the confluence location. Therefore, we think the influence area of upstream flow rate distribution is about 20km.

2.4.2 Water level at downstream boundary

By comparing the water level records at 2 tidal stations of Sheshan and Zhongjun out of the river mouth (referring Figure 1.1), the water level is slightly different between each other (Figure 2.13). Dividing water level range between 2 stations by the distance between them, the average surface gradient is obtained, which is shown by the red line in Figure 2.13. The surface gradient fluctuates a little bit with an order of 10^{-5}. The downstream boundary of our study area is about 15km. Considering the same surface gradient, the water level range between two banks is about 15cm. Here, we compare the flow field with surface gradient to the flat water surface and evaluate the calculation result. Method 1 uses flat water surface by using water level records at Wusong. Method 2 uses the slanting water surface at downstream boundary with the same gradient as shown in Figure 2.13. In these 2 calculations, the upstream boundary was set to be proportional to 5/3 power of water depth.

The calculation result is exhibit by the blue line in Figure 2.12. The influence of cross-sectional water level change at the downstream boundary is about 15km. There are 5 small peaks occurs in the reach. Each locates at the bifurcation or confluence of the channel. The slight water level difference in cross-sectional dissection induces a little change of flow rate distribution at these places. However, the influence is quite small as shown in Figure 2.12, we think the flow field at these places is seldom influence by the cross-sectional water surface gradient. The influenced reach by water level is 15km from Wusong.

By the above discussion, the 20km from Jiangyin at upstream part and the 15km from Wusong at downstream part were influenced by the boundary condition of flow rate and water level respectively. Our investigation on flow field does not include these 2 parts. For our calculation, at upstream end, the flow rate per unit width is proportional to 5/3 power of water depth. At downstream end, the water surface gradient is set to be 0.

2.5 Calculation result

2.5.1 Intensity of secondary flow

At first, the intensity of secondary flow was investigated. Secondary flow is a term to describe a relatively minor flow component which deviates from the main flow direction. In natural open channel, the main cause of secondary flow is the channel curvature. Because the water flowing through a bend must follow the curving streamline, the water surface is slightly higher near the concave bank than near the convex bank, by which the pressure gradient from concave bank towards convex bank keeps equilibrium with centrifugal acceleration. On the other hand, at the bottom layer, the velocity is not large enough to balance the pressure gradient due to friction, which induces a component of flow from concave bank towards convex bank. This circulatory flow pattern is termed secondary flow, which inducing direction change between surface and bottom velocity. In the quasi-3D model, the velocity composes of depth-average component and deviation component, the former representing “Primary flow” and the latter representing “Secondary flow”. The angle between surface and bottom velocity can indicate the intensity of secondary flow.

In Figure 2.14, the largest difference of flow direction between surface and bottom velocity was summarized in a tidal period. The difference of flow direction is almost smaller than 1º. The influence of secondary flow can be regarded very small. Considering the channel morphology (Figure 2.2), the width of the thalweg is about 2km, and the radius of curved thalweg is at least 8km. The curvature is quite small to produce the secondary flow. From above discussion, we think the flow field calculated from quasi-3D model is almost two dimensional, so the following discussion is based on the depth-averaged velocity.

2.5.2 Characteristic of flow field

Figure 2.15 shows the main characteristic of calculated flow field. The Green arrows in the channel are velocity vectors averaged in a tidal period, from 20:00 on July 15th to 8:00 on 16th (referring "a tidal period" in Figure 2.9). In order to get a clearer distributional figure, the number of vector is reduced to 1/20 in horizontal direction and 1/5 in cross-sectional direction. The background represents the water depth under A.S.L. The deep gray color represents the thalweg, while the light gray represents underwater shoals. The main flow is bifurcated and meandered, roughly following the thalweg. The velocity is apparently small above the large underwater shoals.

From upstream to downstream, 5 cross-sections are set with similar interval. Along each cross-section, the change of flow velocity is extracted in every 5 minutes at 3 points, covering thalweg to underwater shoals. The change of velocity in the same tidal period is shown as red arrows. The number indicates right side to left side (facing downstream). The green arrow at the center of the red arrow group is the average velocity vector in a tidal period. The flow in mainstream (a-1, b-3, c-2, d-1, d-3, e-2) shows almost simple oscillation, following the direction of thalweg. The similar tendency of velocity occurs at the other cross-sections. Meanwhile, at the side of thalweg, huge underwater shoal exists. The change of flow is obvious above or close to the edge of shoals (a-2, a-3, b-1, b-2, d-2, e-3). At these locations, although the averaged velocity in a tidal period is very small, the velocity at each moment is not small. The cross-sectional component of flow is remarkable in these locations. The direction of the flow mainly points to the shoal. Above the small scale shoals (c-1, c-3, e-1), the cross-sectional flow

is also relatively small. Above a center shoal which bifurcate the channel (d-2), the cross-sectional flow is similar to both side of the shoal.

Then we can summarize the characteristic of flow field as following: highly pulsating prevails in the estuarine channel of Yangtze River even in the peak of flood season. The mainstream is almost simple oscillation, following the direction of thalweg, while the cross-sectional flow is remarkable at the edges of shoals. This result suggested that the SS are possible to be transported from the thalweg to side or central shoals.

2.5.3 Shear stress distribution

The color contours in Figure 2.16(a) shows the maximum value of shear velocity during one tidal period. Large value appears in thalweg and small value appears above the underwater shoals. There exist four peaks of shear velocity along the thelweg, with the similar interval of 20-22km (marked in red cycle). The location of peaks roughly corresponds to the deep spots in topography in Figure 2.2. Meanwhile, a steady flow calculation is tested in which boundary conditions are kept constant as average flow rate at Jiangyin and average water level at Wusong. The distribution of shear velocity is shown in Figure 2.16(b). In this condition, the shear velocity is almost half as much as in the upper figure. This fact suggests the existence of large shear velocity is the result of tidal change. Besides, because the sediment pick-up rate is a non-linear factor of shear velocity, we can deduce that the sediment transport is more active in the tidal control condition. And the strong erosion may occur in the 4 deep spots in thelweg where shear velocity is very large.

2.6 Summery

In this Chapter, a quasi-3D model is applied to the estuarine channel of Yangtze River to reproduce the unsteady flow field successfully. The influence of boundary condition is discussed by sensitive study. The flow field in the middle part of channel is regarded to be reliable. The characteristic of flow field suggest: 1) The secondary flow is not obvious in our study area, and the flow field can be roughly regarded as two dimensional 2) The flow field is highly pulsatile due to the tidal influence even in flood season. 3) The flow shows simple

oscillation in thalweg while the cross-section flow is remarkable above or near the underwater shoals. 4) 4 peaks of shear velocity appear along channel, which roughly corresponding to the deep spots in thalweg. 5) The shear velocity decrease to half in the steady flow condition, which suggest that the strong bottom friction is controlled by the tide.

REFERENCE

Shen, H.T, Mao, Z.C. and Zhu, J.R.: Saltwater Intrusion in the Changjiang Estuary. *Ocean press*, Beijing, 175 pp. (in Chinese). 2003.

Wu, H.L., Shen, H.T. and Wu, J.X.: Relationships among depth datum levels in the Yangtze Estuary, *The Ocean Engineering.* Vol 20(1), pp. 69-74, 2002

Yoshida, K. and Ishikawa, T.: Fundamental investigation of Depth-Average Numerical Model with Evolution of Secondary Currents in Curved Channels, *Proceeding of the 15th Congress of APD-IAHR*, IIT Madras, Chennai, India, August 7-10, pp. 357-362, 2006.

吉田圭介, 石川忠晴: 2 次流の時空間発展を考慮した水深積分モデルに関する基礎的検討, 水工論文集, No. 50, pp.781-786, 2006

吉田圭介, 石川忠晴: 円筒座標 CIP-Soroban 法と境界適合座標法を組む合わせた蛇行河川の準 3 次元計算法, 水工論文集, No. 52, pp. 997-1002, 2008

趙聯芳, 吉田圭介, 石川忠晴, 二木敬右: 鎮江市内江の流動計算のための長江水理条件の導出, 水工論文集, No. 52, pp. 1051-1056, 2008

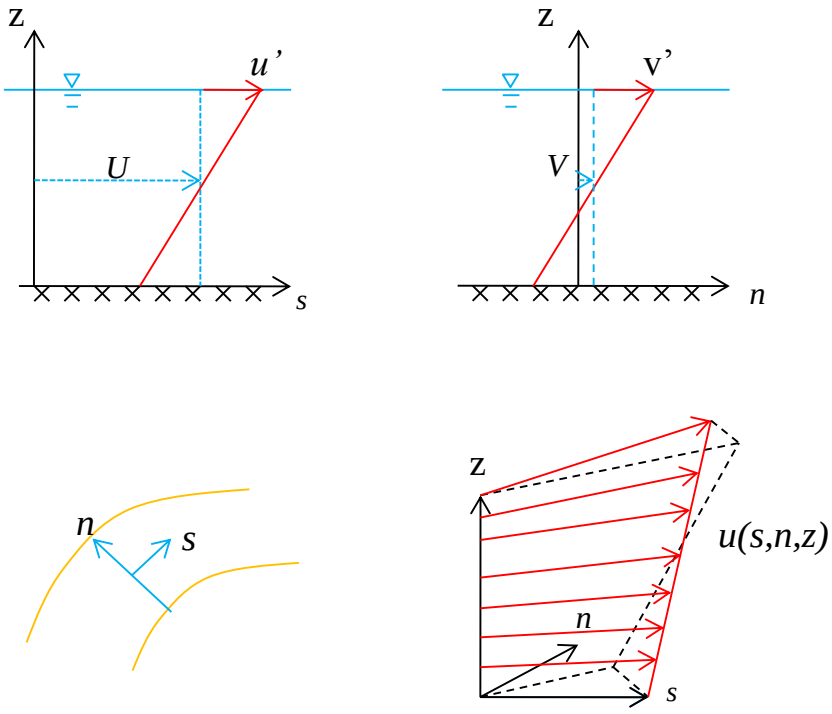

Figure 2.1 The schematic diagram of quasi 3D model

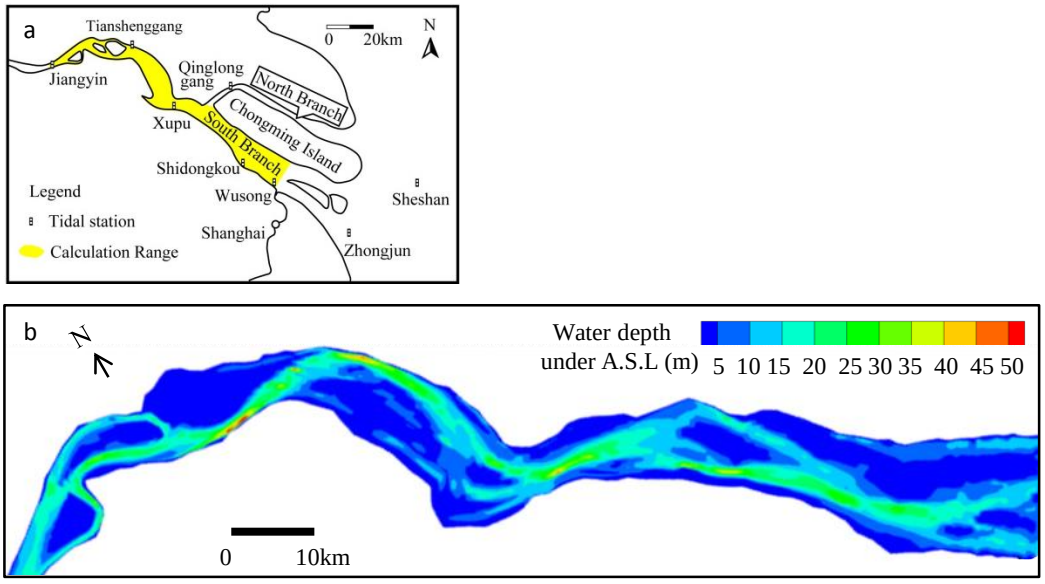

Figure 2.2 The topography of calculation area (water depth under average sea level (A.S.L)) and its location in Yangtze Estuary

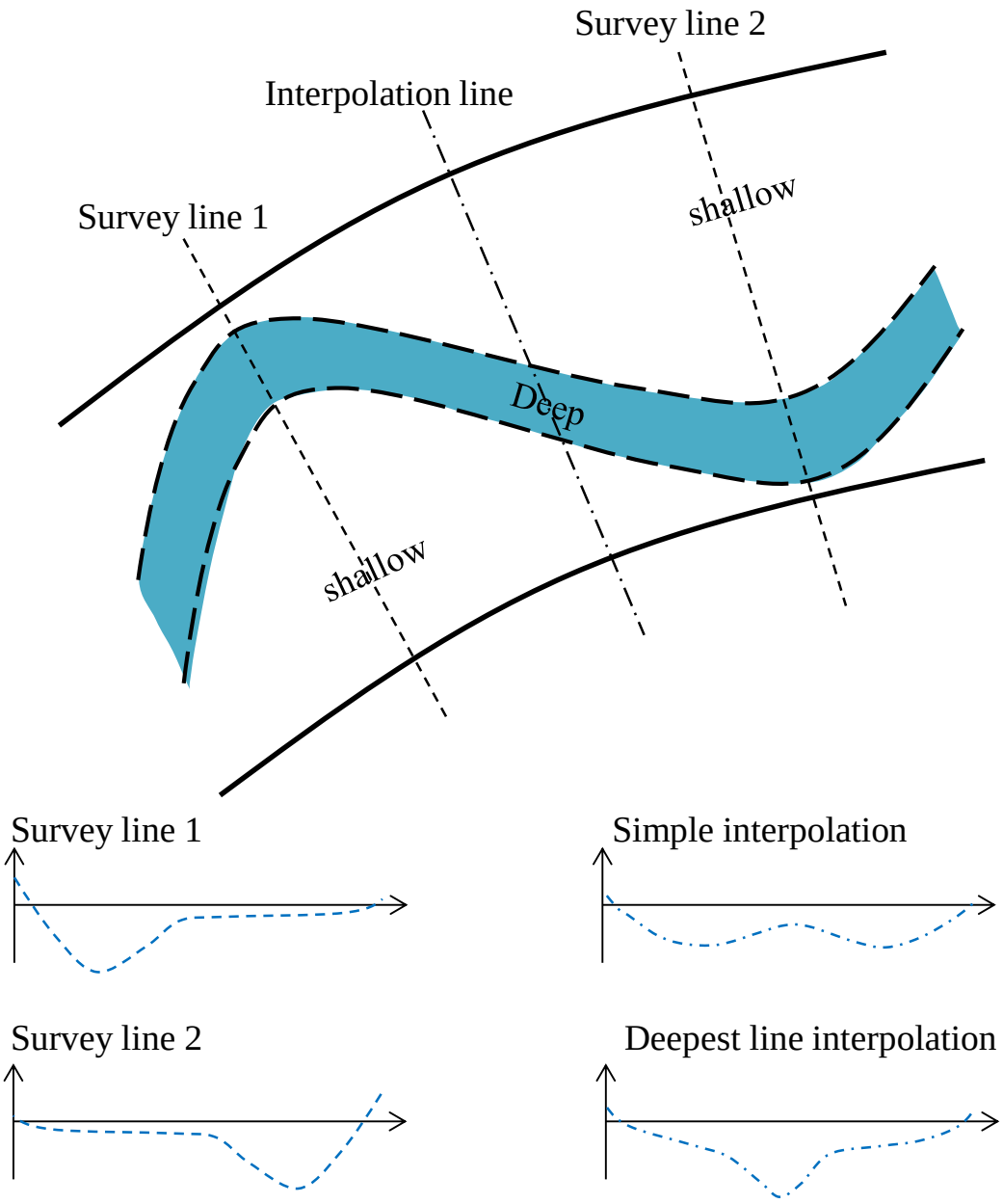

Figure 2.3 The schematic diagram of simple interpolation and deepest line interpolation

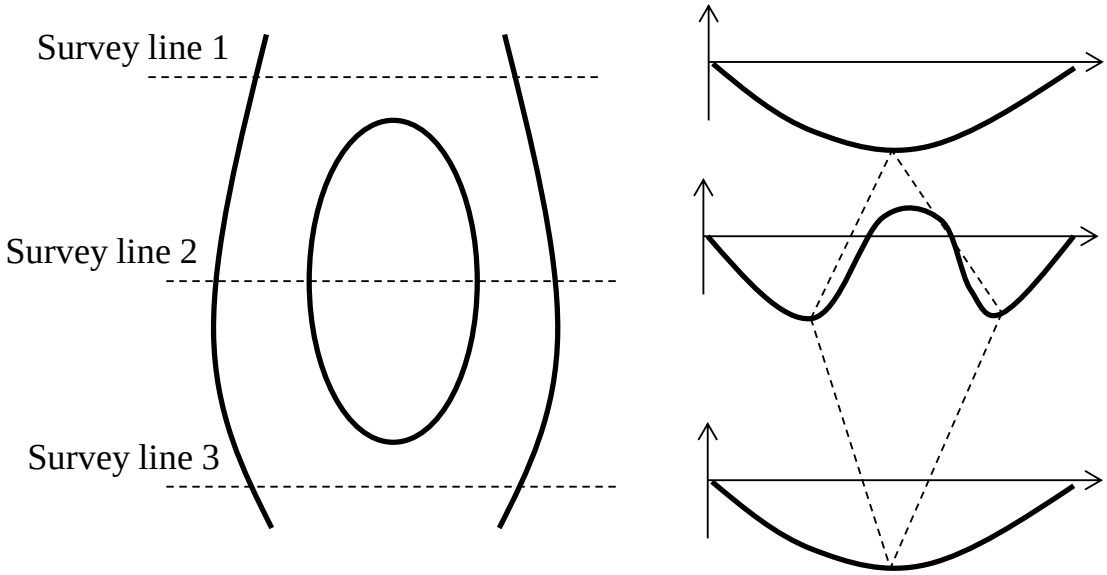

Figure 2.4 The schematic diagram of the deepest line interpolation with central shoal

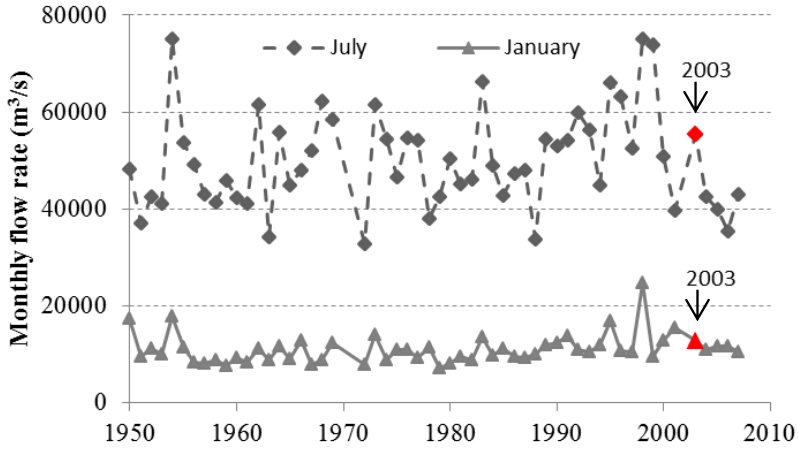

Figure 2.5 The average flow rate in July among 56 years

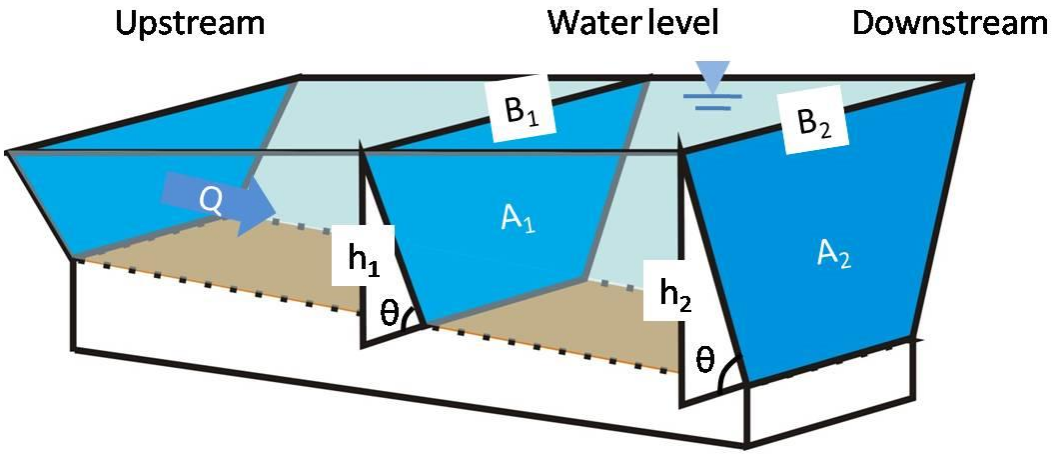

Figure 2.6 The schematic diagram of 1D unsteady flow model

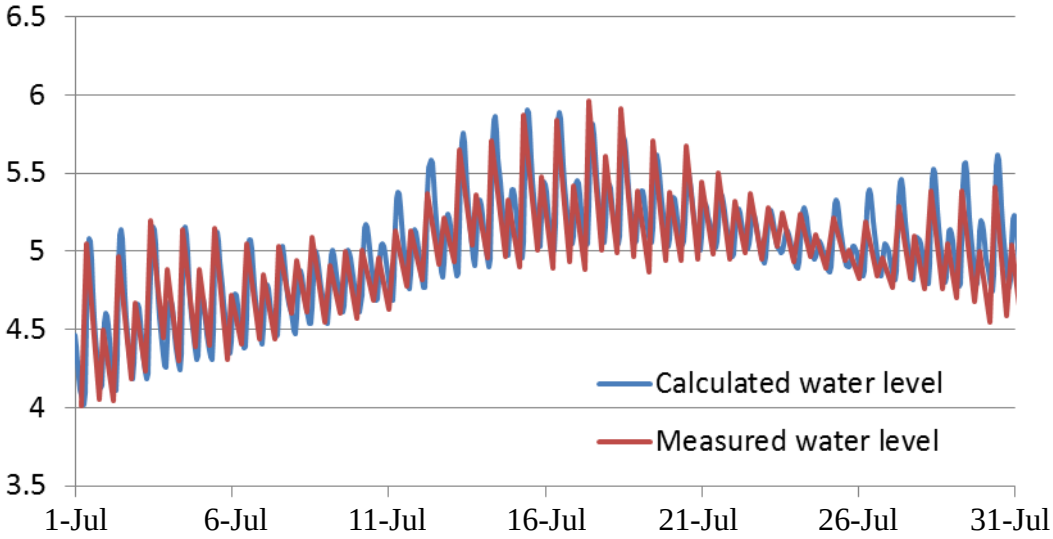

Figure 2.7 the comparison of calculated water level and Measured one at Zhenjiang of (July-2003 as example)

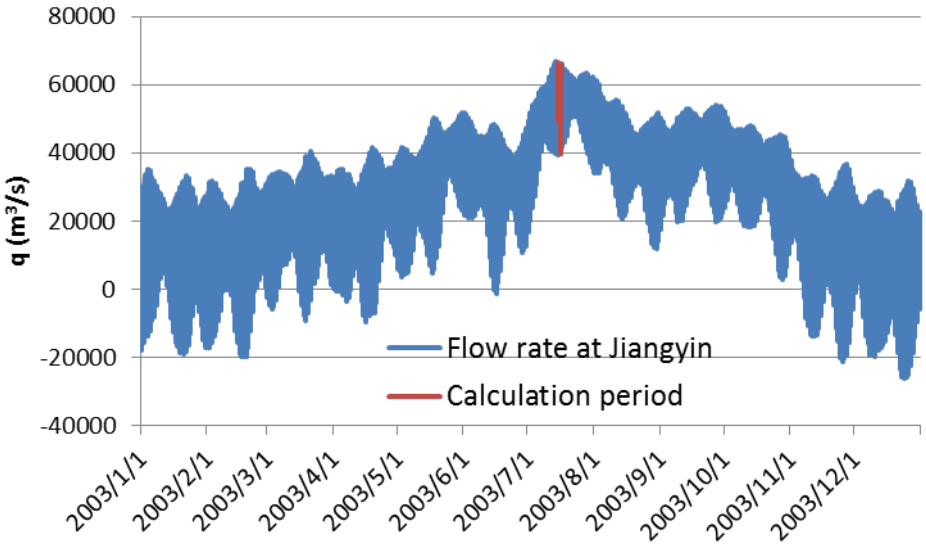

Figure 2.8 The calculated flow rate at Jiangyin and the selected calculation period for the quasi 3D model

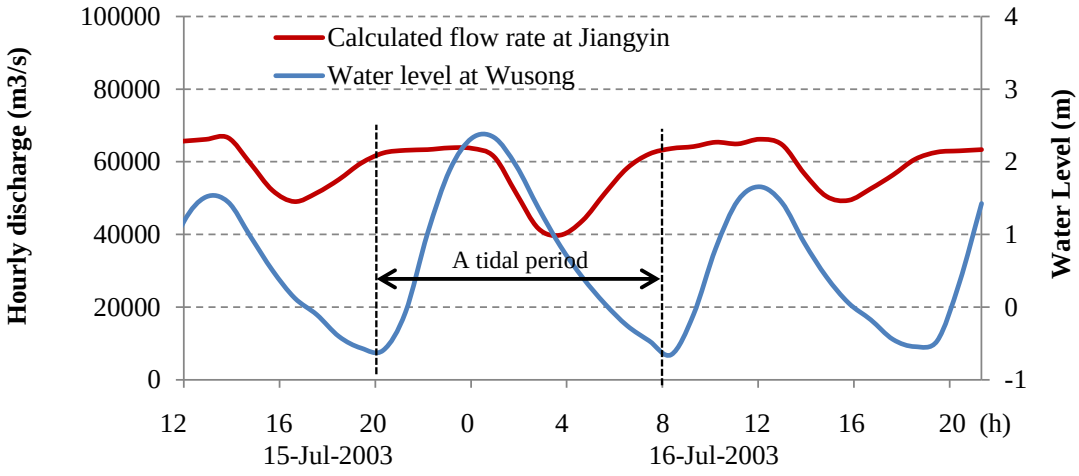

Figure 2.9 The boundary conditions for flow calculation

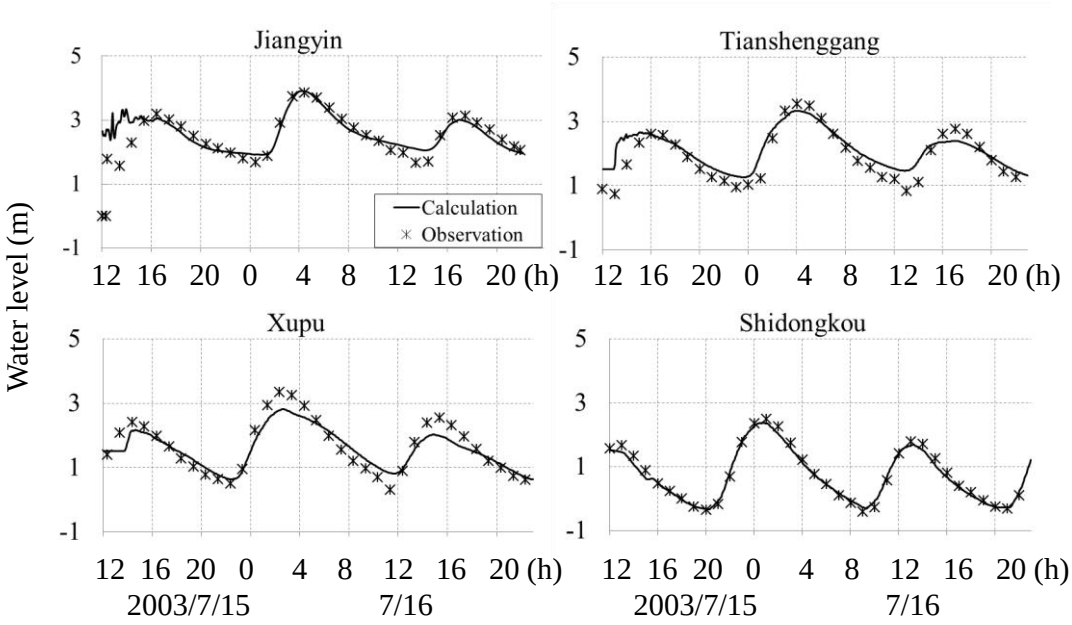

Figure 2.10 The comparison of calculation water level and the observational one (n=0.024)

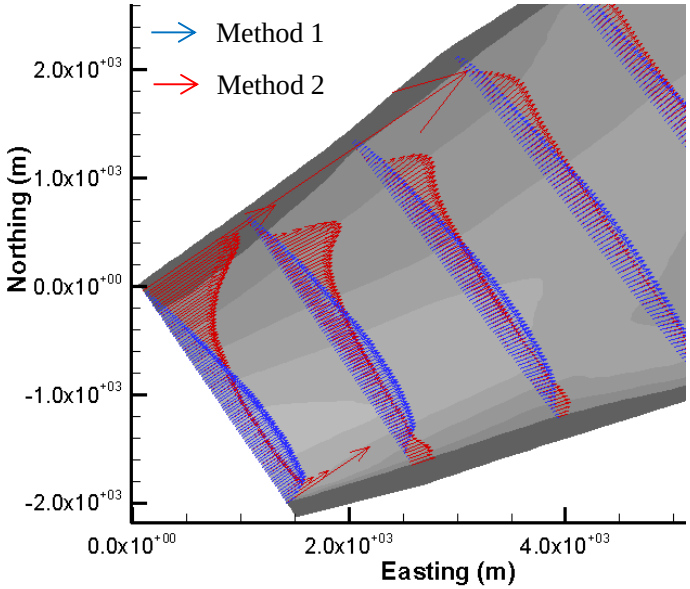

Figure 2.11 The cross-sectional distribution of flow velocity by 2 methods

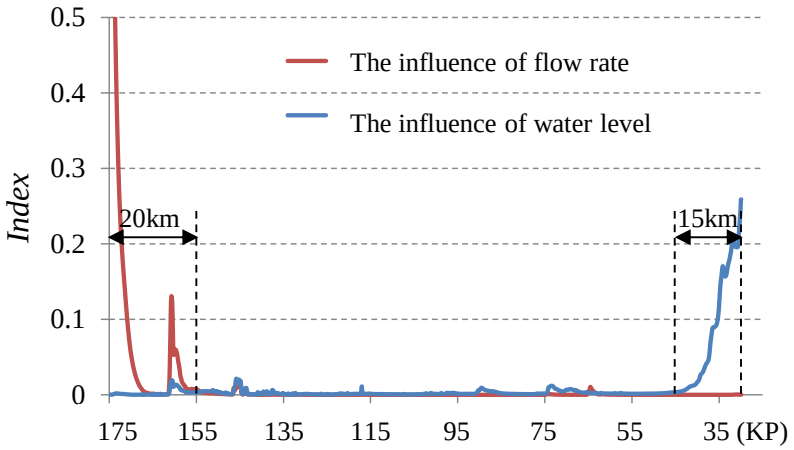

Figure 2.12 The horizontal distribution of Index. The red line indicate the influence of flow rate distribution. The blue line indicate the influence of cross-sectional water level.

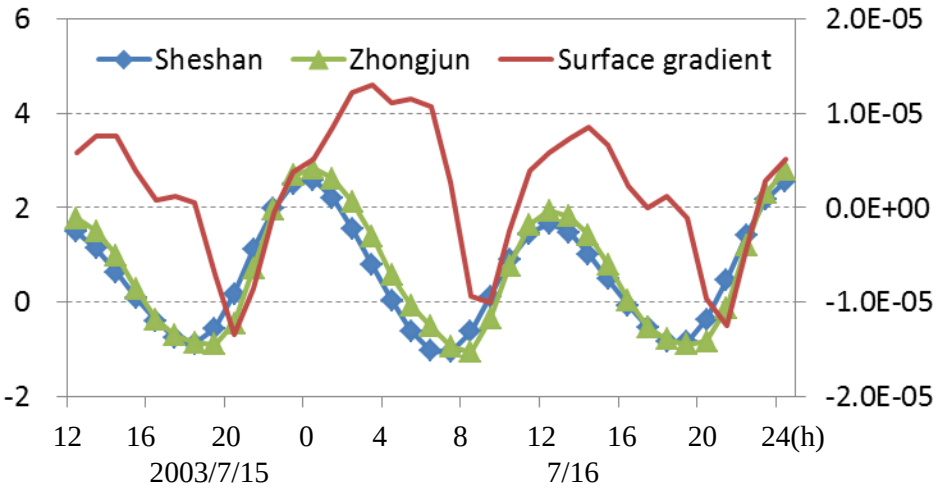

Figure 2.13 The water level record out of the river mouth, and the surface gradient between them.

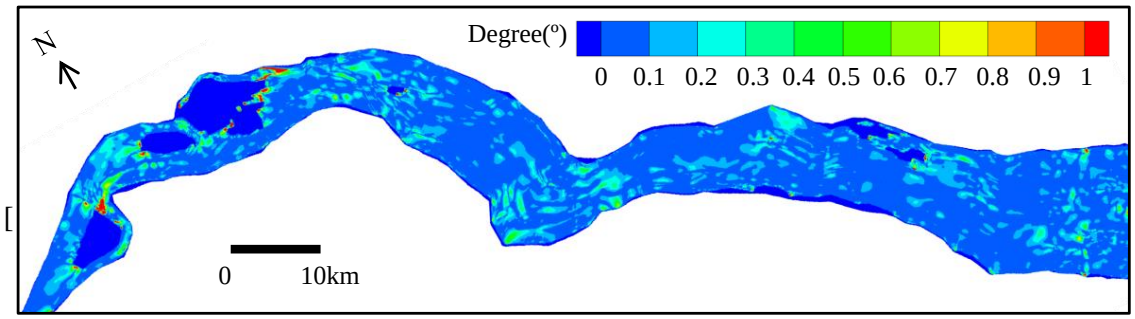

Figure 2.14 The difference of flow direction between surface and bottom velocity.

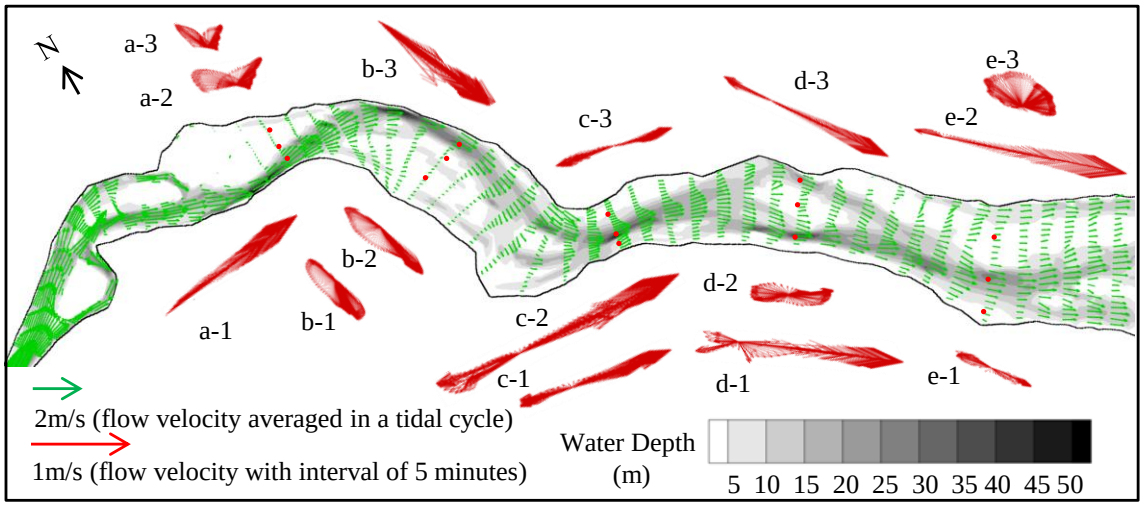

Figure 2.15 the characteristic of flow field including the average velocity and the rotation process in a tide cycle.

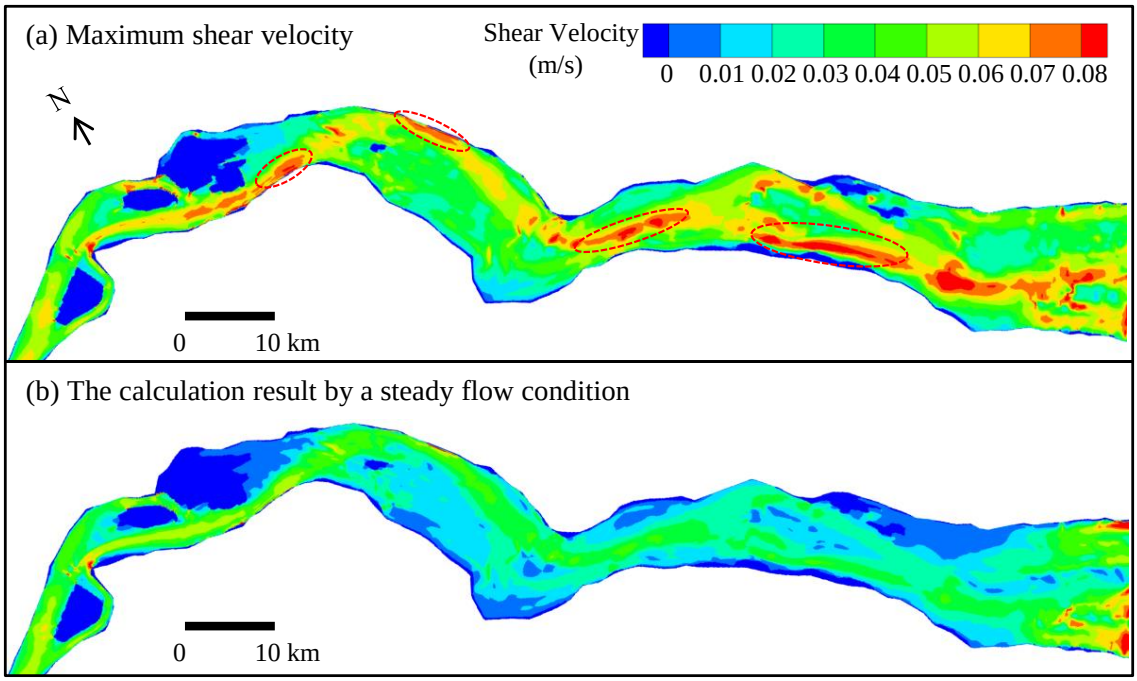

Figure 2.16 The maximum shear velocity in a tidal period and the shear velocity distribution under the steady flow condition.

Chapter 3 Sediment transport in flood season

3.1 Consideration

In the above chapter, the tidal influenced flow field was reproduced. The highly rotation tendency of flow velocity indicates the possibility of sediment transport from thalweg to shoals. The distribution of shear velocity also suggests active sediment pick-up at deep spots in thalweg with regular interval. However, the sediment transport process with the relation to the tidal change has not been exposed. Of course, the fully 3D sediment transport calculation can present the vertical sediment movement of suspension and deposition. But it needs a lot of credible input data, including suspended sediment input volume, output volume, grain-size distribution of bed sediment and suspended sediment, the interference between wash load and suspended load, etc. Besides, the current equations on sediment transport rate are basically experimental, and derived from channel experiments, the scale of which is much smaller than the huge Yangtze estuary. Some parameters might be sensitive to the final result. The main characteristic of sediment transport process might not be easily extracted.

In this consideration, we used a simple tracer experiment to grasp the main characteristic of sediment transport process during a tidal period. The tracer was with neutral buoyancy, and transport at the same speed of water. The sediment pick-up and deposit is qualitatively determined by the comparison of shear velocity and critical shear velocity. At first, the properties of typical bed sediment and flow field were discussed to study the feasibility of tracer experiment. Then two experiments were designed to understand the sediment transport process in tidal influenced condition, and clarify the relationship between spatial periodicity of topography and temporal periodicity of flow field.

3.2 Feasibility analysis

Since the tracer we use was with neutral buoyancy, and flow as the same speed of water, it can only represent the movement of suspended load and wash load. The wash load is only passby. It do not participate the topography change process. So tracer experiment we use is to

catch the main characteristic of suspended load. Before the experiment, we must make sure the suspended load is the main sediment transport mode in our study area and in flood season.

The comparison of shear velocity and setting velocity was used to investigate the sediment transport mode. The setting velocity shows the nature of suspended sediment itself. According to Wang et al 2009, 15 samples were taken in the navigation channel of Yangtze Estuarine Channel with ~10km/sample (Figure 3.1). The water depth covers 6m-40m. The bed sediment sample taken in the estuarine channel of Yangtze River is composed by well sorting fine sand. Figure 3.2 shows examples of grain size distribution of bed sediment. The mean diameter is 100-200μm with a single peak. For simplicity, the uniform size of 150μm was used for bed sediments. The corresponding setting velocity was calculated by the terminal settling velocity w_0 of a sphere in a still fluid, which is obtained from the equilibrium between the net particle weight and the fluid drag force on the particle (Japan Society of Civil Engineers 1999).

$$w_s = \sqrt{\frac{2}{3}\left(\frac{\sigma}{\rho}-1\right)gd + \frac{36\nu^2}{d^2}} - \frac{6\nu}{d} \tag{3.1}$$

where d is the diameter of the sphere, σ and ρ are the sediment and water density respectively, g is gravity, ν is fluid kinematic viscosity. In this equation, the setting velocity is only determined by particle diameter. When the grain-size of 150μm is taken, the corresponding setting velocity is equal to 0.0166 m/s.

The shear velocity is a function of flow field and topography. As shown in Figure 2.16, the shear velocity in thalweg is much larger than that above the underwater shoals. For simplicity, the distribution of shear velocity is rearranged in frequency at every certain moment in Figure 3.3. The x axis is shear velocity (u_*) and the ratio of shear velocity to the settling velocity (u_*/w_0). The red line and the green line refer to the moments when the largest and smallest shear velocity occurs in the whole channel, respectively. They are roughly corresponding to the maximum ebb and at high water slack. According to the experimental concentration of bed sediment at the reference level (Vanoni, 1975), when $u_*/w_0 > 3$, suspended mode prevails. When $u_*/w_0 < 1$, bottom concentration is close to 0. In other words, the sediment is in deposition. The value between 1 and 3 is supposed to be the bedload. Back to our calculated flow field, the frequency distribution shows 2 peaks in maximum ebb. One is larger than 3, mainly in thalweg (referring Figure 2.16). The other is around 2, mainly above shoals. This fact shows that in maximum ebb, the flow velocity in thalweg is large enough to pick-up the bed sediment to

suspension. In contrast, in high water slack, the shear velocity in the whole reach is very small (u_*/w_0 <1). The flow velocity is too slow to keep the sediment in suspension and deposition occurs. In the case of steady flow (blue line), the suspended load is scarce, which indicates the pulsatile transport of bed sediment is controlled by tide. From the above understanding, the suspended mode is prevails from maximum ebb to high water slack. The tracer experiment can represent the suspended sediment transport process in this period.

The time series of shear velocity is used to determine the input moment and checking moment for tracer experiment. The input moment is when time series shear velocity reaches its maximum, which ensures the volume of bed sediment eroded from river bed also reaches its maximum. The checking moment is when time series shear velocity reaches its minimum, which ensures the sediment has largest possibility to be deposit.

3.3 Tracer experiment

From the discussion in 2.5.1, the intensity of secondary flow is regarded to be very small. The flow field is basically 2D movement. So in the tracer experiment, the 2D advection and diffusion equation was used.

$$\frac{\partial c}{\partial t}+U\frac{\partial c}{\partial x}+V\frac{\partial c}{\partial y}=\frac{\partial}{\partial x}\left(D\frac{\partial c}{\partial x}\right)+\frac{\partial}{\partial y}\left(D\frac{\partial c}{\partial y}\right) \tag{3.2}$$

where c is tracer concentration; t is time; x and y are the coordinates in Cartesian coordinate system U and V are the depth-averaged velocity components in x- and y- directions, respectively; D is average horizontal diffusion effect $D=\kappa h u_*/6$; κ is von Karman constant equal to 0.4; h is water depth and u_* is shear velocity in which Manning's equation is used $u_*=\sqrt{\frac{gn_*^2}{h^{1/3}}\left(U^2+V^2\right)}$; g is gravitational acceleration (9.8m/s^2); n_* is Manning's roughness coefficient, in which the result of flow field calibration in 2.3.5 was used, n is set to be 0.024.

3.3.1 Experiment 1: At the most possible erosion locations

From the discussion in 2.5.3, the shear velocity show 4 peaks along thalweg, representing the largest possibility of river bed erosion in maximum ebb. In this experiment, the tracer is input at these 4 locations, and transport with water. The transport pattern is checked until high water slack, when shear velocity reaches its minimum and the tracer is supposed to be deposit.

The boundary condition of flow rate and water level are normalized to be periodical to eliminate the changes of tidal range, (Figure 3.4). The blue lines are the observational water level at Jiangyin and Wusong. The red lines are the result of normalization for the periodical calculation condition. The green line is the periodical flow rate at Jiangyin by applying the periodical water level of Jiangyin to the 1D unsteady flow model as introduced in 2.3.4. By using this boundary condition, the flow field calculation is applied for 4 tidal periods. Due to the initial effect of calculation, the flow field becomes periodical from the second period. The tracer experiment begins from the second tidal period, and the advection and diffusion patterns are checked for one tidal period.

The tracer input moments and locations were determined by following sequence: Figure 3.5 is the horizontal distribution of shear velocity in maximum ebb (moment A in Figure 3.6). Almost the same as Figure 2.16 (a), the shear velocity shows 4 peaks along thalweg, with regular interval of ~22km. The tracer is input to the 5 locations marked by blue rectangles (P1-P5) which represent that the river bed erosion is strong at these locations. The tracer input at the moment of maximum shear velocity, and the dispersion pattern is traced until the moment of minimum shear velocity. The input moment and tracing period is determined by Figure 3.6. It shows the time series of shear velocity at P1-P4. P5 is not included because it is the same as P4). For each location, the maximum value is marked in "■" and the minimum value is marked in "●". The line A and B suggest the appearing moments of maximum and minimum shear velocity for the whole channel in calculation. The maximum and minimum shear velocity at P1-P4 is a little bit different from each other due to the tidal wave transport. For each location, the tracing period is from "■" to "●"

The calculation result is shown in Figure 3.7, including the tracer distribution at 1/4 of calculation period (a), 1/2 of calculation period (b) and the end of calculation period (c). The tracer input at each location is marked to different color for easy recognition. The arrows are the representative velocity at the center of tracer. The rectangles in Figure 3.7(a) represent the tracer input location. Figure 3.7(a)-(b) shows the process of tracer transport from thalweg to shoals.

Together with the velocity vector distribution in 2.5.2, we think the large cross-sectional velocity component is the main factor to transport the tracer to the shoals. Figure 3.7(c) shows that the tracer inputted at location P1 arrives the location around P2; the tracer inputted at location P2 arrives the location around P3 and so on. The transport distance of tracer is almost the same as the interval of locations with large shear velocity. The tracer start from each location arrive the next input locations and the underwater shoals a little bit upstream than the next input locations.

At high water slack, due to the appearance of small shear velocity, the suspended sediment (represented by tracer) is in deposition with the distribution shown in Figure 3.7(c). The deposited sediment in thalweg will be picked-up in the next ebb tide, while the deposited sediment above the underwater shoals is hard to be moved by small shear velocity. This fact causes the development of shoals and more meandering of thalweg with the wavelength of ~22km, which is controlled by the sediment excursion distance during one tide in flood season. This experiment does not consider the bed load movement and the pick-up, deposit process for sediments. The experiment result is no more than a qualitative discussion to propose the relationship of topography development and the tidal effect at the estuarine channel of Yangtze River.

3.3.2 Experiment 2: For the entire calculation range

In experiment 1, we obtain the sediment excursion distance in a tidal period at several critical spots, but the characteristic of the whole reach does not exposed. Therefore, the experiment 2 is designed. Experiment 2 also focuses on the 2 critical moments in tidal circle. Because the tracer input to the whole channel, the time-series of shear velocity for a single location is not appropriate. The channel-average shear velocity is used (Figure 3.6). The input moment is the maximum value and the checking moment is the minimum value. They are marked A and B in the figure. At moment A, the bottom concentration of suspended sediment is calculated for the whole reach and input to the calculation as tracer. At moment B, the tracer distribution is checked and compare to the distribution in moment A. To be noticed, because in equation 3.2, the tracer concentration means depth-average concentration, so the Rouse equation (eq. 3.4) was used to calculate the depth-average concentration at moment A and calculate the bottom concentration at moment B. Due to the periodical calculation condition, the bottom

concentration has the same value in each tidal period. So the comparison of moment A and B can be regarded as erosion and deposition in the next tidal period. At a certain location, if the concentration at moment B is larger than moment A, we think more sediment is transported than the water can carry. The riverbed is in deposition. On the contrary, if the concentration at moment B is smaller than moment A, we think the local sediment is not enough to be carried by water. The insufficient part should be replenished by riverbed erosion.

The Ashida · Michiue equation (Ashida and Michiue, 1970) for the sediment suspension is used to calculate the bottom sediment concentration.

$$C_a = K\left\{\frac{1}{\sqrt{2\pi}\xi_0}\exp\left(-\frac{1}{2}\xi_0^2\right) - \frac{1}{\sqrt{2\pi}}\int_{\xi_0}^{\infty}\exp\left(-\frac{1}{2}\xi^2\right)d\xi\right\} \tag{3.3}$$

where C_a is the bottom concentration at the reference level a; ξ_0 is a parameter concerning shear velocity and setting velocity ($\xi_0=4w_0/3u_*$); K is coefficient for this experimental equation (=0.025).

The Rouse equation is used to obtain the bottom concentration from the depth-averaged concentration.

$$\frac{C}{C_a} = \left(\frac{h-z}{z}\frac{a}{h-a}\right)^Z \qquad Z = \frac{w_0}{\beta\kappa u_*} \tag{3.4}$$

where h is water depth; z is height from river bed; a is reference level (=0.05h); κ is von Karman constant (=0.41): β is coefficient defined by experiment (=1.2). Eq.3.4 is the vertical distribution of sediment concentration for a certain bottom concentration C_a. By integral, the depth-average concentration $\overline{C}$ has a one to one correspondence to C_a. Then we could obtain another bottom sediment concentration C_b from $\overline{C}$ by using numerical integral as Eq.3.5 (Figure 3.8).

$$C_b = \overline{C}\times f(Z) = \overline{C}\times\left(-0.8261Z^3 + 6.3204Z^2 + 2.2523Z + 1.077\right) \tag{3.5}$$

Figure 3.9 (a) is the bottom concentration at Moment A (C_a), showing similar distribution of shear velocity in Figure 3.5. Figure 3.9 (b) is bottom concentration calculated by the dispersion result of tracer at Moment B (C_b). Figure 3.9 (c) is the difference between them (C_b-C_a). The blue means the erosion and the red means deposition. It is clearly that the thalweg (water depth >10m) is erosion and the shallow shoals (water depth < 4m) is in deposition. The calculation

result suggests that the bed sediment at the study area is picked-up from deep thalweg and transport to shallow shoals to deposit, which causing meandering development. Together with the excursion distance of ~22km exposed by experiment 1, we can roughly get the idea that the movement of bed sediment at the estuarine channel of Yangtze River is active. The bed sediment transports from deep thalweg to the shallow shoals continually. The development of shoals inducing channel meandering tendency with the half-wavelength of main stream meandering of ~22km, which is controlled by tidal change in the hydrological condition of flood season. From the observational topography obtained by side-scan sonar and sub-bottom profiler (Wang et al, 2007), small scale sand wave (~100m of wave length and 1m of wave-height) appears at the estuarine channel of Yangtze River, which support the point of active bed sediment movement.

3.4 Summery

The qualitatively discussion on typical bed sediment of 150μm in the estuarine channel of Yangtze river suggested that the bed sediment can be picked-up in ebb tide when shear velocity is large and deposit in high water slack when shear velocity reaches its minimum. By this feasibility analysis, 2 tracer experiments are designed to investigate relationship between spatial periodicity of topography and temporal periodicity of tidal influenced flow field.

Experiment 1 suggested that the sediment eroded from one deep spot in thalweg move to the next one in a tidal period in flood season. The sediment also disperses to the adjacent shoals. In normal flooding flow rate, the distance of particle movement is about ~22km in a tidal period, almost the same as the interval deep spots in the channel, which corresponds to a half-wavelength of main stream meandering. This excursion distance was considered to be as the main factor of the development of meandering thalweg in flood season.

Experiment 2 suggested that in the view of whole reach, the thalweg is in erosion and the underwater shoals are in deposition, which is control by the tide in flood season.

REFERENCE

Vanoni, V.A.: Sedimentation engineering. ASCE, New York, 418 pp. 1975.

Wang, Z., Chen, Z.Y., Shi, Y.F., Li, M.T., Zhang, Q. and Wei, T.Y.: The fluvial bedform and hydrodynamic controls along the middle and lower Yangtze River, *Science China Series D: Earth Sciences*, Vol. 37, No. 9. pp. 1223-1234, 2007.

Wang, Z.J., Chen, Z.Y., Li, M.T., Chen J., and Zhao, Y.W.: Variations in downstream grain-sizes to interpret sediment transport in the middle-lower Yangtze River, China: A pre-study of Three-Gorges Dam, *Geomorphology*. Vol 113, pp. 217-229, 2009

芦田和男, 道上正規: 浮遊砂に関する研究(1)河床付近の濃度, 京大防災研究所年報, 第13号B, pp. 233-242, 1970.

土木学会編: 水理公式集 平成11年版, pp.156-192, 1999.

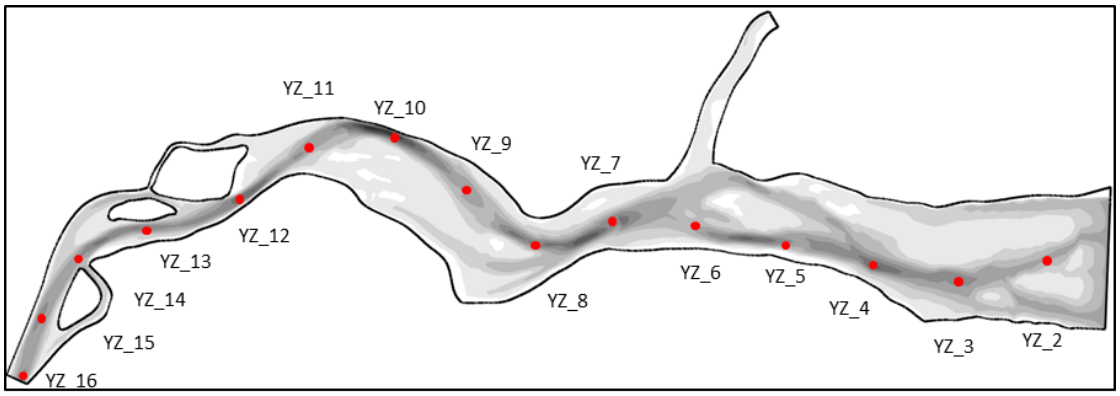

Figure 3.1 The sampling points of bed sediment

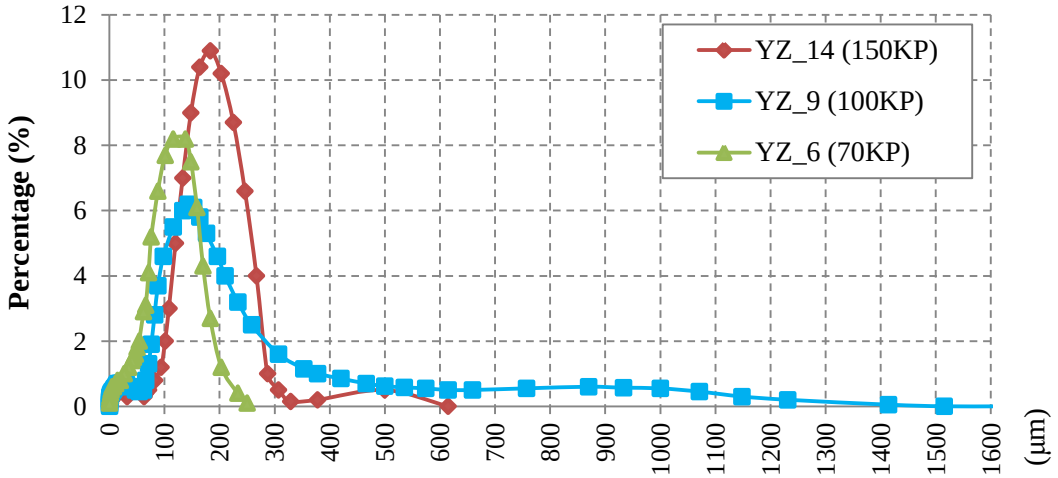

Figure 3.2 The grain size distribution of bed sediment

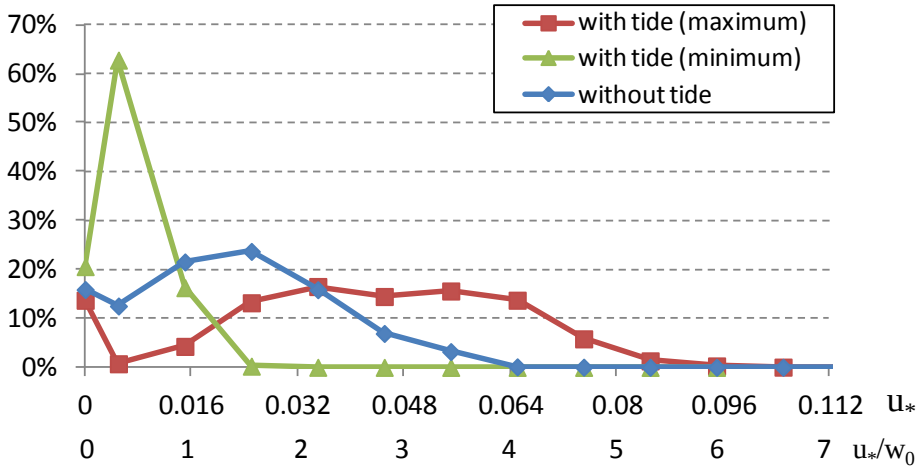

Figure 3.3 The frequency distribution of the ratio of shear velocity u_* to the setting velocity w_0

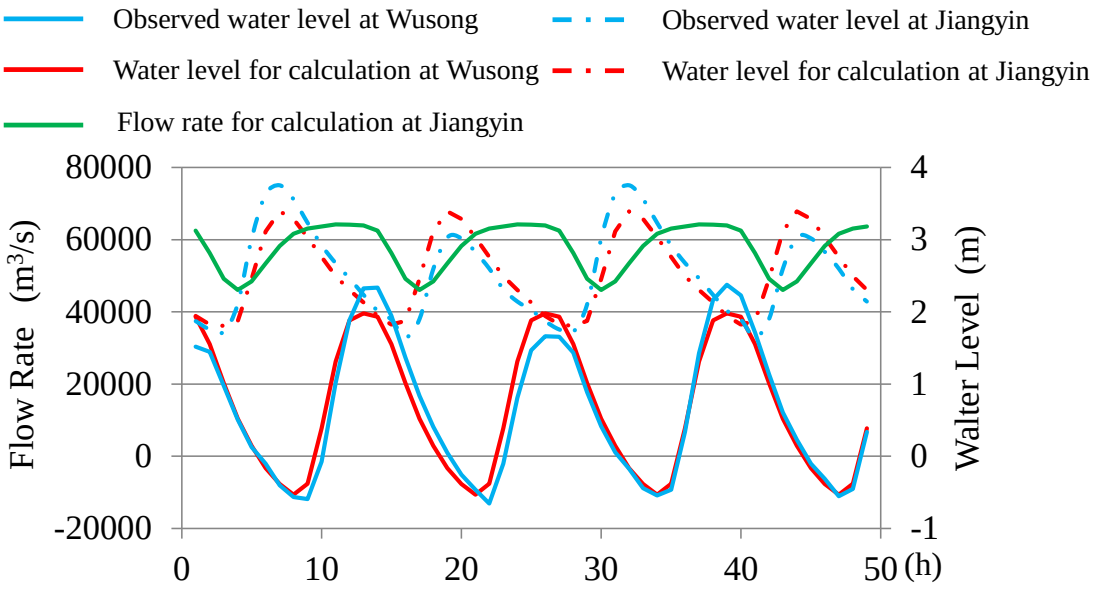

Figure 3.4 Periodic boundary conditions for tracer experiment

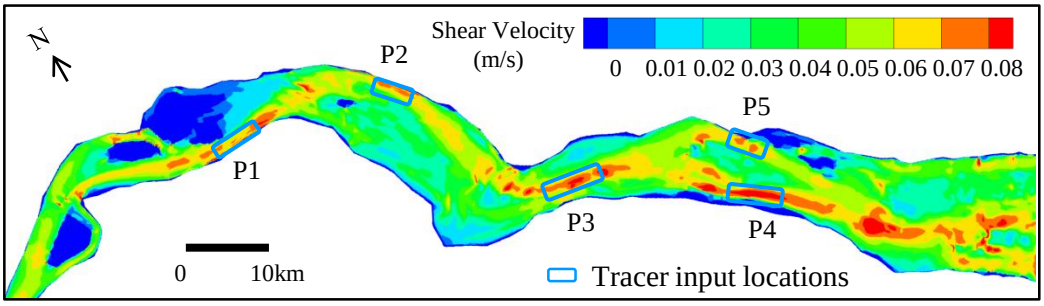

Figure 3.5 The distribution of shear velocity in maximum ebb and the tracer input locations

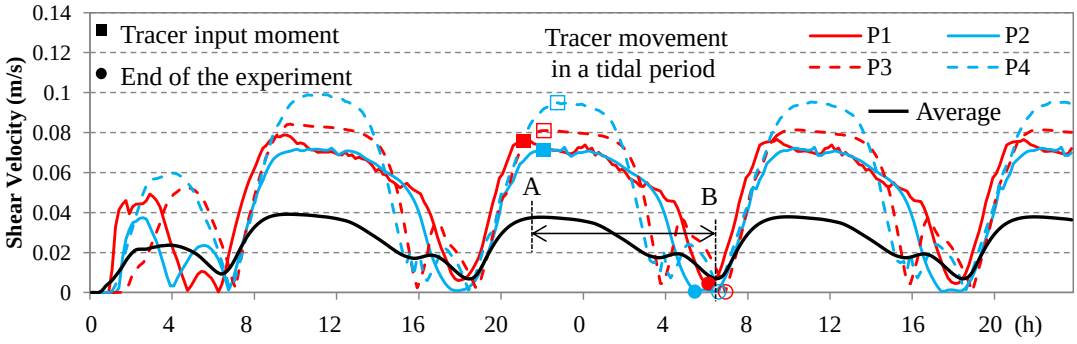

Figure 3.6 The time series of shear velocity at 4 locations

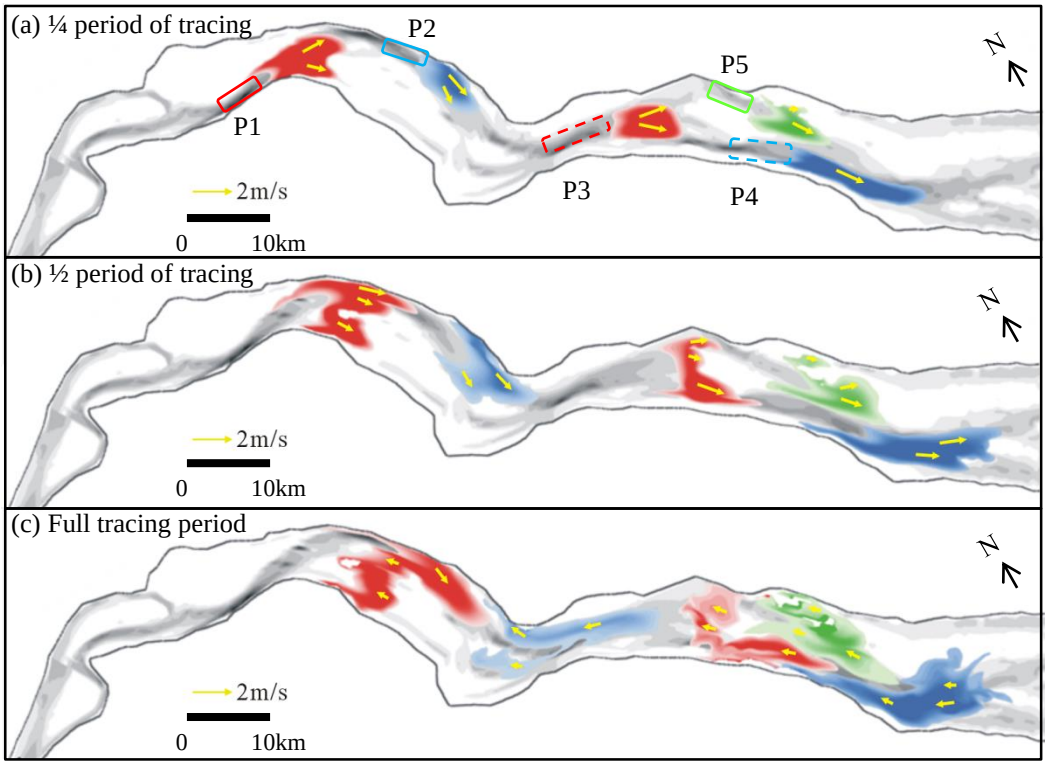

Figure 3.7 The tracer distribution in tracing period with the representative flow velocity

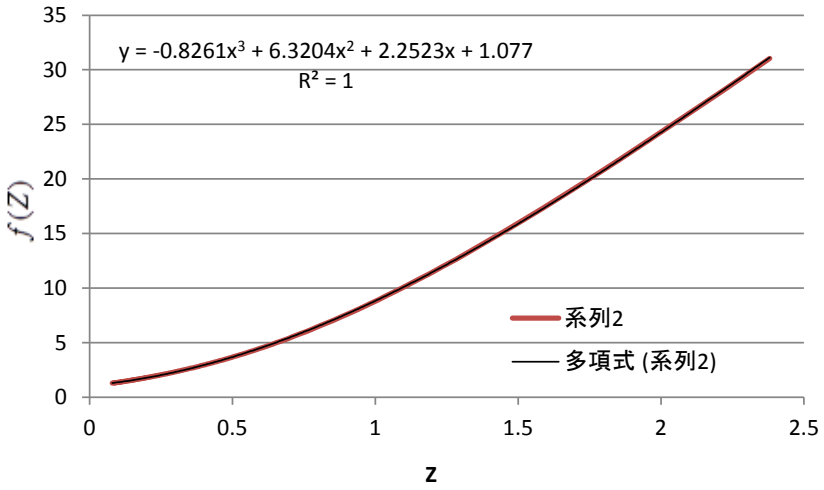

Figure 3.8 the numerical integral of Rouse Equation to get C_b from

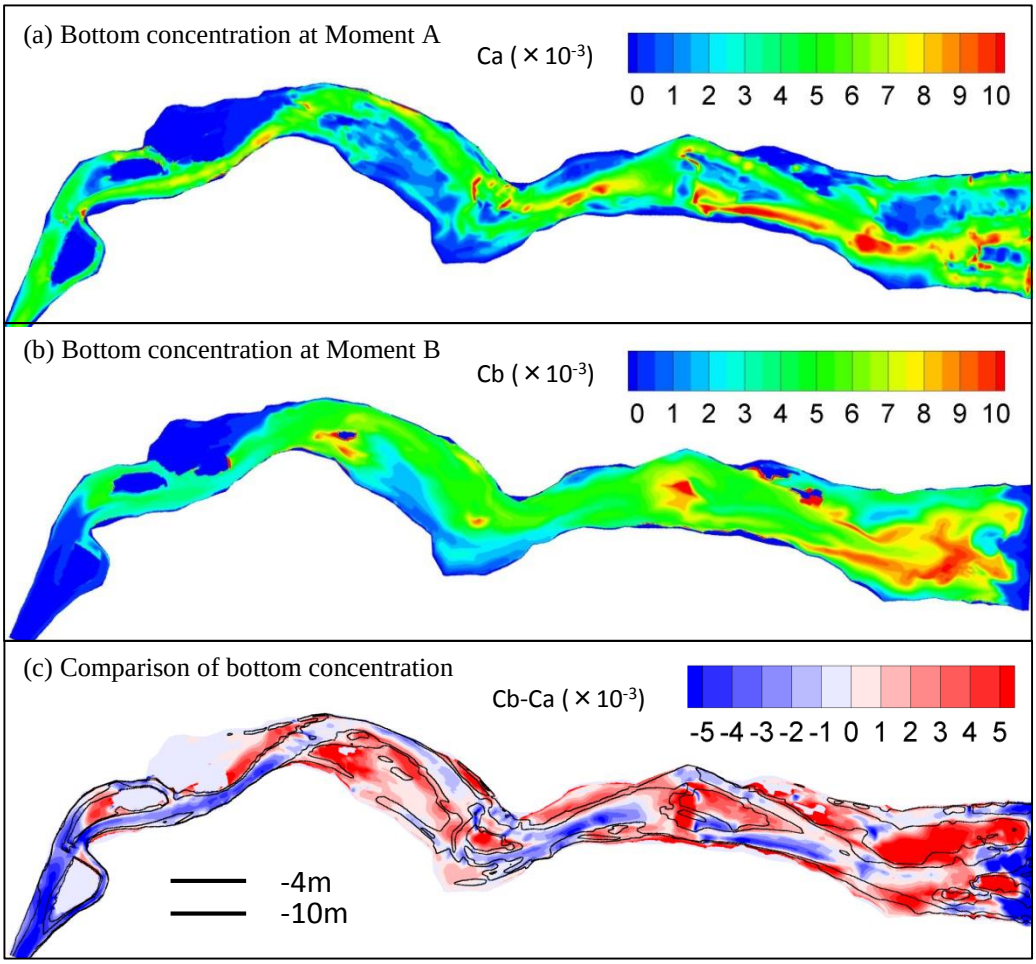

Figure 3.9 The distribution of bottom concentration at Maximum ebb (Moment A in Figure 3.6) , high water slack (Moment B), and the comparison between them

Chapter 4 Seasonal characteristics of pulsatile flow field

4.1 Consideration

In Chapter 2-3, the tidal influenced pulsatile flow field was reproduced and its effect on the suspended sediment transport was discussed in flood season, when the relative strength of tide is weakest. However, as introduced in Chapter 1, the flow rate in the estuarine channel of Yangtze River is mainly controlled by East Asia Monsoon, with obvious flood season and dry season, the flow rate in flood season is about 3 times larger than that of dry season. The tidal influence in dry season is different from flood season due to the little water input. Therefore, in Chapter 4, we mainly focus on the influence of flow rate to the pulsatile flow field. We try to distinguish the characteristic of pulsatile flow field in flood season and dry season, which lays the foundation for sediment transport and topography change study in the next chapter.

4.2 Model Selection

In 2.5.1, the intensity of secondary flow was investigated by comparing the difference between surface velocity and bottom velocity, which was calculated by quasi-3D model. The result shows that the vertical difference of velocity is slight. Normally, the direction change of velocity is less than 1º. The reason is suggested to be the relative small curvature radius of thalweg. Anyway, this fact suggests that the calculation result of quasi-3D model has no big difference from horizontal 2 dimensional (2DH) model. In Chapter 4-5, the 2DH model will be applied.

In the topography change calculation, the accurate reproduction of initial topography is the key point for the reasonable calculation result. The orthogonal mesh system used in quasi-3D model is not good enough to exhibit the complicated topography especially at the edge of the shoals handle. The calculation is easy to be broken. Therefore, in this calculation, the unstructured triangular mesh system is used, which is regarded the smoothest method to reproduce the complicated topography.

Besides, because the topography change process is normally very slow in natural rivers, most of the numerical calculation chooses increasing the span of time step to speed up the calculation.

By CFL condition, the mesh system has to be set in relatively rough resolution. For example, Wang et al, 1995 set 60s as time step to the 2DH model to calculate the topography change at Wadden Sea in Dutch. The corresponding mesh size is ~3km. Xie et al, 2010 used Delft 3D to model the topographic change at Hangzhou Bay of China. His mesh size is 1km and the time step is also 60s. In the present study, the program is developed on the GPGPU (General Purpose computing on Graphics processing Unit) to speed up the calculation with small time step (1s) and fine meshes (~100m).

4.3 Introduction of 2DH model

4.3.1 Basic equations

The 2DH model with unstructured triangular mesh system was proposed by Akoh and Xiao in 2010, which is applied to reproduce the tsunami wave in 2012 (Akoh and Ishikawa, 2012). The model is based on shallow water equations, which are normally used to describe the flow which horizontal scale is much larger than the vertical scale. In our study, the longitudinal length is 145km. The cross-section length is 2km at Jiangyin and 15km at Wusong. The water depth is 0-50m. It is very shallow comparing to the horizontal scale. So the shallow water equations can be used in our study area. Here are the basic equations.

$$\partial_t q + \partial_x F + \partial_y G = S \tag{4.1}$$

$$q = \begin{bmatrix} h \\ hu \\ hv \end{bmatrix}, \quad F = \begin{bmatrix} hu \\ hu^2 + \frac{1}{2}gh^2 \\ huv \end{bmatrix}, \quad G = \begin{bmatrix} hu \\ huv \\ hv^2 + \frac{1}{2}gh^2 \end{bmatrix}, \quad S = \begin{bmatrix} 0 \\ S_{bx} + S_{fx} \\ S_{by} + S_{fy} \end{bmatrix} \tag{4.3}$$

where h is water depth; hu and hv are the flow rate component in x- and y- directions; g is gravity; S_b is the source term of bed slope, S_f is the source term composed of Reynolds stress and bottom friction.

$$S_{bx} = -gh\partial_x z, \quad S_{by} = -gh\partial_y z$$

$$S_{fx} = -\frac{\tau_{bx}}{\rho} + \partial_x(h\tau_{uu}) + \partial_y(h\tau_{uv}) \tag{4.3}$$

$$S_{fy} = -\frac{\tau_{by}}{\rho} + \partial_x(h\tau_{uv}) + \partial_y(h\tau_{vv})$$

where z is bed elevation; ρ is water density, τ_{bx}, τ_{by} are shear stress of river bed; τ_{uu}, τ_{uv} and τ_{vv} represent the depth averaged Reynolds stress with the respect to uniform flow, which is derived from 0 equation model. In the terms of bottom shear stress τ_b, the following equation is used:

$$\boldsymbol{\tau}_b = f \cdot \rho \boldsymbol{U}_{ave} |\boldsymbol{U}_{ave}| \tag{4.4}$$

where τ_b is the vector of bottom shear stress, ρ is the density of water, f is the coefficient of bottom shear stress, which is calibrated experimentally by the comparison of calculated and observed water level. $\boldsymbol{U}_{ave}$ is the vector of velocity, which is averaged from the adjacent 4 meshes.

$$\boldsymbol{U}_{ave} = \tfrac{1}{2}\boldsymbol{U}_m + \tfrac{1}{6}\sum_{i=1}^{3} U_i \tag{4.5}$$

The relationship of $\boldsymbol{U}_m$ and $\boldsymbol{U}_i$ can refer Figure 4.1. Here the $\boldsymbol{U}_{ave}$ was used instead of the original $\boldsymbol{U}$ because in the unstructured triangular mesh system, all the parameter is placed at the center of the triangle including the water depth h (Figure 4.2 (a)). Although the exact topography along the black line should be the same, the value in the triangle is different due to the direction of the triangle. When we calculate the velocity vector $\boldsymbol{U}$ from the streamline $h\boldsymbol{U}$ (Figure 4.2 (b)) by $\boldsymbol{U} = h\boldsymbol{U}/h$, it shows opposite situation that big velocity appears at the shallower places Figure 4.2 (c), which is not fit for the real phenomena. Therefore, we use $\boldsymbol{U}_{ave}$ instead of the original $\boldsymbol{U}$ (Figure 4.2 (d)), which is basically follow the real phenomena that small velocity appears at the shallower places.

4.3.2 Discretization

In order to apply the shallow water equations to the unstructured triangular mesh system by finite volume method, the Godunov's method is used. The time evolution is given by:

$$q_i^{n+1} = q_i^{n+1} - \frac{\Delta t}{\Delta s_i}\left(\sum_{j=1}^{3}\left(\boldsymbol{E}_j^* \cdot n_j dl_j\right) - \Delta s_i \boldsymbol{S}_{b_j}^*\right)_i^n + \Delta t \boldsymbol{S}_{f_i}^n \tag{4.6}$$

where $E_j^* = (F, G)_j^*$ is numerical flux tenser, $n_j = (n_x, n_y)_j$ is the outward unit normal vector in each side of triangle, dl_j is the length of side, Δs_i is the area of triangle, $S_b^* = \sum_{j=1}^{3} S_{bj}^*$ is the bed slope at each side of the triangle. S_f is the integral calculus of source term for each triangle.

Furthermore, the approximate Riemann solover-ROE is applied to calculate the numerical flux.

$$E^* \cdot n_j = \frac{1}{2}\left[E_R \cdot n + E_L \cdot n - R\,|\,\Lambda\,|\,R^{-1}(q_R - q_L)\right] \tag{4.7}$$

where R is right eigenvector matrix of the Jacobian matrix $A=\partial E(q)/\partial q$, Λ is a diagonal matrix constituted by eigenvalues.

4.4 Data processing

4.4.1 Topography

Basically, the study area is the same as in the quasi-3D model. It is the estuarine channel of 145km long from Jiangyin to Wusong. However, in order to obtain the influence of the North Branch to the main channel, it is included in the calculation range (Figure 4.3). The study area extended to the tidal station Qinglonggang.

The mesh system is created by the software ANSYS. The mesh number is 292695 corresponding to ~100m in resolution (Figure 4.3). These meshes are carefully placed along each contour line. The topography database created for quasi-3D model applied to the mesh system by taking the nearest value of topography for every edge. Then the value of triangle is calculated by averaging 3 edges of every triangle. In order to avoid the abnormal calculation result at the downstream boundaries, 2 blocks are defined about 2km in length. The topography at these two blocks is fictional, which change from completely water area (the water depth is the same as the deepest point in the real topography at the downstream end) to the real topography by linear interpolation.

This calculation is applied on GPGPU, which can operate in parallel by running a large amount of blocks. A block can be further divided into several threads as the calculation unit of GPU. In order to make full use of shared memory in a block, the meshes in calculation should be partitioned to several subdomains in spatial. Each subdomain is calculated on one block. So the mesh system is partitioned by greedy method to 4294 subdomains (Figure 4.4).

4.4.2 Calculation period

To compare the characteristics of sediment transport processes under different flow rates, two calculations were used, representing the hydrological conditions of flood season and dry season. The average flow rate of July (55000m^3/s) and January (13000m^3/s) in 2003 were selected for the calculation with the following consideration. 1) From Figure 1.2, the flow rate recorded at Datong station (624KP, shown in Figure 1.1) shows the monthly flow rate reaches maximum in July and minimum in January in general. This distribution of monthly flow rate is averaged from 1950-2007. 2) From Figure 2.5, the flow rate for July and January in 2003 was close to the 56-year average.

The spring tide period of July and January in 2003 is selected; specifically, from 11:00 on July 15 to 23:00 on July 16 for the flood season and 10:00 on January 21 to 22:00 on January 22 for the dry season. The relationship of selected periods and the yearly distribution of hydrological condition are shown in Figure 4.5. Each period is 36 hours in length, including 2 and a half tidal periods and starting from high water slack at downstream end (Figure 4.6). The middle period was used to discuss the flow field in the calculation results.

4.4.2 Boundary condition

The boundary condition used in 2DH model was similar to the quasi-3D model. The flow rate is input at upstream end of Jiangyin, which is calculated by the 1D unsteady flow model. The water level is input at two downstream ends of Wusong and Qinglonggang which is reported from the tidal stations.

The flow rate distribution at the upstream boundary follows the Manning's equation that the flow rate per width is proportion to 5/3 power of water depth. At the downstream boundary, the water level is the same in the last cross-section.

The sediment input and output at the upstream and downstream end are set to be 0, because in this reach, the observed suspended samples is much finer than bed sediment. The grain-size of suspended samples are fine silt of 8-16μm, while the bed sediments are fine sand of 100-200μm. We consider the most part of the input sediment are very fine wash load. It is only pass by and does not participate in the topography change process. The topography change is mainly controlled by the movement of bed sediment.

4.4.3 Shear stress coefficient f

The 2DH model used experimental shear stress coefficient f instead of Manning's coefficient n in calculation. So the calibration was done again to determine the shear stress coefficient f. The same as 2.3.5, the tidal stations of Jiangyin, Tianshenggang, Xupu and Shidonghou (marked in Figure 1.1) were used for calibration. After several attempts, the $f = 0.002$ was determined to be the best fit between observational and calculated water level (Figure 4.7).

4.5 Calculation Result

4.5.1 Comparison of quasi-3D model and 2D model

In this dissertation, 2 kinds of model were used. In Chapter 2-3 the quasi-3D model is used while in Chapter 4-5, the 2DH model was used. The mesh system is different. The former uses orthogonal mesh and the latter uses unstructured triangular mesh. The calculation of bottom shear stress is also different, inducing a little deviation after calibration. However, they basically agree with the observational data well (Figure 2.10 and Figure 4.7).

Next, in order to compare the difference in flow field in a tidal period, the following equation is used:

$$Rate = \frac{Max\left(\sqrt{u_1^2 + v_1^2} - \sqrt{u_2^2 + v_2^2}\right)}{Ave\left(\frac{\sqrt{u_1^2 + v_1^2} + \sqrt{u_2^2 + v_2^2}}{2}\right)} \tag{4.8}$$

The numerator is the maximum difference in velocity in a tidal period for each point of the entire reach, and the denominator is the average value of the velocity in a tidal period. The result is shown in Figure 4.8. To be noticed, the topography used in 2DH modal is the same as quasi-3D model that the North branch was not included in the calculation. The calculation condition is absolutely the same.

In general, the difference between two methods of calculation is less than 10% of the velocity in the entire reach. The larger value is occurs at the edge of bank and central islands with steep slope, which is mainly influenced by different kind of mesh system. The orthogonal mesh used in quasi-3D model is denser than triangular mesh in 2DH model. At the location with steep slope, the one triangular may cover several orthogonal meshes, which inducing slight difference in velocity field. As a result, we basically think the 2 methods agree with each other well.

4.5.2 Influence of North Branch

In this model, because the North Branch was included in the calculation, which is differ from the quasi-3D model used in Chapter 2-3. At first, the influence of the North Branch was investigated. As shown in Figure 4.9, the time series of flow rate are exhibited at the cross-sections 1) before the bifurcation (blue), 2) after the bifurcation (red), 3) at the inlet of the North branch (green). The flow rate pass through the inlet of the North Branch is less than 1/10 of the main channel. We think the flow field and the sediment transport are rarely influenced by the North Branch. Therefore, the following investigation on calculation result is focus on the South branch after bifurcation.

4.5.3 Seasonal characteristics of water level

By changing inflow water volume, the flow rate at the upstream end Jiangyin controls the longitudinal distribution of water level in study area, and further influence the flow field.

Therefore, the water level distribution in different flow rate condition is investigated at first. In order to catch the main characteristic of water level changing process, 4 typical tidal phases at the downstream end Wusong are selected to display the longitudinal water level along the thalweg (Figure 4.10). They are the maximum flood (①), high water slack (②), and maximum ebb (③), low water slack (④) in sequence (marked in Figure 4.10-left). The water level in the dry season is lower than the flood season in general, especially at the upstream part, with a range of about 2m at each phase. The water level at the downstream end is similar, about 0.2-0.5m in difference.

During the ebb tide period (②→③→④), the water level shows integrate decrease. The seaward slope is large during the flood season and small during the dry season. During the flood tide period (④→①→②), the water surface slope shows opposite tendency. During the flood season, the intrusion of flood tide is restricted around 130KP. After 130KP, the landward slope is very mild. Before 130KP, the water surface slope is still seaward. In contrast, during the dry season, the reverse slope oriented upstream was very large, which is the largest in the a tidal period.

This phenomenon suggests that relative strength of flow rate and tide control the water level distribution. During the flood season, the tidal influenced range is limited by large amount of water inflow. In contrast, the tide influenced the entire reach during the dry season. The different water surface slope changes the flow field eventually, which will be discussed in the next part.

4.5.4 Seasonal characteristics of flow field

Secondly, the typical flow structure is exhibited in both flood season and dry season (Figure 4.11), which is similar to Figure 2.15. The green arrows are the averaged flow velocity in a tidal period (marked in Figure 4.6), which is re-arranged by reading the orthogonal grid system used in quasi-3D model. It is about 3km interval in horizontal direction and 100-300m interval in cross-sectional direction (Figure 4.11). The background is water depth under A.S.L. During the flood season, the average flow velocity in deep locations (in thalweg) is much higher than shallow locations (mainly above the shoals). During the dry season, the average flow velocity is quite small in both deep and shallow locations.

The same as Figure 2.15, the change of flow velocity is extracted every 10 minutes as red arrows from 5 cross-sections. Each cross-section includes 3 points, covering thalweg to underwater shoals. The number indicates right bank to left bank (face to downstream). The green arrow inside the red arrow groups is the averaged velocity in a tidal period (Figure 4.11). The basic relationship between velocity and topography is the same as qusai-3D model that the mainstream (a-1, b-3, c-2, d-1, d-3, e-2) shows almost simple oscillation, following the direction of thalweg, while remarkable cross-sectional component of flow are formed above large underwater shoal at the side of the thalweg (a-2, a-3, b-1, b-2, d-2, e-3). The main difference between the flood season and the dry season is the relative strength of reverse flow. In flood season, the seaward velocity was apparently stronger, which created a larger average velocity during a tidal period. In dry season, the landward velocity was significant and with longer duration, especially above the shallow shoals. As a result, the averaged value is very small in a tidal period.

In order to investigate the strength of reverse flow for the whole reach, a strength ratio R is defined as

$$R = \frac{\sum U_i^- h_i - \sum U_i^+ h_i}{\sum U_i^- h_i + \sum U_i^+ h_i} \tag{4.8}$$

where U_i is the along channel component of velocity. In order to handle the changes of water depth at every time step, the streamline flow rate $U_i h$ is used. $\sum U_i^- h_i$ is the integral of landward flow rate in a tidal period, $\sum U_i^+ h_i$ is the integral of seaward flow rate in a tidal period. The distribution of R is shown in Figure 4.12. The minus value represents the seaward flow and the plus value represents the landward flow. During the flood season, seaward flow occurs in almost the entire reach, including deep thalweg and shallow shoals. During the dry season, the value of R is much smaller than that during the flood season. The component of landward flow is similar to the seaward flow. The minus value of R is observed at several places above shallow shoals (encircled by solid line), showing landward movement in a tidal period. However, in most places, the average velocity is still point to downstream.

Next, the tracer experiment is used to investigate the characteristic of tracer distribution in a tidal period (Figure 4.13). The method is the same as tracer experiment 1 in 3.4. The start moment and end moment of the tracer experiment is determined by the average shear velocity

for the whole reach. Maximum shear velocity refers to start moment and the minimum velocity refers to end moment. It is a little bit different for the end moment in different season (Figure 4.13 (a)).

The center of tracer input locations is the same as 3.4. But the input region is cycle because it is much easier to define a cycle in the unstructured triangular mesh system. Two colors are used to distinguish the different source. The final distribution of tracer is displayed in Figure 4.13 (b). During the flood season, as discussed in 3.4, the tracer input in one spot moves to the next spot, with strong dispersion above the adjacent shoals. In contrast, during the dry season, the dispersion of tracer occurs around the input spots. As exposed in Figure 4.10, the degree of landward slope is larger in downstream reach than upstream reach. The distance of tracer movement in the upstream 2 spots is a little longer than downstream 2 spots. Here, the tracer experiment is only used to display the dispersion degree by flow field. It is not sufficient to discuss the sediment transport tendency during the dry season, because the transport mode is different from the flood season, which will be introduced in the next Chapter.

4.6 Summery

In this Chapter, a 2DH model was established to investigate the influence of flow rate to the pulsatile flow field. Two calculation periods are set referring the normal flood season and dry season. The calculation results suggest: 1) the flow rate mainly influence the upstream water level. The water level in dry season is about 2m lower than that of flood season, which changes the longitudinal water surface slope. The landward slope is larger at the high water slack in dry season than that of flood season. 2) the reverse flow in dry season is much stronger than flood season, which inducing relatively small average velocity in a tidal period. 3) In a tidal period, the average flow rate direction is seaward in thalweg and landward at several shallow places in dry season. In contrast, during the flood season, the flow rate direction is seaward in the entire reach. 4) By using tracer experiment, the movement distance in flood season is much longer than dry season, with stronger dispersion ability. In the next Chapter, the sediment transport calculation will be included in to 2DH model to investigate the characteristic of topography change in different season.

REFERENCE

Laursen, E. M.: The total sediment load of stream, *Proc. ASCE*, Vol. 84, Hy1, 1958.

Wang, Z.B., Louters, T. and De Vriend, H.J.: Morphodynamic modeling for a tidal inlet in the Wadden Sea. *Marine Geology*, Vol.126, pp.289-300, 1995.

Xie D.F., Wang, Z.B., Gao,S. and De Vriend, H.J.: Modeling the tidal channel morphodynamics in a macro-tidal embayment, Hangzhou Bay, China. Continental Shelf Research, Vol. 29, pp. 1757-1767, 2009.

赤穂良輔, 肖鋒: 非構造格子に基づく浅水流計算モデルの開発と数値実験, 水工学論文集, Vol. 54, pp.1153-1157, 2010.

赤穂良輔, 石川忠晴: 平成 23 年東北地方太平洋沖地震津波における利根川下流の津波遡上再現計算, 土木学会論文集 B, Vol.68, No.4, pp.I_1543-I_1548, 2012.

土木学会編: 水理公式集 平成 11 年版, pp.156-192, 1999.

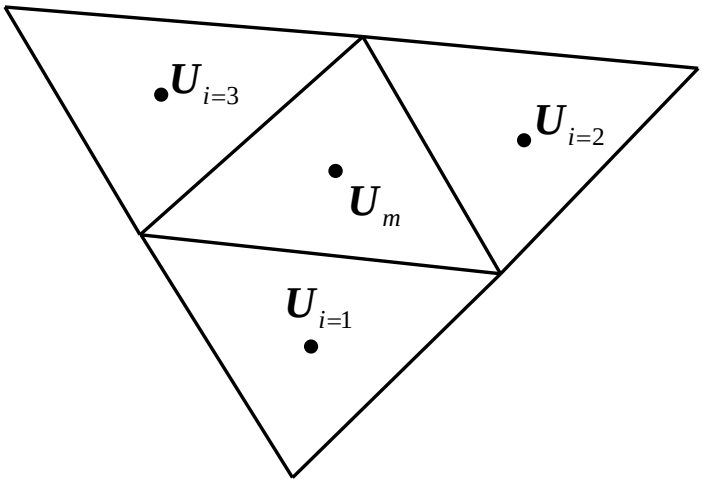

Figure 4.1 The relationship of $\boldsymbol{U}_m$ and $\boldsymbol{U}_i$

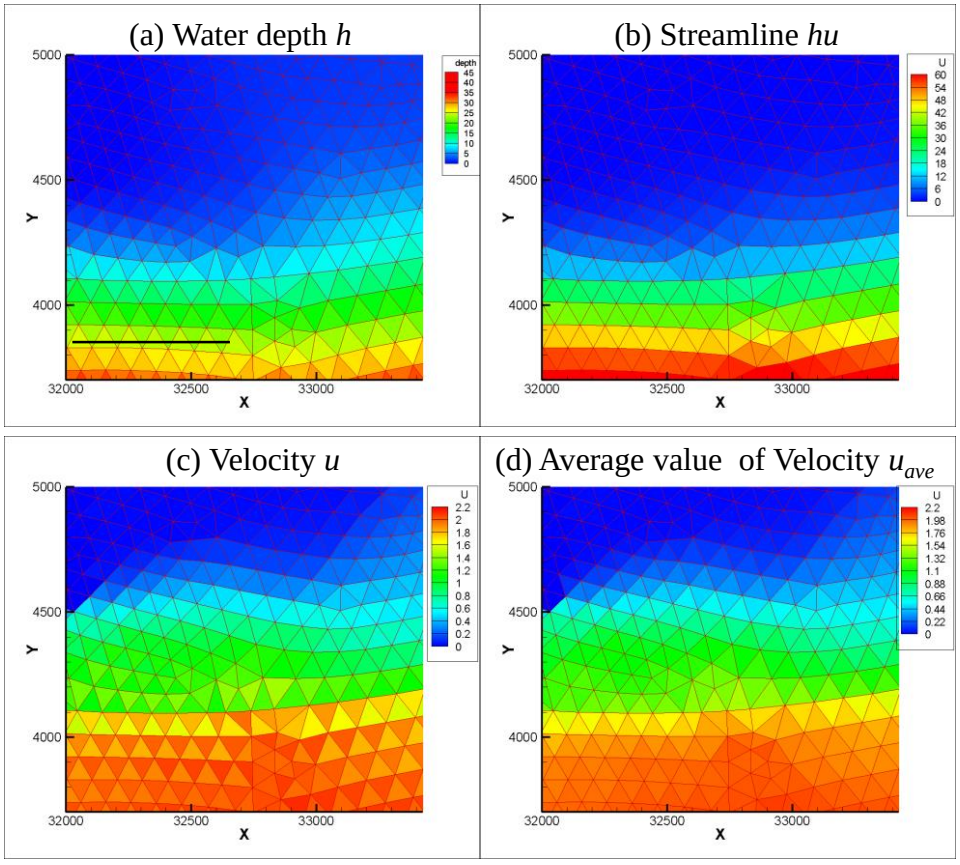

Figure 4.2 The relationship of (a) water depth *h*; (b) Streamline *hu*, (c) Velocity *u* and (d) average value of velocity u_{ave} which is used to explain the reason that u_{ave} is used instead of *u*

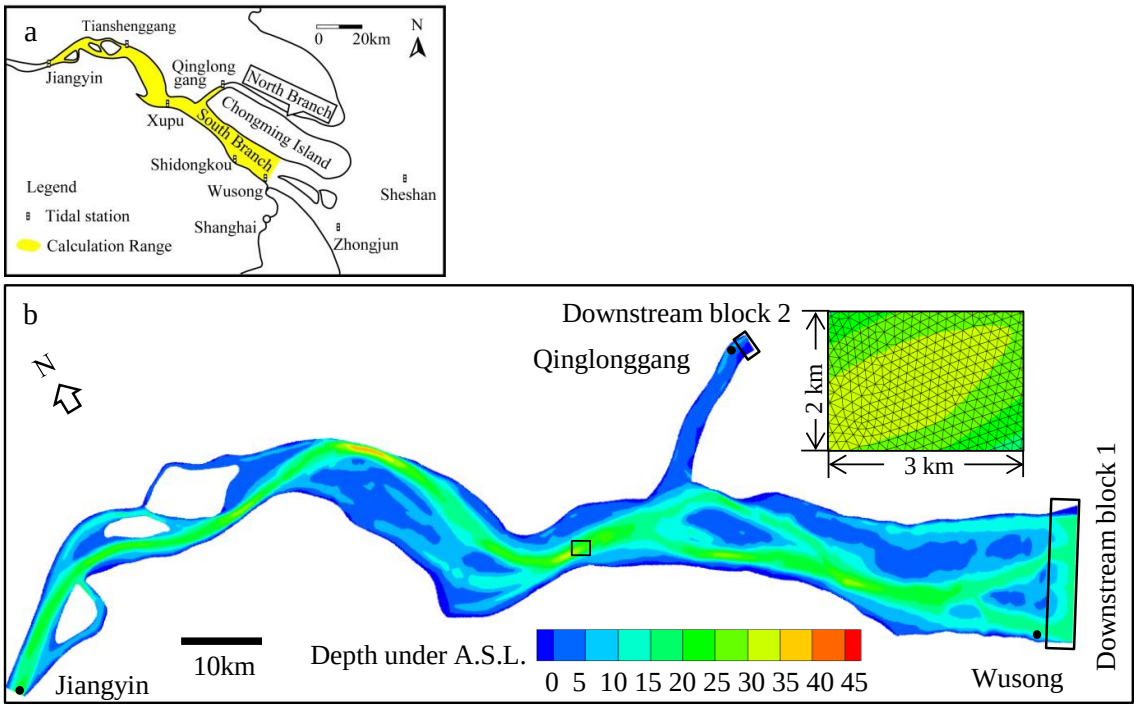

Figure 4.3 The topography of study area, and its location in Yangtze Estuary, with the example of mesh and the location

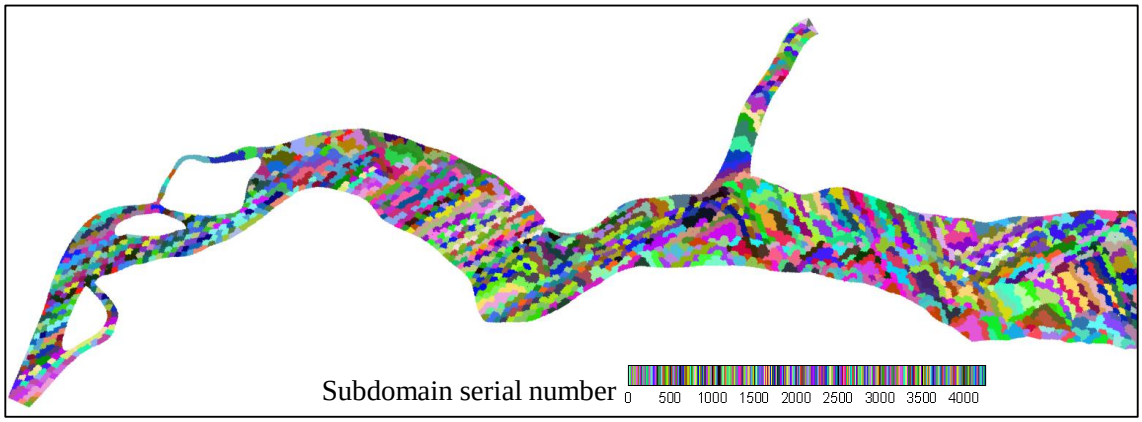

Figure 4.4 The subdomain division in study area

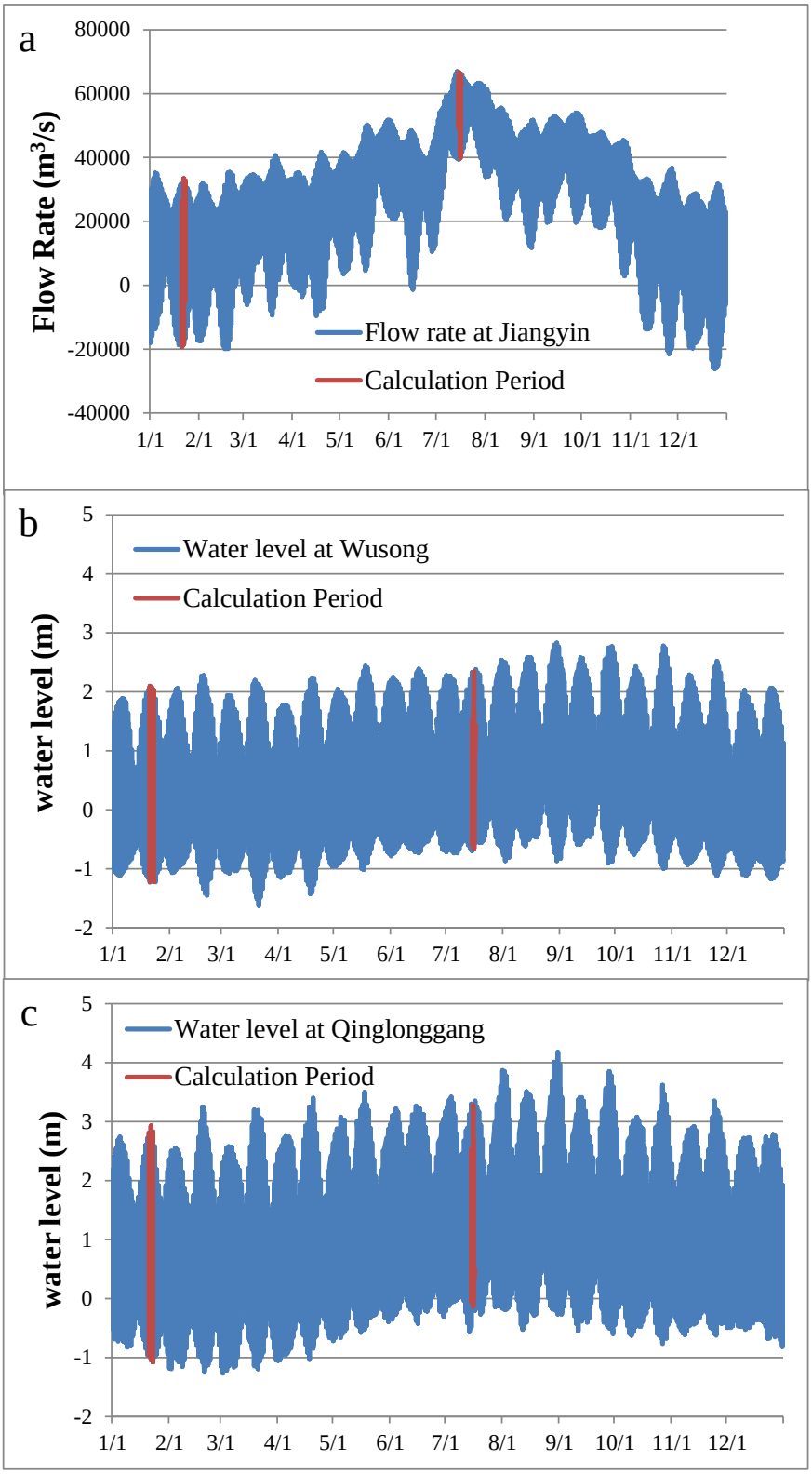

Figure 4.5 The yearly distribution of hydrological condition and the selected calculation periods a) Flow rate at Jiangyin b) Water level at Wusong c) Water level at Qinglonggang

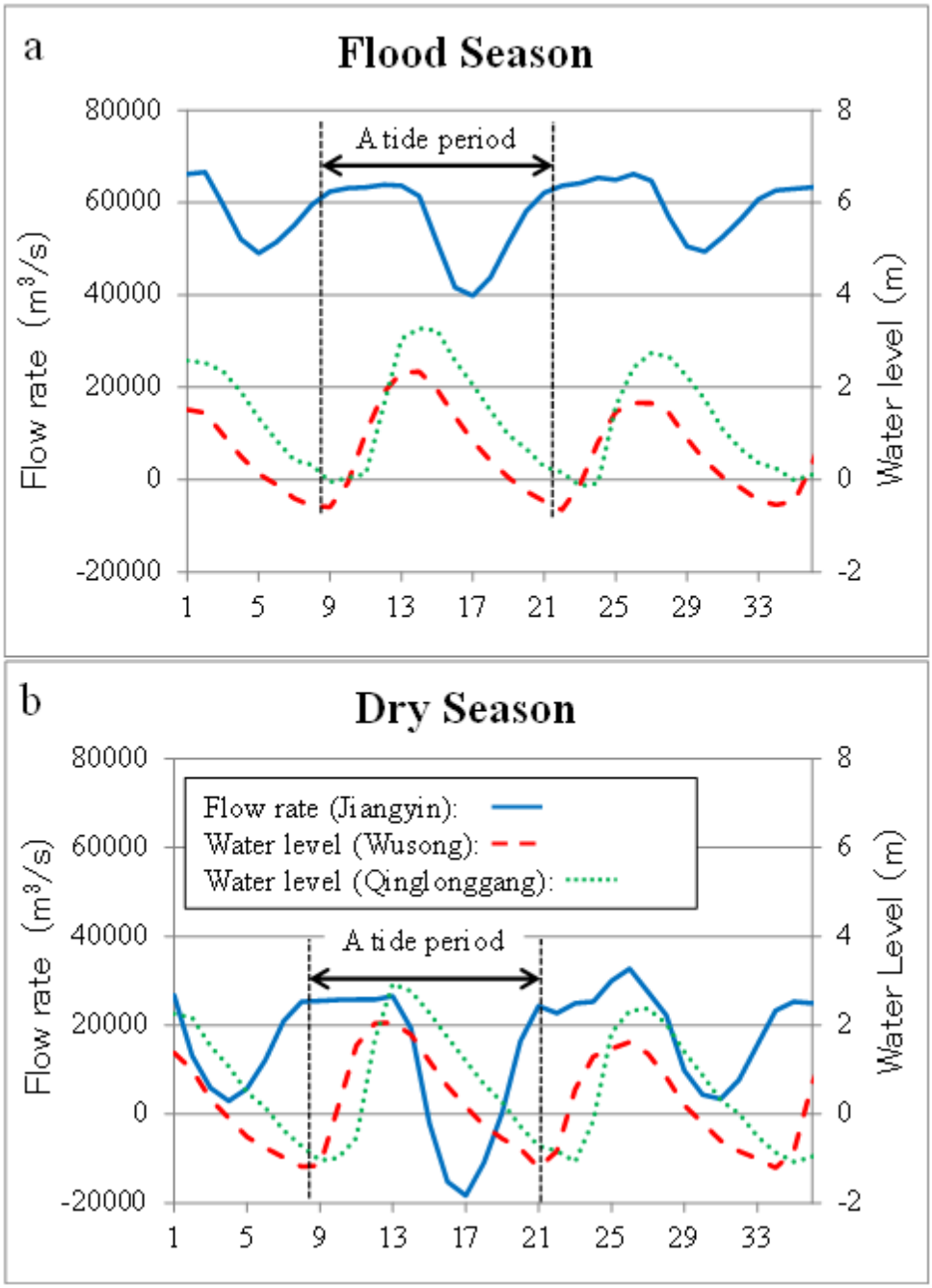

Figure 4.6 The enlarged figure of calculation condition a) Flood season b) Dry season

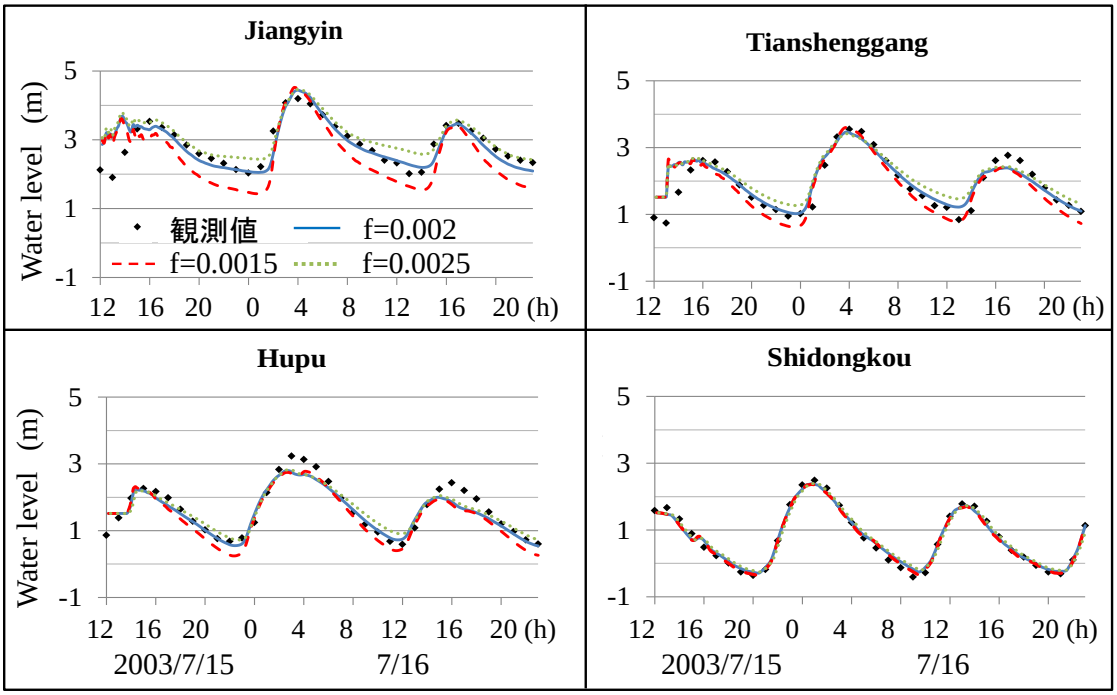

Figure 4.7 The calibration result of coefficient *f*

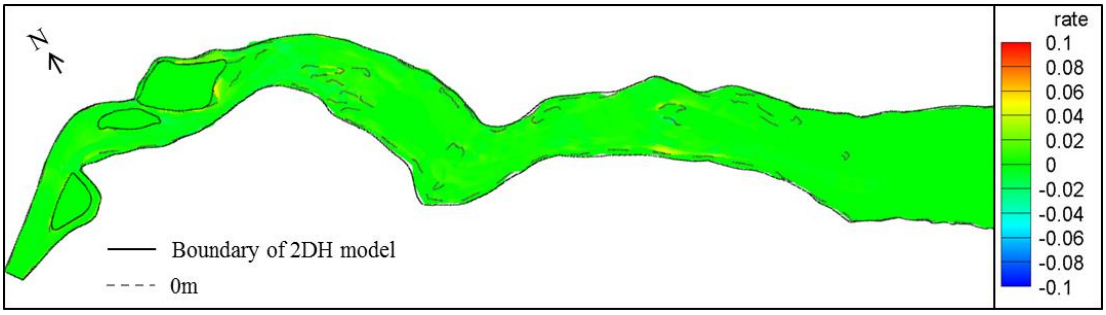

Figure 4.8 the maximum difference of velocity between two methods

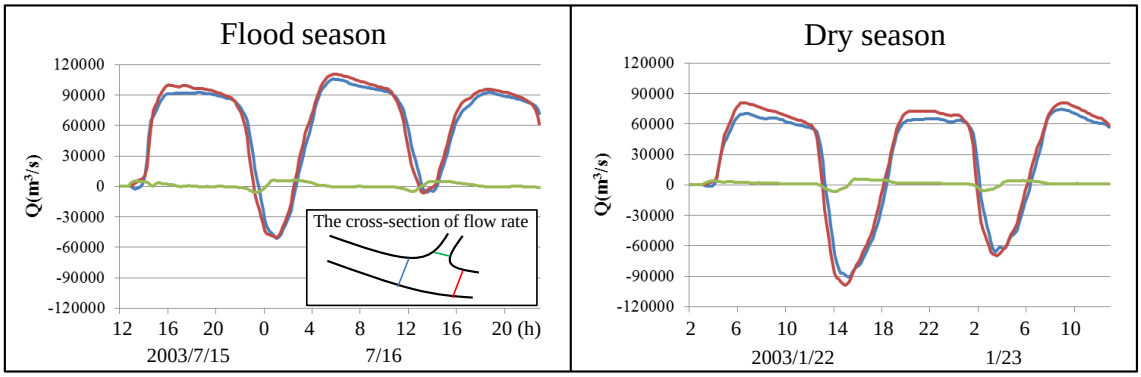

Figure 4.9 the flow rate comparison of the North Branch and South Branch. (Blue line indicates the flow rate before bifurcation; Red line indicate the flow rate in the South Branch; Green line indicate the flow rate in the North Branch)

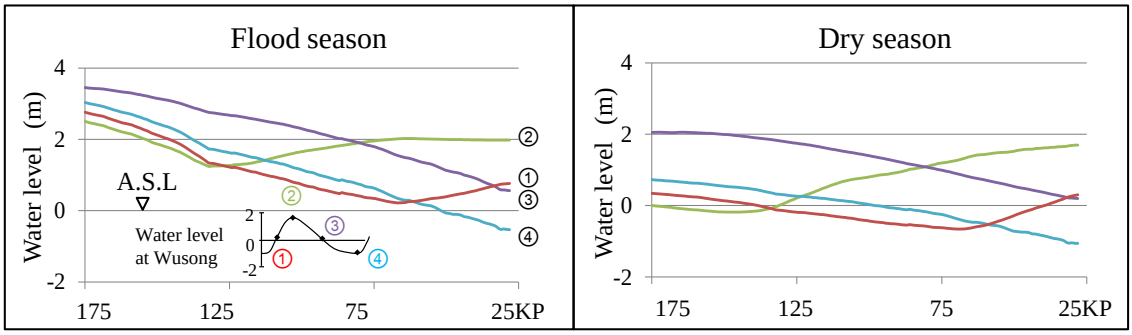

Figure 4.10 Water level distribution in flood and dry season

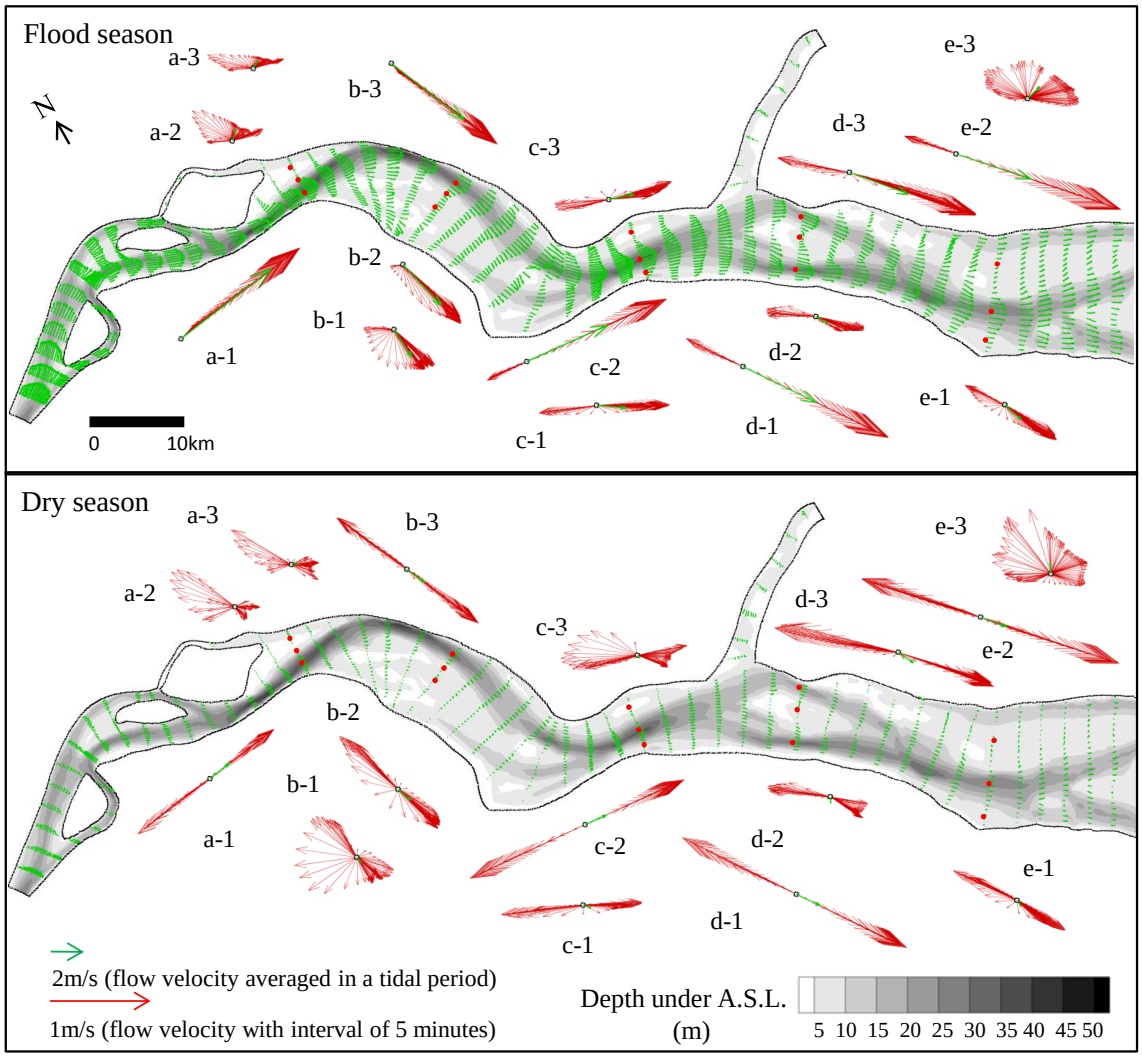

Figure 4.11 Average velocity and velocity change process in a tidal period in flood and dry season

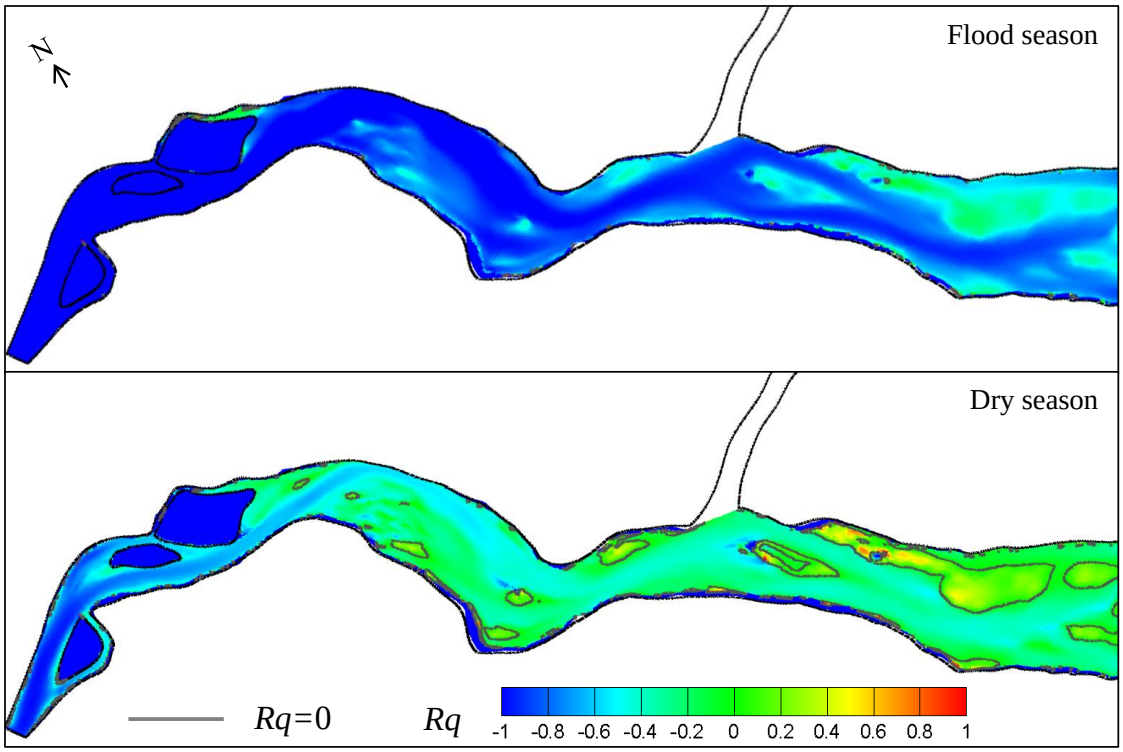

Figure 4.12 The strength ratio of flow rate direction

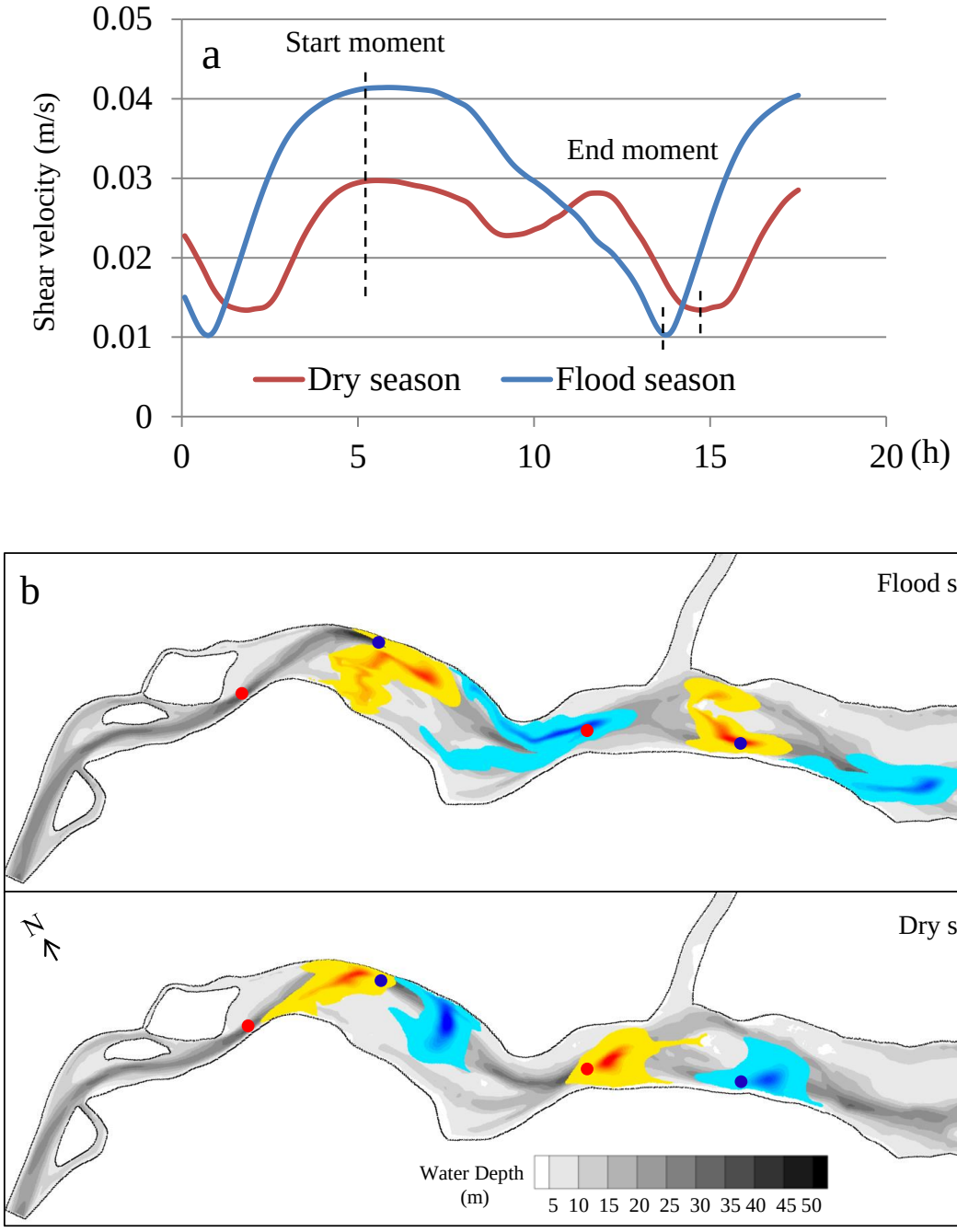

Figure 4.13 the result of tracer distribution a) the time serious of shear velocity averaged for the whole reach. The start moment and end moment is marked as dash line b) the distribution of tracer at the end moment. The input locations of the tracer is marked as solid cycles

Chapter 5 Seasonal characteristics of topographic change tendency

5.1 Sediment transport mode

In Chapter 4, the 2DH model was established to reproduce the flow field in both the flood season and the dry season, which laid the foundation to the discussion on topography change tendency. In Chapter 5, the sediment transport rate was included in to the 2DH flow model to model the morphological development in both seasons.

For the topography change calculation, some study suggests that the river bed erosion is limited due to the bed armoring (Cheng, 1985, Liu et al, 2002). But their solving methods are adding an experimental coefficient to erosion depth or applying detail calculation on grain-size change. For the former, the observation database is necessary to calibrate the coefficient. For the latter, our sampling density is not high enough to support this study. Both methods will increase the uncertainty for the calculation result. Therefore, we still use the uniform particle size of 150μm as representative bed sediment. The corresponding settling velocity is 0.016 m/s. The corresponding critical shear velocity u_{*cr} is 0.014m/s and critical shear stress τ_{*cr} is 0.081, which is calculated by Iwagaki equation (Japan Society of Civil Engineers, 1999).

The normalized frequency histogram of u_*/w_0 is also used to define the sediment transport mode. The distribution of u_*/w_0 is exhibited at the moment of 4 typical tidal phases in downstream end (the same as 4.5.2, marked also in Figure 5.1 (a)) in both the flood season and the dry season. Here, the hydrological condition of flood season and dry season is the real condition used in Chapter 4. The Vanoni's experimental bottom sediment concentration is also used to be the criteria of sediment transport mode (Vanoni, 1975). When $u_*>u_{*cr}$, the bed sediment is entrained. When $u_*/w_0>3$, the sediment transport mode is considered to be changed from bed load movement to suspended load movement. As discussed in 3.2, during the flood season, large shear velocity occurs in low water slack when seaward water surface slope is maximum, showing strong tendency of suspended sediment transport. The shear velocity decreases in flood tide period. The bed load movement becomes the major transport mode. The minimum shear velocity occurs in high water slack, large amount of sediment deposits (Figure 5.1 (a)). On the contrary, during the dry season, despite the tidal phase, the proportion of $u_*/w_0>3$ is quite small. Bedload movement is the major transport mode (Figure 5.1 (b)).

5.2 Sediment transport calculation

Considering the change of sediment transport mode of [deposition]~[bed load]~[suspended load], the experimental transport rate of bed material load is selected for calculation. To be honest, in most studies, the bed load and suspended load are studied separately, because of the different transport status. Actuary, it is a continual distribution without a definite boundary, which is called total sediment load (Laursen, 1958). It is slightly different from the sum of bedload of suspended load for the difference in definition (Japan Society of Civil Engineers, 1999). In our study area, due to tidal effect, the sediment transport mode changes, a single mode of bed load or suspended load cannot describe the entire movement of bed sediment. Therefore, the bed material load is adopted.

$$\frac{q_T}{u_* d} = \frac{7.66}{265\tau_{*c}}\left(\tau_* - \tau_{*c}\right) \times f\left(\frac{u_*}{w_0}\right) \tag{5.1}$$

where q_T is transport rate of bed material load (m^2/s); u_* is shear velocity; d is diameter of bed sediment; τ_* and τ_{*c} are the shear stress and critical shear stress; τ_{*c} is calculated by Iwagaki equation that $\tau_{*c} = 0.195R_*^{-7/16} = 0.014m/s$ when $R_* = \sqrt{(\sigma/\rho - 1)gd^3}/\nu = 7.38$ for the particle diameter of 150μm (Japan Society of Civil Engineers, 1999). f is a coefficient derived from experiment (Laursen, 1958) which relates to the ratio of shear velocity u_* and setting velocity w_0. The distribution of f is simulated by polynomial fitting (Figure 5.2).

$$\begin{aligned} f = {} & 0.0018 \times \left(\frac{u_*}{w_0}\right)^5 - 0.1136 \times \left(\frac{u_*}{w_0}\right)^4 + 2.0925 \times \left(\frac{u_*}{w_0}\right)^3 - 3.4983 \times \left(\frac{u_*}{w_0}\right)^2 \\ & + 11.185 \times \left(\frac{u_*}{w_0}\right) + 5.0879 \end{aligned} \tag{5.2}$$

The evolution of bed topography is governed by the sediment continuity equation:

$$\frac{\partial z}{\partial t} + \frac{1}{1-\lambda}\left(\frac{\partial q_{bx}}{\partial x} + \frac{\partial q_{by}}{\partial y}\right) = 0 \tag{5.3}$$

where z is bed elevation; λ is porosity of bed material; q_{bx} and q_{by} are the bedload transport flux per unit width in x- and y- directions.

For the discretization, the finite volume method is used:

$$q_{T\,i}^{\,n+1} = q_{T\,i}^{\,n} - \frac{\Delta t}{\Delta s_i (1-\lambda)} \left(\sum_{j=1}^{3} \boldsymbol{E}_{q_T} \cdot ndl_j \right)_i^n \qquad (5.4)$$

$$\boldsymbol{E}_{q_T j} = 0.5 \times \left(q_{Tj} + q_{Tm} \right) \quad (j = 1,2,3)$$

where q_T is the transport rate of bed material load at the center of triangle mesh; E_{qT} is the transport rate at each side of the triangle, which is the average value of adjacent 2 triangles (Figure 5.3).

5.3 Calculation condition

The same as Chapter 3, the periodical condition is used for topography change calculation to eliminate the fluctuation of semidiurnal tides. The calculation condition is shown in Figure 5.4. The dash line and dotted line is the normalization result of water level at downstream ends. The solid line is periodical flow rate at upstream end. It is calculated by applying the periodical water level of Jiangyin to the 1D unsteady flow model, which is introduced in 2.3.4. The second tidal period is used to display the characteristic of sediment transport.

The bank erosion was not included in calculation, because in our study area, the artificial dykes covered the entire reach, including the large center islands. So in our calculation, the boundary which is protected by artificial dyke is set to be unmovable.

5.4 Calculation result and discussion

5.4.1 Sediment transport process in a tidal period

From Figure 4.11, the flow velocity rotates in a tidal period in both seasons. The component of reverse flow in dry season is larger than the flood season. In deep thalweg, the velocity appears simple oscillation, following the direction of thalweg axis. Above shallow shoals, the rotation tendency is more obvious. However, the 15 examples of velocity change process as red

arrows are not enough to represent the entire reach. In order to get the characteristic of sediment transport tendency, it is necessary to use an index which can be applied for the entire reach.

First, the average angle of sediment transport direction is calculated for a tidal period. This angle means the angle between the sediment transport vectors at each moment to the axis of average sediment transport vector. After all the angles in a tidal period are calculated, it is averaged to make the Figure 5.5. The larger the average angle, the larger the cross-sectional component of sediment transport. If the average angle is close to 0, the sediment is simply moves back and forth. The broken line is the contour line of -5m of topography. It is obvious that the angle is small along deep thalweg, and large above the shallow shoals, showing strong cross-sectional sediment transport above the shoals. Comparing the angle above the shoals, it is larger during the dry season than that of the flood season, which indicates cross-sectional movement of bed sediment is stronger during the dry season.

Next, in order to distinguish seaward/landward direction of sediment transport in different season, a strength ratio R_q is defined similar to R in 4.5.3 (Figure 5.6).

$$R_q = \frac{q_T^- - q_T^+}{q_T^- + q_T^+} \tag{5.5}$$

where q_T^- is the integral of the landward sediment transport rate in a tidal period, q_T^+ is the integral of the seaward sediment transport rate in a tidal period. During the flood season, seaward transport of sediment occurs over almost the entire reach, including deep thalweg and shallow shoals. During the dry season, minus value of R_q is observed above shallow shoals (smaller than -5m contour line), showing landward transport of sediment. Meanwhile, the seaward transport of sediment still occurs in the thalweg. In the dry season, the transition area between the thalweg and shoal is sensitive due to the conjunctions of seaward transport and landward transport of bed sediments.

The trends in topographic changes can be discussed with respect to the average of effective shear stress, τ_{ave} in a tidal period. The horizontal distribution of the sediment transport rate is a more direct index; however, due to the nonlinear relationship between the shear stress and sediment transport rate, the range of values for the latter is much larger. Hence, the distribution cannot be clearly determined, so we substituted in the average of effective shear stress (τ_{ave}), which is defined as follows:

$$\tau_{ave} = \sum_{t=1}^{T} \tau_t \Big/ T \quad if\left(\tau_t > \tau_{*cr}\right) \tag{5.6}$$

where τ_t is the shear stress at each moment output file, τ_{*cr} is critical shear stress equal to 0.081, introduced in 5.1. T is a tidal period.

4 segments during the dry season were extracted for their unique distribution of τ_{ave}. The locations of these 4 segments are marked in Figure 5.6, are the aggregations of the seaward sediment transport and the landward sediment at the transition between the thalweg and shoal. When the sediments traveling in opposite directions collide, the distribution of τ_{ave} shows a horizontal vortex (Figure 5.7 (b)). This phenomenon may be responsible for shoal deformation. In contrast, during flood season, the seaward transport of bed sediment occurs over almost the entire reach (Figure 5.6 (a) and Figure 5.7 (a)). The tendency of topographic change is similar to a normal river with unidirectional flow.

As a result, the topography change process for these segments during the dry season is shown in Figure 5.8. The calculation continues for 4 months. At the location of vortex, a long and narrow sandbar appears and extended from the large shoal, which is called sandspit. Once the sandpits appear, they develop and penetrate to thalweg due to the effect of sediment transport vortex during the dry season. In contrast, during the flood season, the sandspit is hard to be formed (Figure 5.9). The flow transport sediment from thalweg to the underwater shoal to deposit continuously, with the development of alternate bars. The topography change tendency is that the shoals become larger and the thalweg become deeper.

5.4.2 The existence of sandspits in references

The study on the topography change in the estuarine channel of Yangtze River is quite scattered and rough as introduced in 1.4. Most studies rely on the nautical maps. The map publish is unsystematic, with about 5-10 years interval. The observation for one series of maps also takes a several months. For example, the nautical maps we used to make the topography for calculation are measured in March-July in 2000. The seasonal characteristic cannot be reflected from these figures. To be honest, the nautical maps are also hard to be obtained in China for science. For this study, we only obtained a series of nautical maps. It is used to make the topography database. Here, the discussion on topography evidence mainly relies on the results

from references which using nautical maps to study. The publish year of the nautical maps they use and the contour line they focus on are different with each other.

For Segment 1, the evidence is the -12.5m contour line in 1998 and 2006 reported by Jiang et al, 2011. The -12.5m counter line in calculation results are also shown in both flood season and dry season (Figure 5.10). In calculation, we noticed the meandered thalweg transported to downstream with relative smooth tendency during the flood season (Figure 5.10 (a)), while a small sandspit appears at the edge of thalweg and shoal during the dry season (Figure 5.10 (b)). In the observational figure of topography, a sandspit is observed at almost the same location in both 1998 and 2006 (marked by cycle in Figure 5.10 (c)).

For Segment 3, we have two evidences. One is the -5m contour line in 1998 and 2002, reported by Yun, 2004 (Figure 5.11). Another is -10m contour line in 2002 and 2008, reported by Xu and Chen, 2009 (Figure 5.12). In calculation, the topography change tendency is similar to Segment 1. The outline of the underwater shoal changes smoothly during the flood season (Figure 5.11 (a) and Figure 5.12 (a)), while during the dry season, a sandspit appears and extended with the times development of calculation (Figure 5.11 (b) and Figure 5.12 (b)). At the almost the same location, a sandspit is observed and transport to downstream in the observational topography figure in both -5m contour line (Figure 5.11 (c)) and -10m contour line (Figure 5.12 (c)), marked by cycle. It seems that the shape of sandspit is much clearer by -5m contour line in observation. The -10m contour line is smooth. Only the convex outline of the shoal can be seen.

For Segment 4, the observational topography change is smooth, with the seaward movement of the convex outline of shoal (marked by rectangle Figure 5.11 (c)). We think the sandspit might appear in dry season, but it deforms to be smoother and transports to downstream in the next flood period. The detail discussion on long terms topography change is in next part.

Unfortunately, the observation records do not include Segment 2. However, another sandspit is observed at the opposite bank and a little bit downstream to the Segment 2 (marked in ellipse in Figure 5.11 and 5.12). This tendency appears during both the dry season and the flood season. The reason is considered to be the development of alternate bar, which is obvious after a big turning point of main channel (referring topography in Figure 4.3).

The above discussion listed several evidences in the existence of sandspits. However, the exact locations or changes tendencies cannot be reproduced by the calculation separately during

the flood season and the dry season. Actuary, the natural topography change is controlled by long term hydrological condition including both flood season and dry season. In the next part, we discuss the topography effect after the development of sandspits.

5.4.3 Influence of sandspits

Next, we investigate the changes of flow field after the development of sandspits. We compare the flow field during the flood season to different initial conditions: (1) from the original topography, digitized from navigation maps, resulting in relatively smooth interpolation (Figure 5.13 (a)), and (2) the resulting topography after 4-month calculations for the dry season, where the sandspits developed at several locations (Figure 5.13 (b)).

The velocity field at the moments of maximum ebb and the turning point from ebb to flood are displayed for both calculations with different initial topography (Figure 5.14). At the maximum ebb, the velocity distribution was similar, despite the existence of sandspits. The velocity at the maximum ebb was about twice as lager as that of the turning moment from ebb to flood, so half of the cross-section is displayed for clearer view. At the turning moment from ebb tide to flood tide, the reverse flow in shallow locations normally begins slightly ahead of that in deep locations. The velocity above the underwater shoals is landward; however, the velocity in the thalweg is still seaward. If sandspits do not exist, then the velocity simply changes direction at the transition zone between the thalweg and shoal. If sandspits exist, then a horizontal vortex appears downstream of sandspit, which may promote the development of sandspits.

Then we can roughly summarize the possible topography change process that the sandspits appear during the dry season, while it develops continually and transport to downstream during the next flood season. In the next part, a simplified long-term topography calculation is applied, and its results are compared to the historical evidence in topographic changes collected from references.

5.5 Long term topographic change tendency

In this section, a long-term topography change is proposed to investigate the motion of sandspits in different season. Here we do not use the yearly observational data directly, because it is hard to get a general characteristic of topographic changes. We still use periodical conditions, with representing flow rate of flood season (summer), dry season (winter) and transitional season (spring and autumn) in 50 years. The selection of the calculation period is marked in Figure 5.15. Period ① is used for December to March; Period ② is used for April to June, Period ③ is used for July and Period ② is used again for August to November to get a one-year circulation.

The resulting topography in different season is represented in Figure 5.16 by the counter line -5m. The locations of sandspits developed in winter are marked by cycles (Figure 5.16 (a)). After the calculation of spring (Figure 5.16 (b)), summer (Figure 5.16 (c)) and autumn (Figure 5.16 (d)), the sandspits still existed and developed in the downstream direction. The vortex at the turning moment from ebb to flood tide may have contributed to the development of sandspits. The large seaward velocity in the ebb tide contributed to the seaward movement of the sandspits. By checking the observational topography in reference studies (Yun, 2004; Xu and Chen, 2009), the seaward movement of sandspits was also observed Segment 2-4 (Figure 5.11 (c) and Figure 5.12 (c)). Downstream movement of sandspits is clear in Segment 3, but not obvious in Segment 2 and 4. However, the downstream movement of convex counter line is observed at Segment 4. One possible explanation may be that the real hydrological condition is more complicated than the simplified way in our numerical experiment. The sandspits may be developed at other depth levels which were not recorded by the reference. As to the Segment 1, only -12.5 m of observational topography was collected (Figure 5.10 (c)), and the development of sandspits was not obvious at this counter line.

Normally, calculations of topographic change have a relatively larger range of error. The data presented here on sandspit development are no more than a qualitative presentation under simplified hydrological conditions. However, this study provides a possible explanation of topography change due to variation in flow rate variation and tidal influences in the estuarine channel of Yangtze River. Next, we try to discuss other evidences for the long-term topographic changes.

Firstly, the development of sandspits at the location of Segment 1 induces the enlargement of shoals and erosion in concave bank. The thalweg is deepened and approach to the concave bank. Although in our calculation, the boundary is fixed, this place has a tendency of strong side bank erosion from our calculation result. In fact, it is just the most dangerous places of Yangtze estuary in history. According to Yun et al, 1988, the side bank erosion occurs several times before 1920. After that, this place has been protected by a serious of spur dikes. The bank erosion is controlled. But the deepest line still moves to the concave bank with the speed of 50-100m/year, which agree with our calculation result.

The similar situation happens on the location of Segment 2, where due to the development of sandspits, the left-side shoal appears progradation and the right shoal appears recession. However, the recession at the right side is not obvious. This place is also one of the most famous nodes in Yangtze Estuary, not only for its good geological condition (The right-side bank is composed by think clay layer with high erosion resistance) but also for the continual protection since 1754 (Yun et al, 2004; Xu and Chen, 2009). Recently, although the thalweg is deeping and narrowing with right-side movement, the bank is stable.

The seaward development of sandspits at the location of Segment 3 is clearly to be seen by the -5m contour line in the historical records by Yun et al, 2004 (Figure 5.11 (c)). However, the evidences of sandspits have not been paid any attention to. At the location of Segment 3, so called Baimaoha Shoal, the topographic change studies suggest that the shoal have a northward move tendency. Actually, this result is derived from the measurement of the distance between -5m counter lines at both the north channel and the south channel (marked in Figure 5.17). The change of distance with time is listed in Figure 5.18. Among the 4 lines, only the distance at the entrance of the south channel has an obvious trend of being large. The other 3 lines have no obvious tendency. If we take the development of sandspits into consideration, the characteristics of topographic changes here is the migration of mainstream due to the influence of sandspits. In Figure 5.17, we displayed the streamline at the maximum ebb by different topography. The gray line refers the initial topography with no sandspits. The red line refers the resulting topography after 4-month calculation for dry season with the development of sandspits. In the latter condition, the streamline at the south channel shows more meandering. Especially at the entrance of the south channel, it is pushed towards north quite a lot. The stream line at the north channel only changes a little. We believe the change of streamline at the south channel

contributes to the erosion at the south edge of Baomaosha, which inducing the enlargement of the entrance of south channel, and agree with the historical records.

At the location around Segment 4, the topographic changes were very complicated in history. Several waterways develop, deform and disappear continually. The location of shoal and waterway changes in a short period, which causes difficulty to navigation. In Figure 5.19, two waterways can be observed in recent nautical maps. The Lateral waterway and the North center shoal waterway. The former researchers claimed that the waterways appear due to the axis change of the main stream. With the deposition at the tail of Upper shoal and the erosion at the head of the Lower shoal, the waterway move to downstream and changes its direction gradually. When it became hard for the water to go through, another waterway was cut at the upstream of the former waterway. The Figure 5.20 list the distance between the entrance of the North center shoal waterway to the Shitousha station (red line) and the angle between the North center shoal waterway and the North direction (blue line). This data is much older than our topography data (Chen et al, 1988). The locations of the waterways were also different. However, the development of waterway was obvious. 2 cycles can be observed. For each cycle, the waterway moved towards downstream with smaller angle from the North direction (Larger angle from the South Branch). In 1950th, a sudden change happened that the waterway moves upstream with a large angle from the North Branch. We suppose at that time, a new waterway is cut and substitute the old one. The location is similar, so they used the same name. In the current nautical map, another waterway (Lateral waterway) was cut at the upstream of the North center shoal waterway. In our calculation result, we observed that one streamline from the north channel of Baimaosha turn its direction onto the Bianshansha shoal at maximum ebb with large velocity (Figure 5.21). Although an entire shoal was observed by -5m counter line, several small waterways exist by -2m counter line. After the development of the sandspits, the streamline changes its direction to a waterway downstream than the former one. In topography, it looks like the old waterway moves toward downstream.

In this section, we listed several phenomena of topographic change in historical records, which were summarized by the former researchers. Due to the lack of observational data, these phenomena have not been explained well in the former studies. In the present study, we took the development of sandspits into consideration. The changes of flow structure can also explain

these phenomena reasonably, which suggest the sandspits may be a key of topographic change in this reach.

5.6 Summery

In this chapter, the topographic change process is composed into the 2DH model by using total sediment rate. Two periodical hydrological conditions are applied representing the typical flood season and the dry season, respectively. The calculation result suggests 1) seaward sediment transport in the entire reach during the flood season. In contrast, during the dry season, it shows the opposite tendency in the thalweg and above underwater shoals. At the transition zone between thalweg and shoal, sandspits develop. 2) the sandspits continued to develop and move towards downstream during the next flood season, which can also be observed at the nautical maps collected in references 3) the phenomena of topographic change summarized by the former researchers can also be explained by the development of sandspits, which infer the existence of sandspits may a key factor in the development in the Yangtze Estuarine Channel.

REFERENCE

Chen, J.Y., Pan, A.D., Su, F.C. and Xu, H.G.: The topographic change analysis in the North Channel of the Yangtze Estuary. In Chen, J.Y., Shen, H.T. and Yun, C.X. eds, Process of Dynamics and Geomorphology of the Changjiang Estuary (in Chinese). *Shanghai Scientific and Technical Publishers*, pp.390-403, 1988.

Cheng, K.J.: An intergrated suspended load equation for non-equilibrim transport of non-uniform sediment, Journal of Hydrology, Vol. 79, pp. 359-364, 1985

Jiang, N.L., Chen, Y.P., Fei, X.A. and Zhang, C.K.: The analysis of topography change of Tongzhou Shoal and Langshan Shoal water way in Yangtze Estuary (in Chinese). Proceeding of China ocean engineering. pp. 1160-1163, 2011.

Laursen, E. M.: The total sediment load of stream, *Proc. ASCE*, Vol. 84, Hy1, 1958.

Liu, J.M., Wang, S.Q. and Wang, G.Q.: A study on non-equilibrium sediment transport process of long distance erosion in fluvial river, Journal of Hydrological engineering (Chinese), No. 2, pp.47-53, 2002

Vanoni, V.A.: Sedimentation engineering. ASCE, New York, 418 pp. 1975.

Xu, Z.M. and Chen, Q.H.: Research on regulation scheme for Xuliujing joint - Baimao sha section of the Yangtze River (in Chinese), *Yangtze River*, Vol. 40, No. 13, 2009.

Yun, C.X., Hu, J.M. and Zhou, D.S.: The topographic change analysis in the Nantong Reach of Yangtze Estuary. In Chen, J.Y., Shen, H.T. and Yun, C.X. eds, Process of Dynamics and Geomorphology of the Changjiang Estuary (in Chinese). *Shanghai Scientific and Technical Publishers*, pp.358-374, 1988.

Yun, C.X: recent developments of the Changjiang Estuary (in Chinese), *Ocean press*. pp.290, 2004.

土木学会編: 水理公式集 平成 11 年版, pp.156-192, 1999.

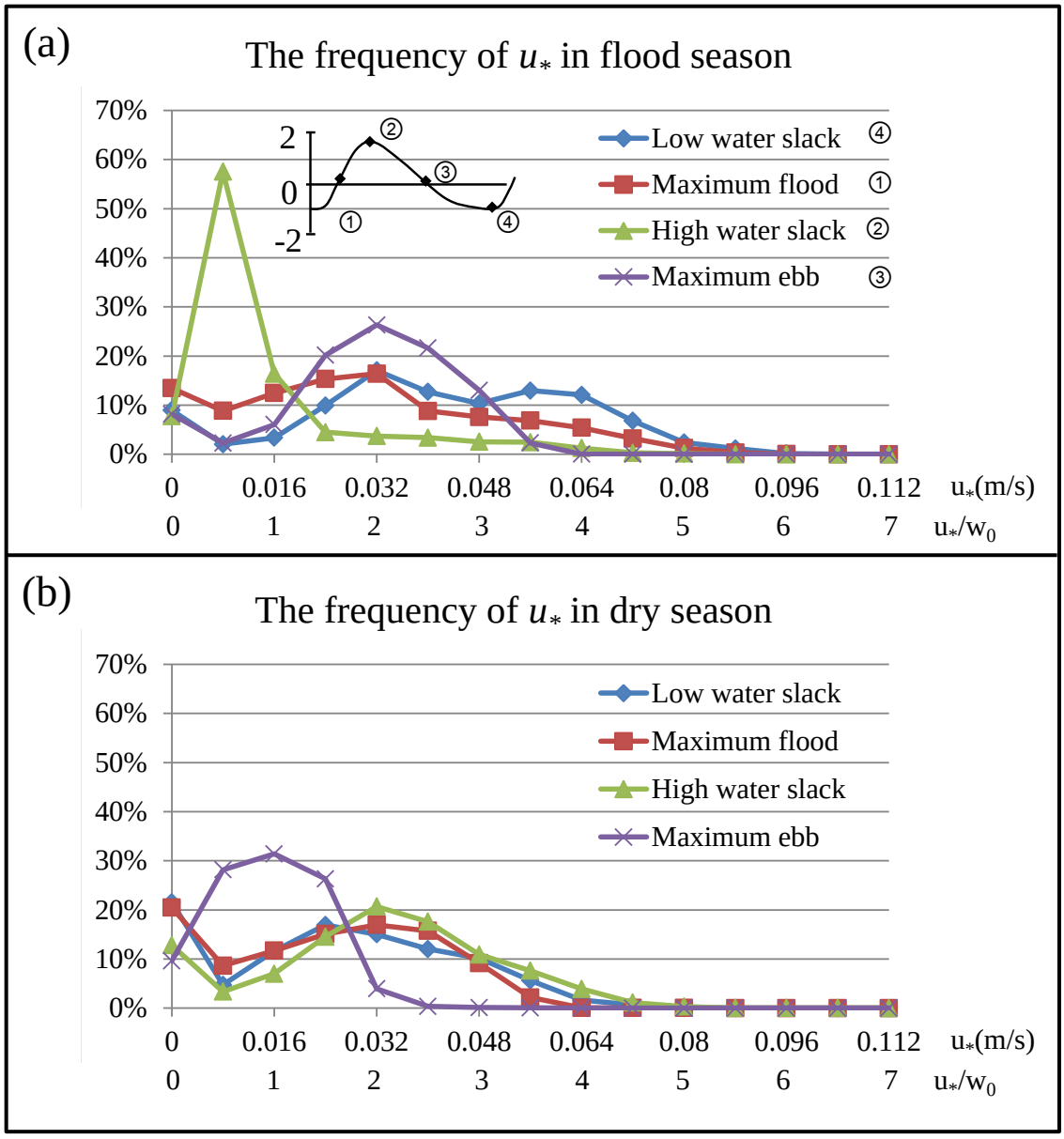

Figure 5.1 The frequency distribution of u_*/w_0

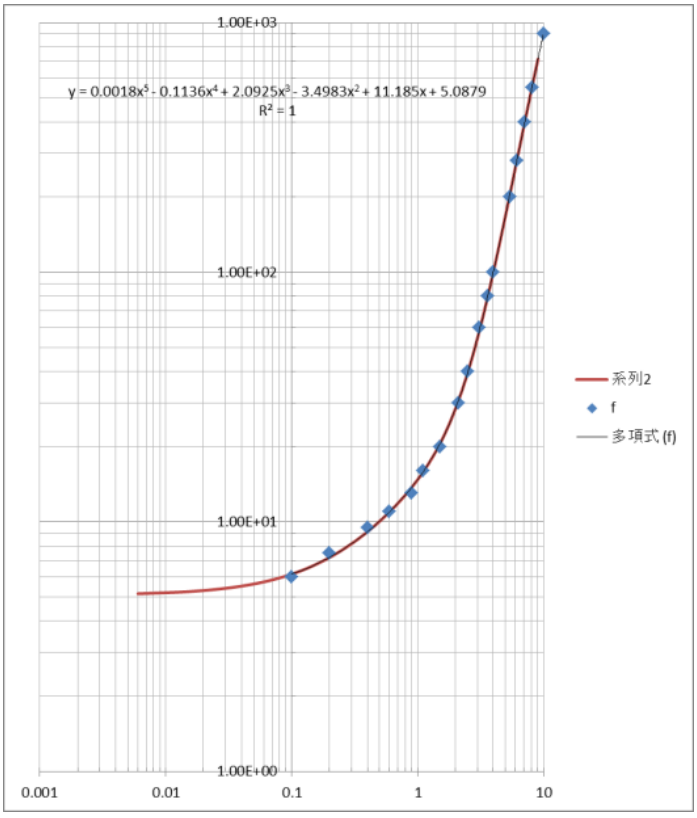

Figure 5.2 The polynomial fitting of the coefficient *f*

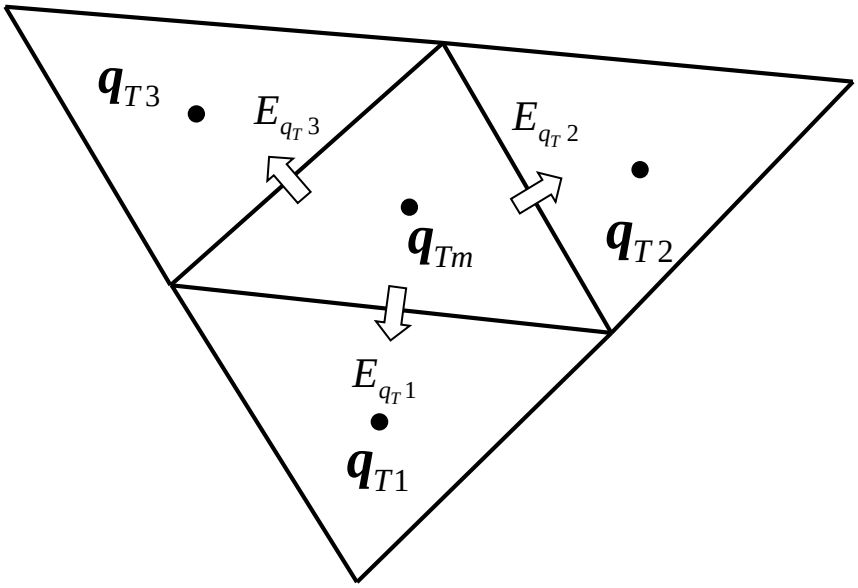

Figure 5.3 The sketch of sediment transport calculation in the unstructured triangular system

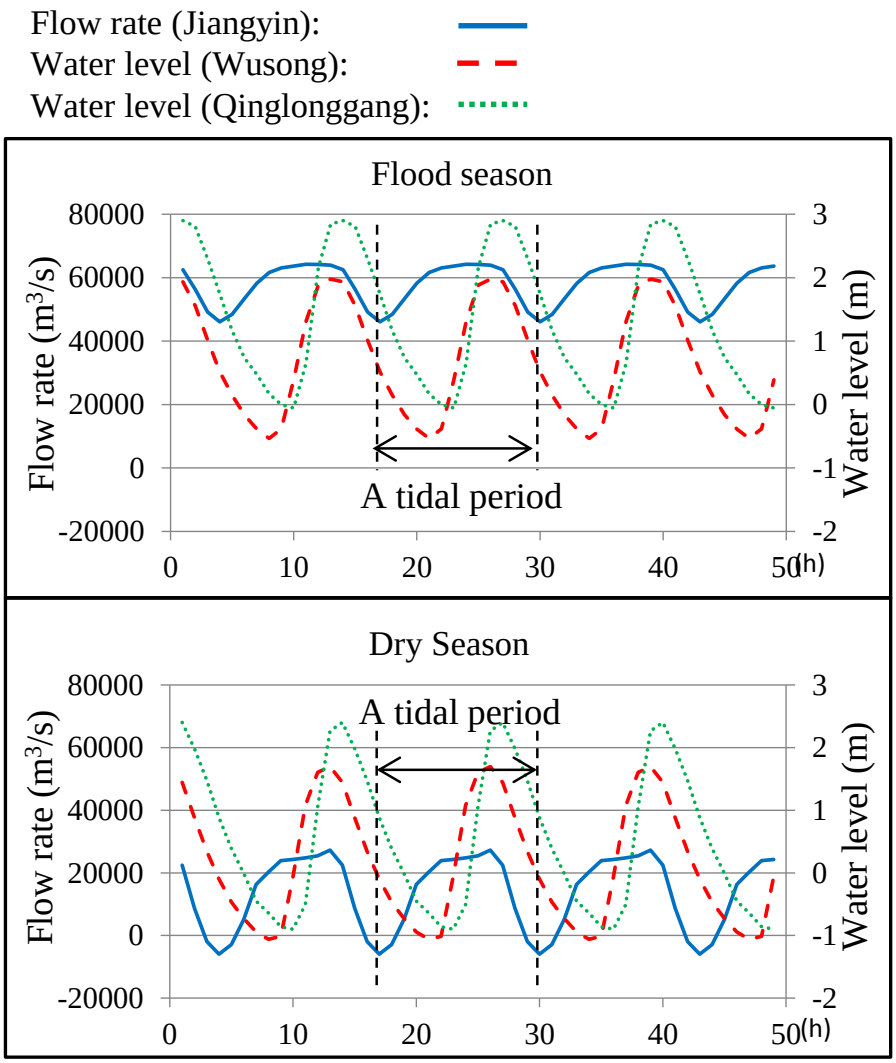

Figure 5.4 The periodical condition of topography change calculation a) Flood season b) Dry season

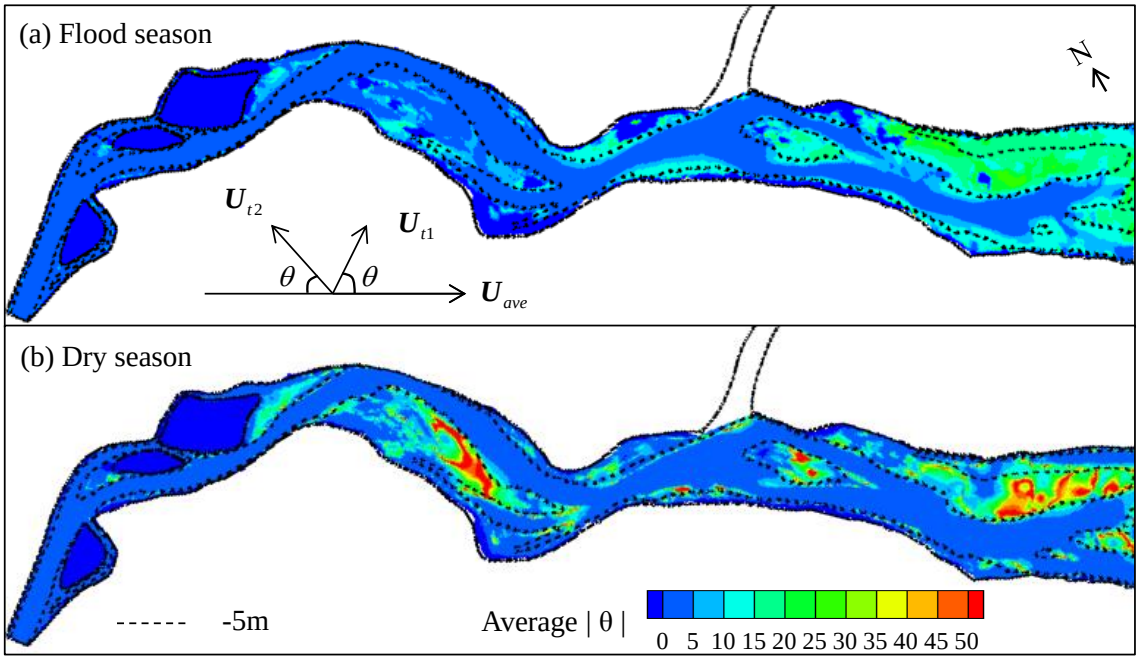

Figure 5.5 The average angle of sediment transport direction to the axis of channel. The definition of θ is the deviation from average sediment transport vector change from 0º to 90º

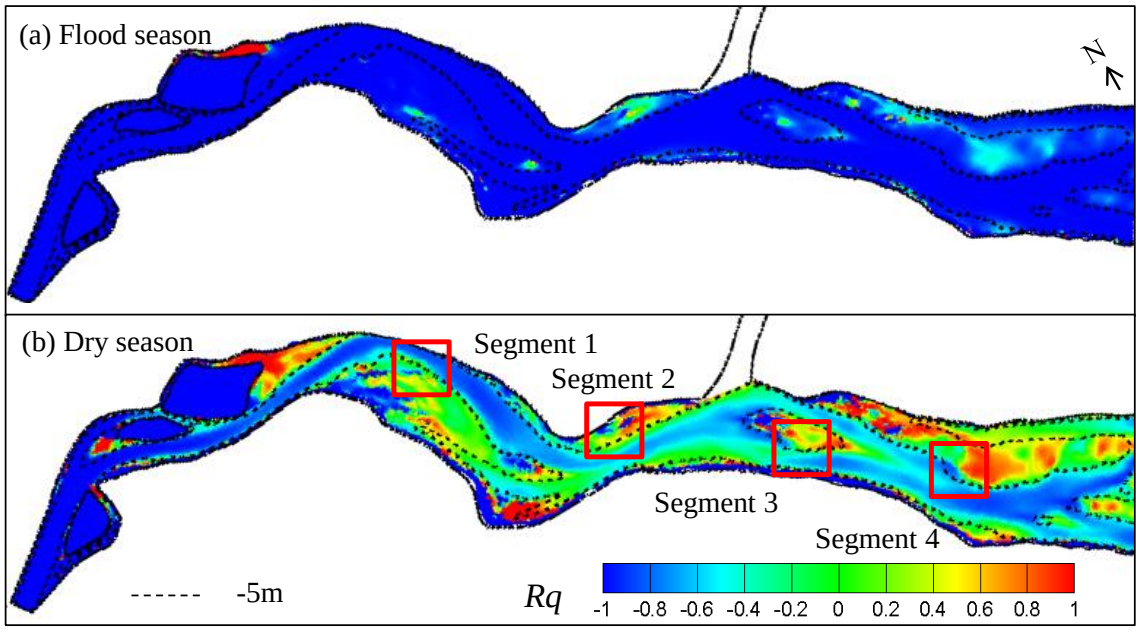

Figure 5.6 The strength ratio of sediment transport direction

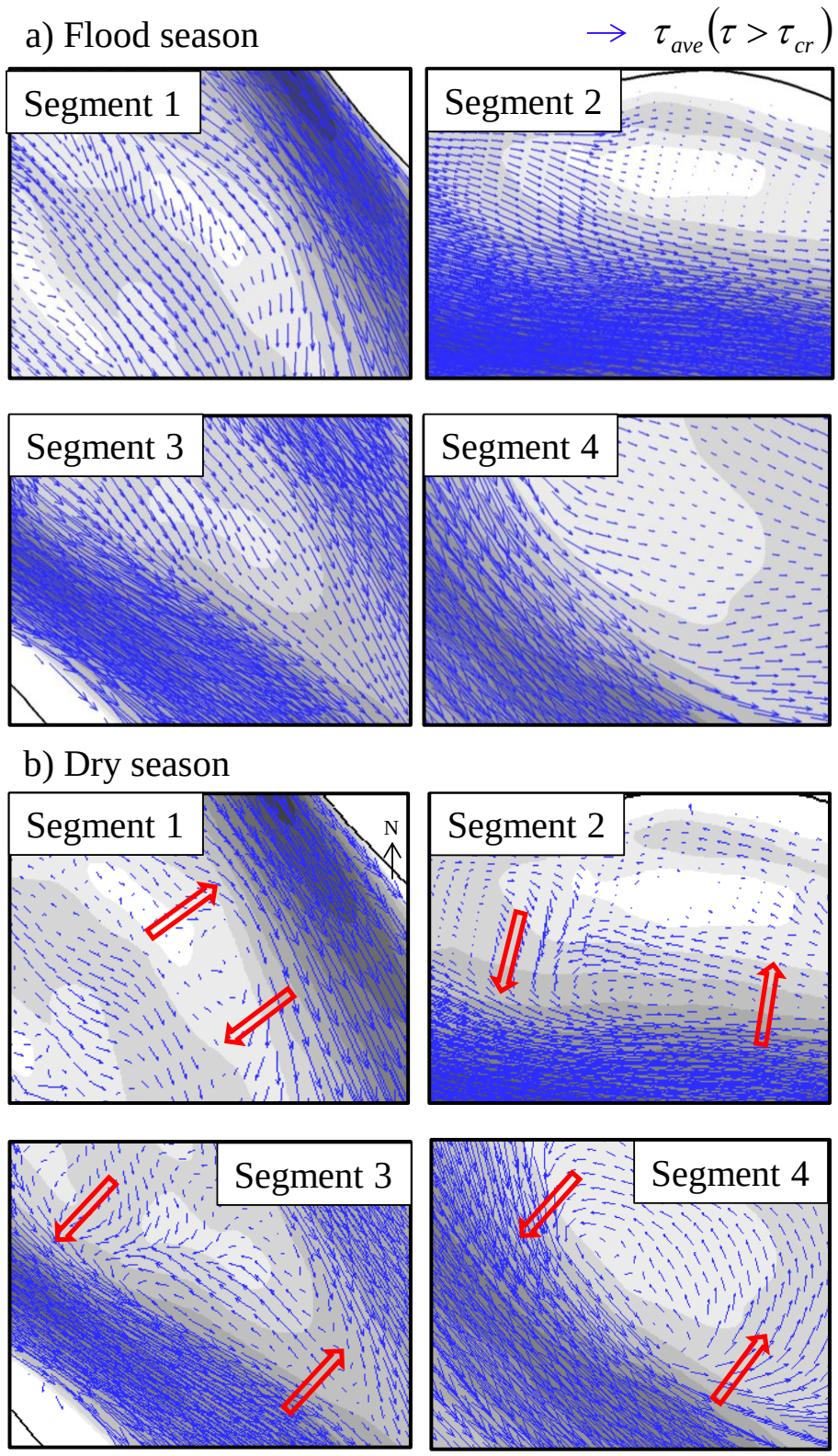

Figure 5.7 The average of effective shear stress in a tidal period a) flood season b) dry season

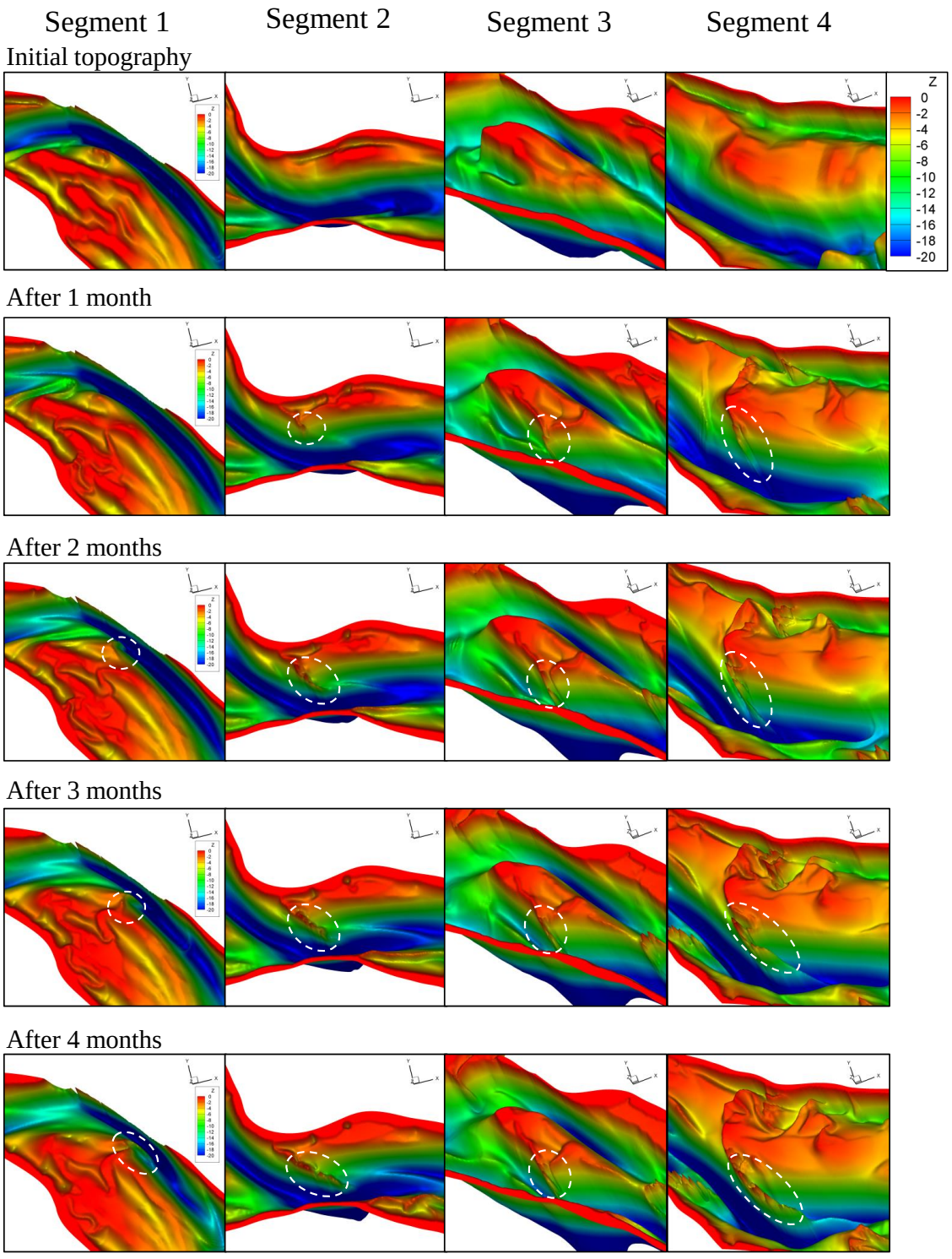

Figure 5.8 The topography change process at the 4 segments in dry season

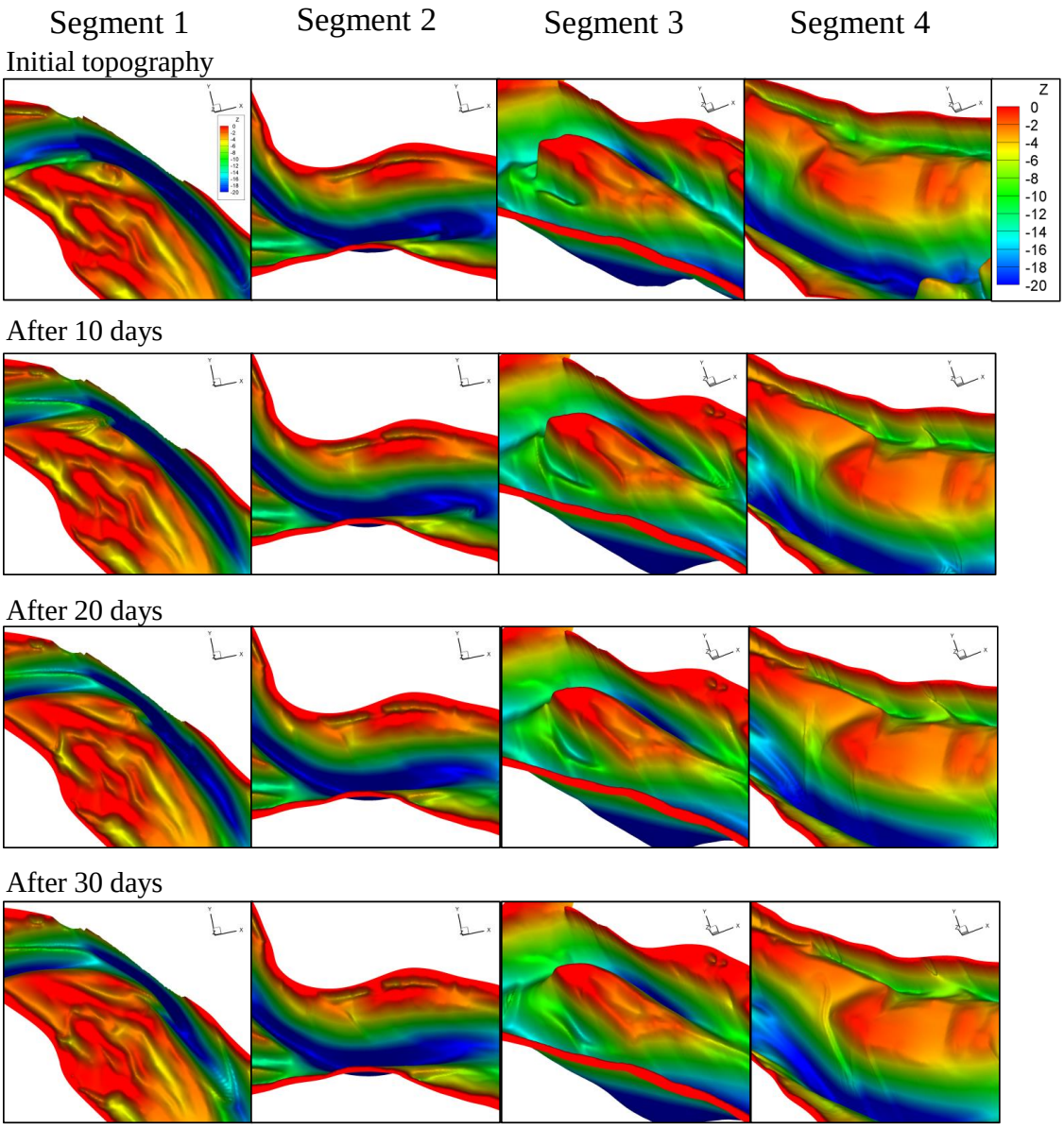

Figure 5.9 The topography change process at the 4 segments in flood season

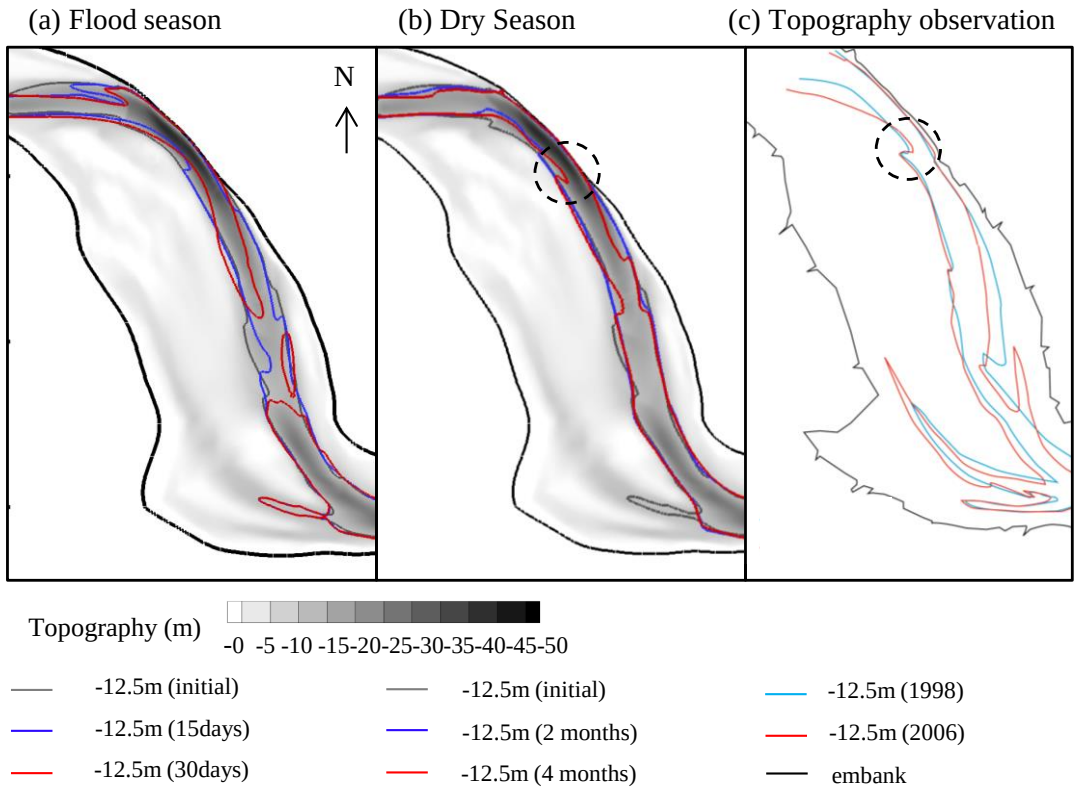

Figure 5.10 The topography change process and the observational record at Segment 1

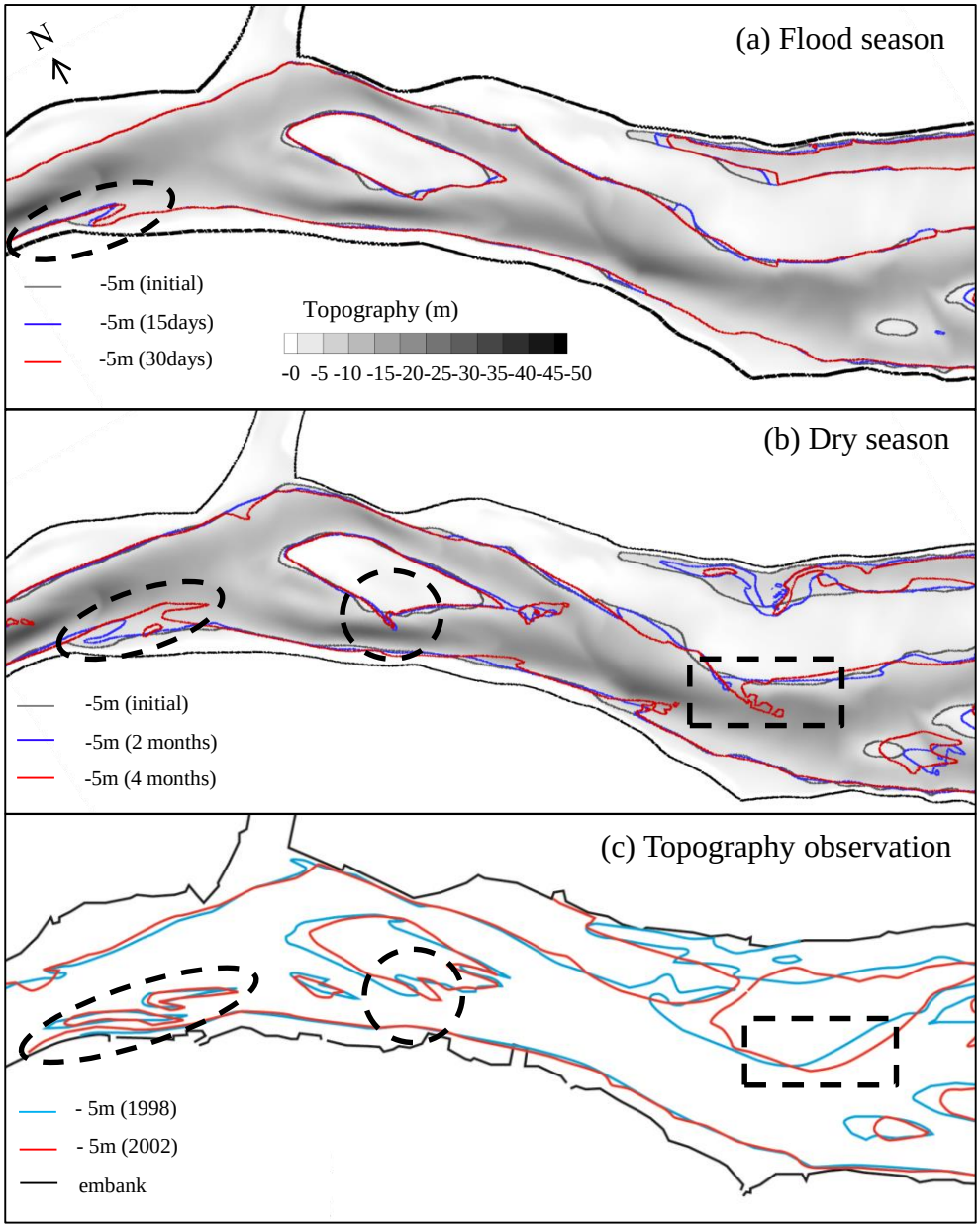

Figure 5.11 The topography change process and the observational record at Segment 3 and 4

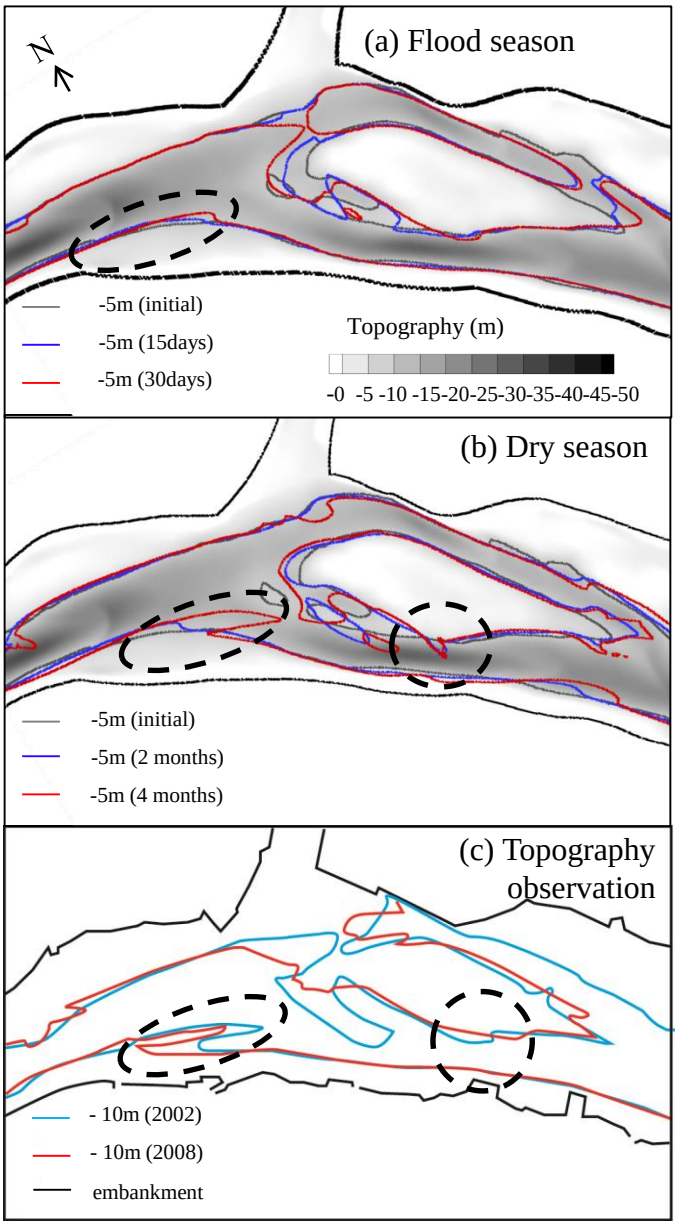

Figure 5.12 The topography change process and the observational record at Segment 3

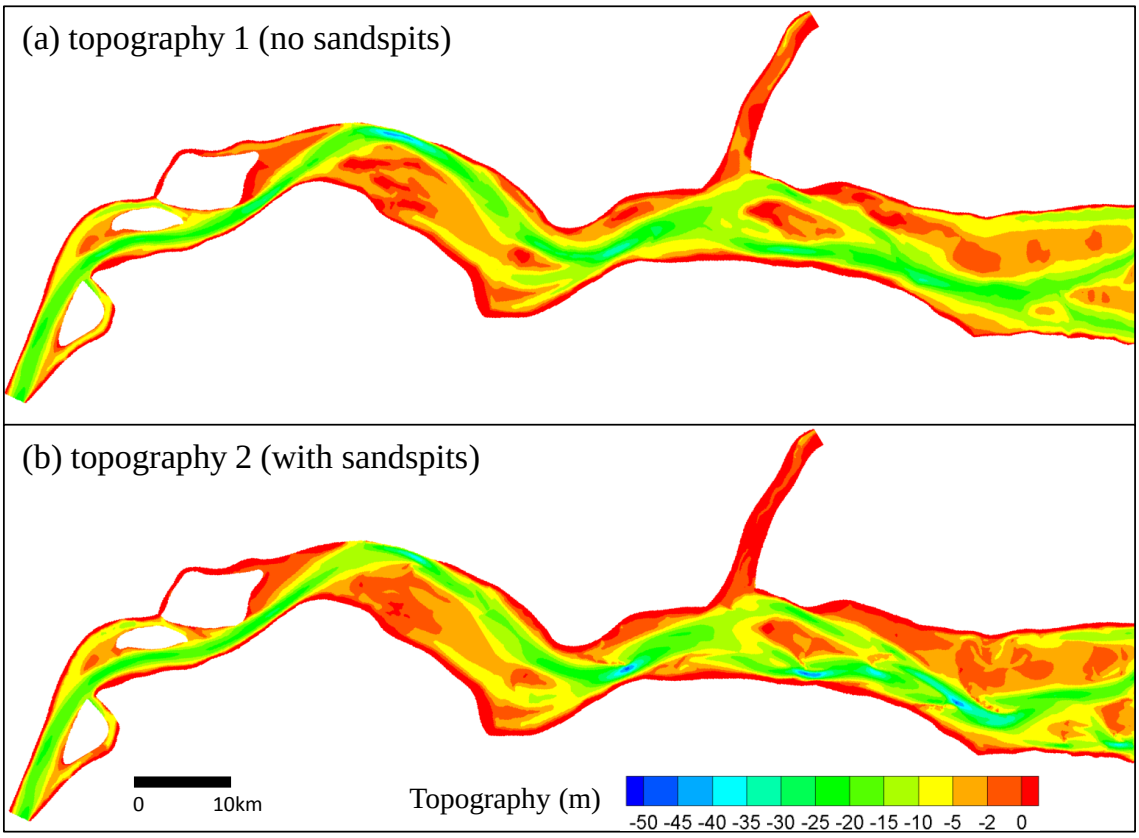

Figure 5.13 The initial topographies for topographic effect investigation (a) is the initial topography derived from the map digitization, with no existence of sandspits (b) is the topography after 4-month calculations for the dry season, several sandspits develop

(a) Segment 1

Before the development of sandspit

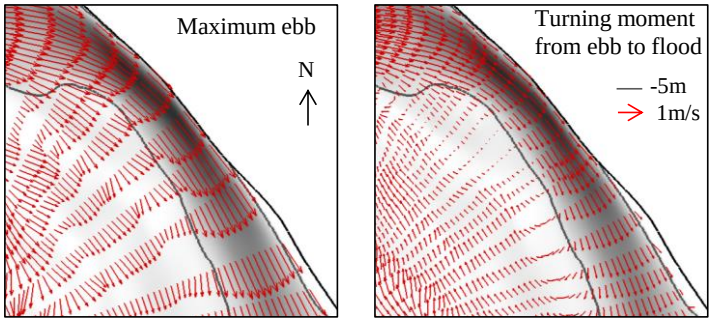

After the development of sandspit

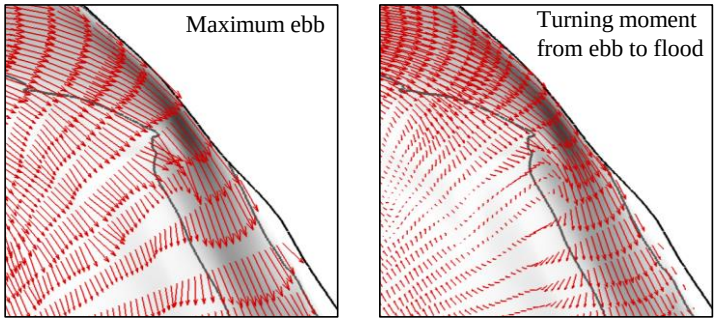

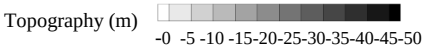

(b) Segment 2

Before the development of sandspit

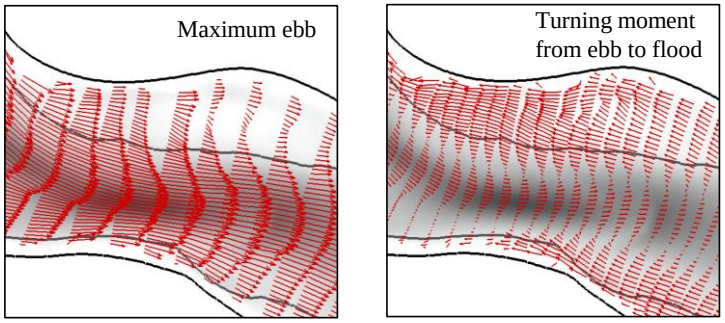

After the development of sandspit

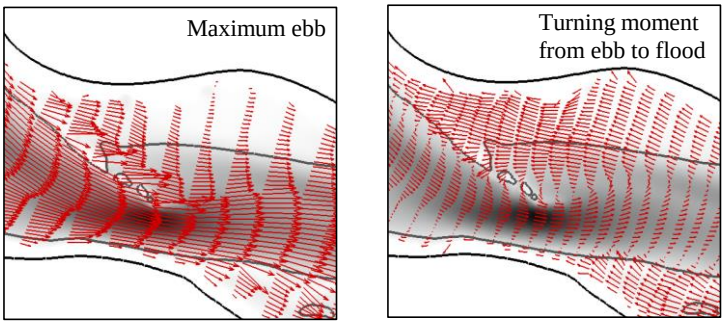

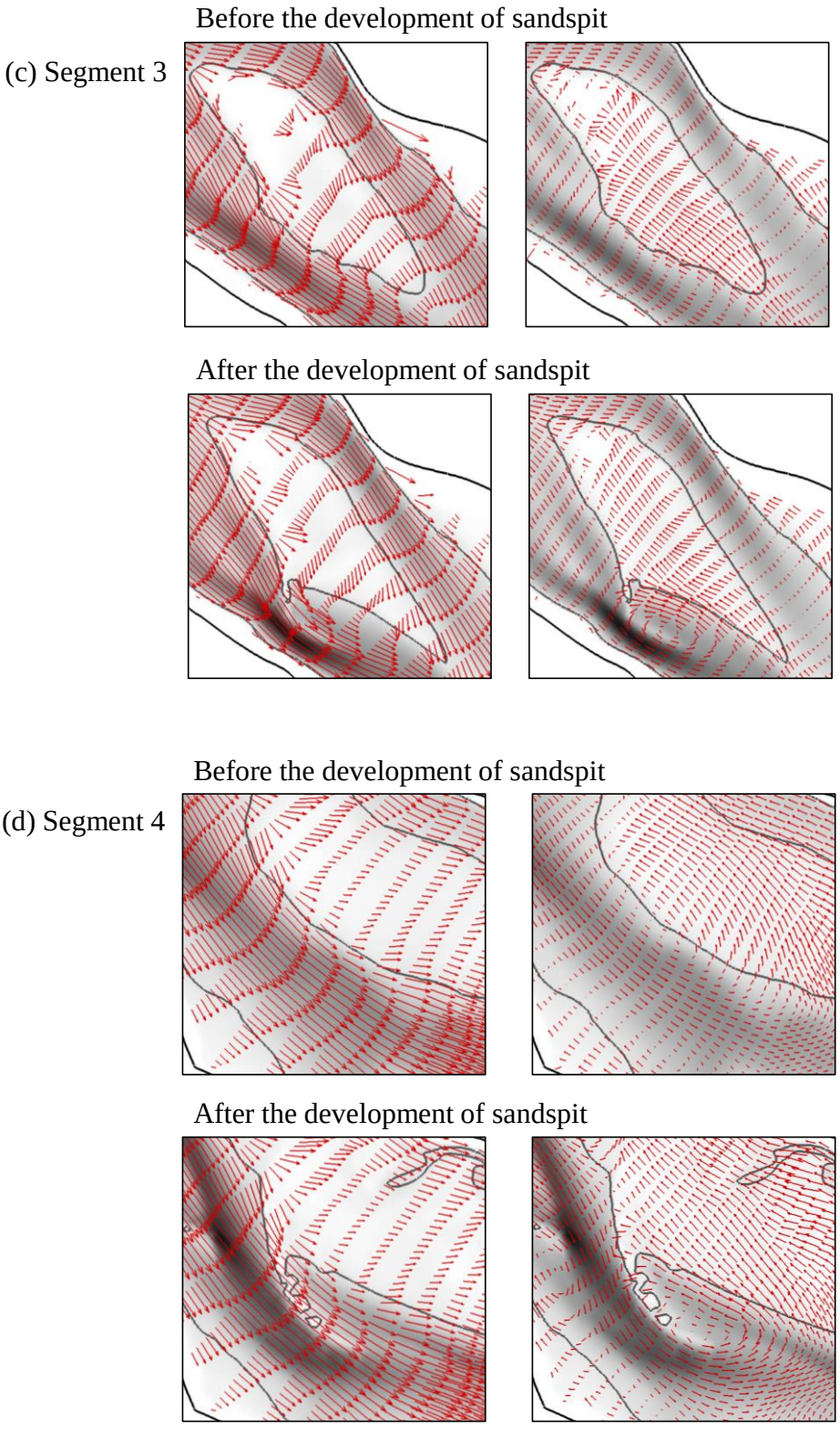

Figure 5.14 The comparison of flow velocity before and after the development of sandspits for 4 segments

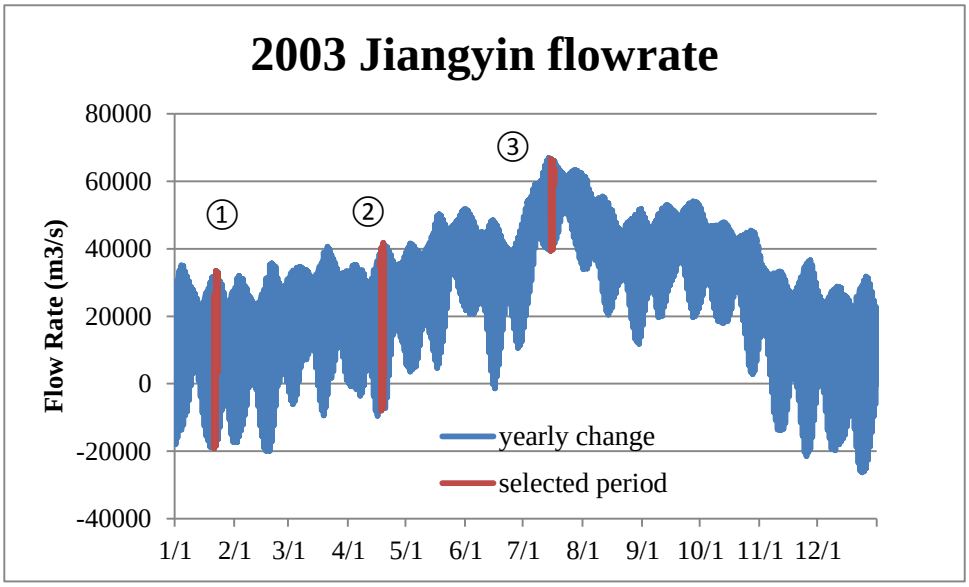

Figure 5.15 The selection for long-term topographic change calculation

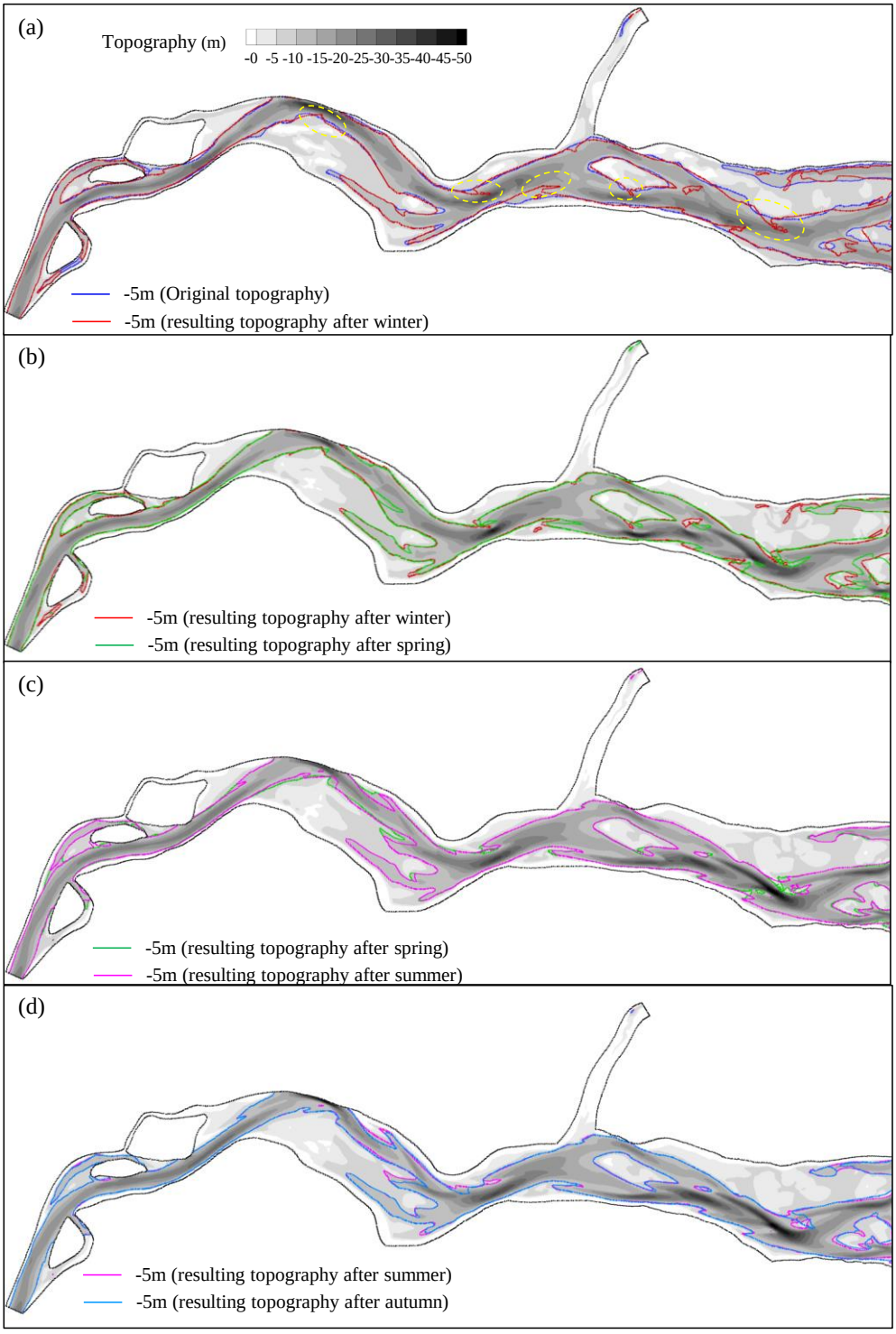

Figure 5.16 The calculation result of simplified yearly topographic change process. Each figure shows the topography at the beginning of a season by gray contour map. The lines show the -5m counter lines at the beginning and end of a season.

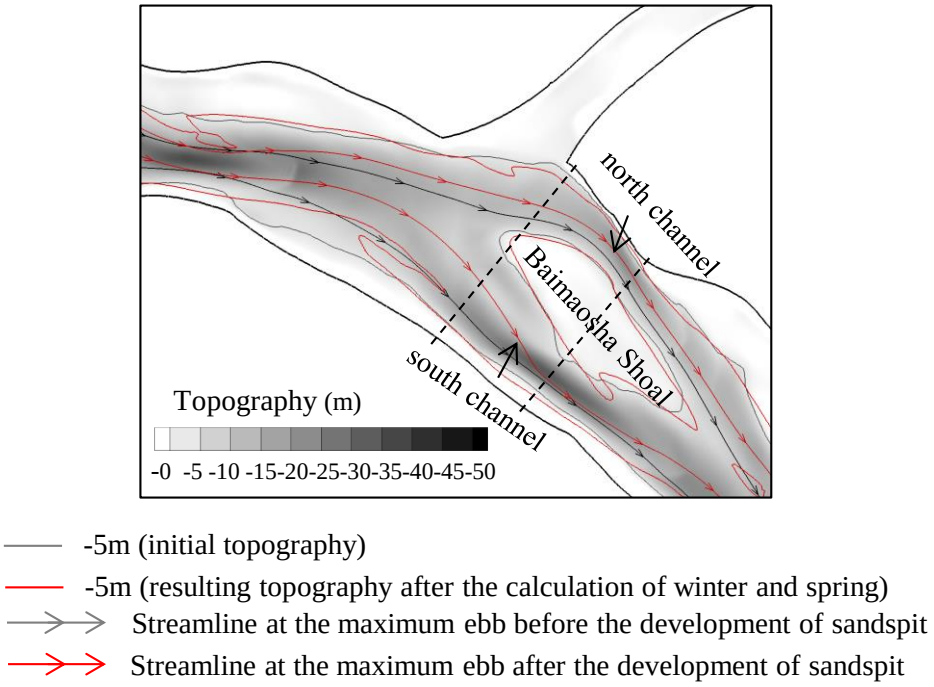

Figure 5.17 The stream line distribution at the maximum ebb before and after the development of sandspits at the location of between Segment 2 and 3

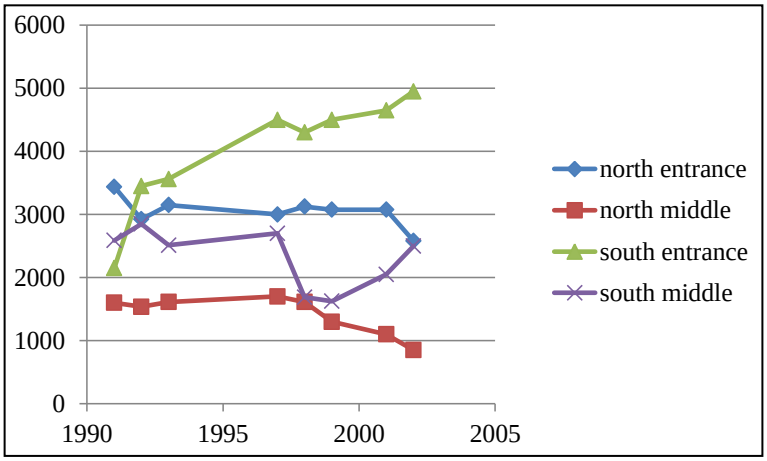

Figure 5.18 The channel width between -5m counter lines at the North and South channel at the sides of Baomaosha Shoal

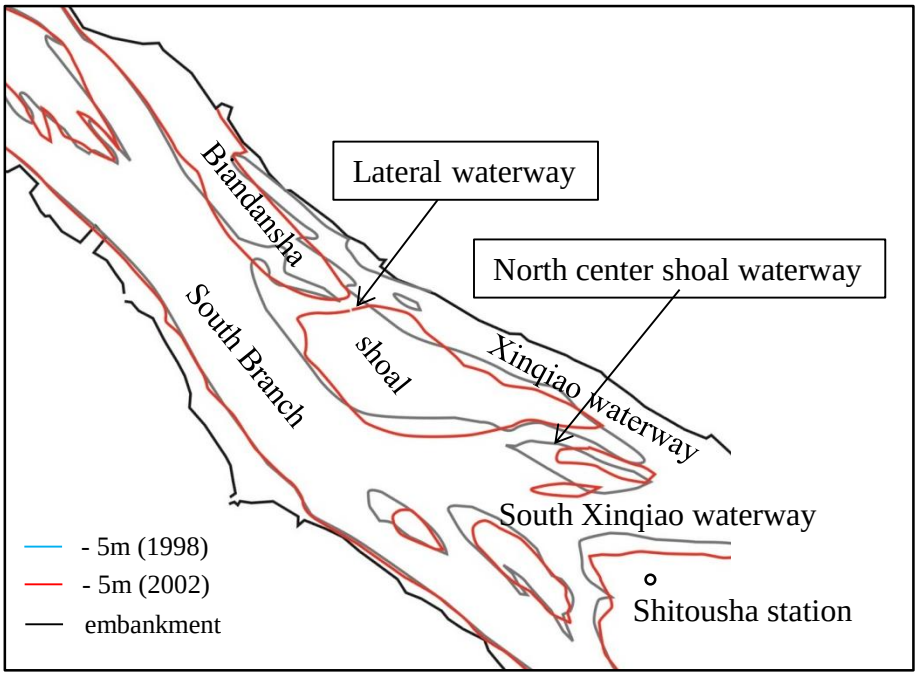

Figure 5.19 The location of the waterways on the Biandansha shoal

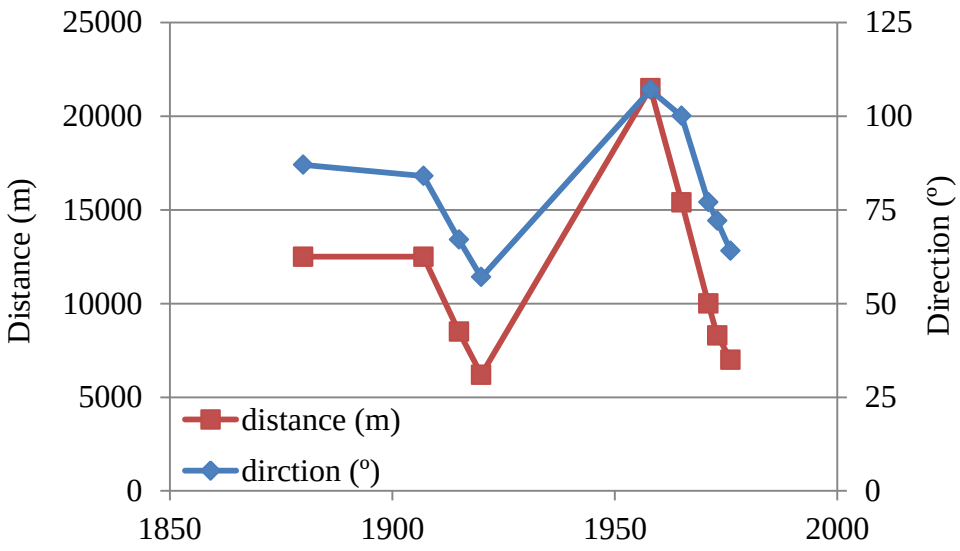

Figure 5.20 The distance between the entrance of the North center shoal waterway to the Shitousha station (red) and the angle between the North center shoal waterway and North direction (blue)

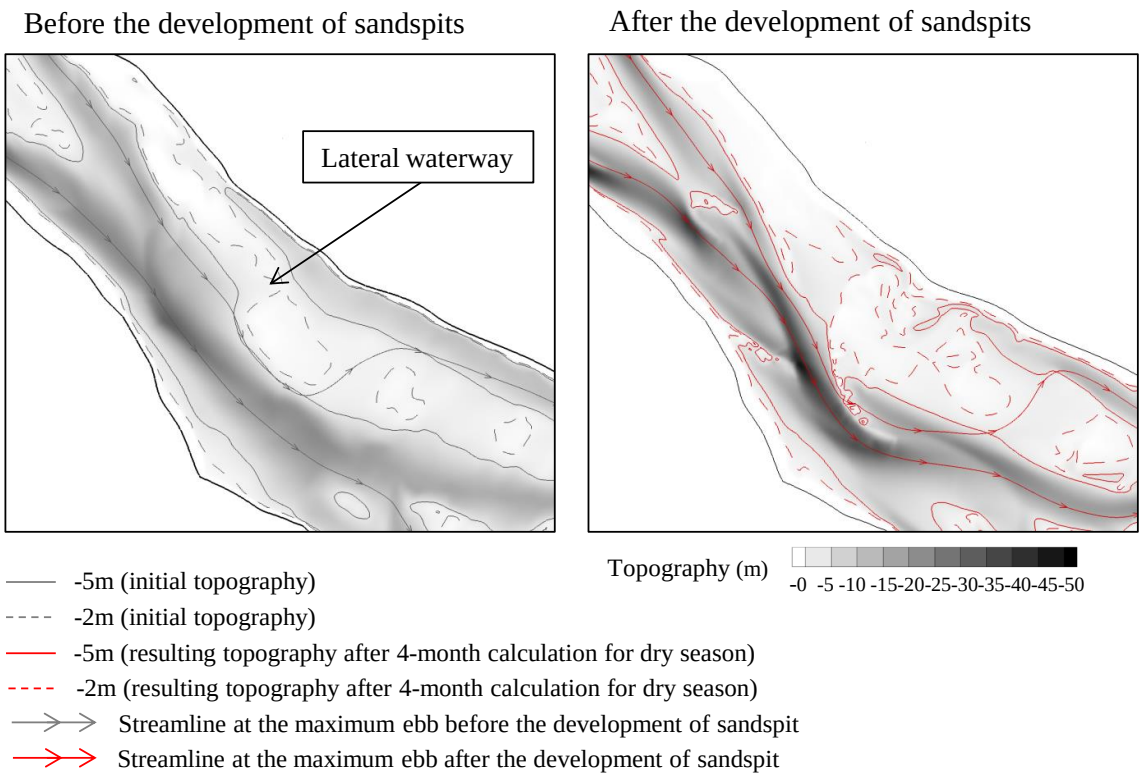

Figure 5.21 The stream line distribution at the maximum ebb before and after the development of sandspits at the location of between Segment 3 and 4

Chapter 6 Conclusions

6.1 Summery

In the present study, two control factors of tide and flow rate were investigated for their influence to the flow field and the resulting sediment transport process in the Yangtze Estuarine Channel by using numerical experiment. The study can be roughly divided into two parts. At first, a quasi-3D model was applied to investigate the minimum tidal effect in flood season. A tracer experiment was composed to the model to clarify the behavior of suspended sediment in a tidal period. Then, a 2DH model on the base of unstructured triangular mesh system was used to distinguish the seasonal characteristics of topographic change process. A simplified long-term calculation on topographic change was applied, and its results are compared to the historical evidences collected from references. The main conclusions are summarized as follows:

1) The numerical experiment is able to capture the characteristics of flow structures and sediment transport in the Yangtze Estuarine Channel. Due to the negligible density effect, the quasi-3D model and 2DH model can be applied in our study area. By the result of quasi-3D model, the secondary flow is not obvious due to the small ratio of depth/curvature, the flow structures in our study area can be roughly regarded as two-dimensional.
2) The lateral distribution of boundary conditions was discussed in our study area. The 20km from upstream end Jiangyin and 15km from downstream end Wusong were regarded influenced by the lateral distribution of flow rate and water level, respectively. The reach between them is believed to be stable.
3) The Yangtze Estuarine Channel is influenced by tide throughout a year. The flow field is highly pulsatile in the Yangtze Estuarine Channel. Simple oscillation occurs in thalweg while large cross-sectional component is observed above the underwater shoals.
4) During the flood season, the bed sediment is suspended in thalweg and transport to downstream in maximum ebb. The suspended sediment is dispersed onto the underwater shoals and deposit in high water slack when the flow is in stagnation. The meandering thalweg develops. During the dry season, due to the decrease of upstream water level, the

reverse slope oriented upstream was very large in flood tide period, inducing stronger landward flow and longer duration, especially above the underwater shoals.

5) During the dry season, the sediment transport is seaward in thalweg and landward above the underwater shoals. At the transition zone between thalweg and shoal, sandspits develop.
6) The sandspits continued to develop and move towards downstream during the subsequent seasons, which can also be observed at the nautical maps collected in references.
7) By comparison with historical records, the phenomena of topographic changes summarized by former researchers can also be explained by the development of sandspits, which infer the existence of sandspits may a key factor in the development in the Yangtze Estuarine Channel.

6.2 Future work

In the present study, in order to capture the main characteristic of flow structure and sediment transport, the calculation condition was simplified for the typical spring tide period during flood season and dry season. The period of neap tide is neglected for its potential small influence on flow structures and sediment transport. However, it may have its unique characteristics in topographic change process. The transitional period between flood season and dry season is similar. The sudden change in our simplified long-term calculation may ignore some interesting points including the development or degeneration of sandspits. Besides, the present study selected the year of 2003 for calculation, which represent a normal flood year. The peak flow rate record at Datong station is ~80000 m/s^3 in 1954, which is approximately 50% larger than the average value (55000 m/s^3). The influence for peak flow rate should be profound and it will take a long period to recover the topography. For the methodology, the uniform grain-size was used in our study for its easy condition control. The mixture-size sediment should also be taken into consideration, although it needs more observational data to support. The current study imply the small-scale sandspits may be the key factor in the topographic change process, the existence and its influence on flow structures need more evidence in field observation. The side-scan sonar and sub-bottom profiler should also be included to investigate the development

of sand wave due to active bed sediment movement. The asymmetry of sand wave is possible to be a good index to indicate the sediment transport direction.

Anyway, the present study provided a new explanation on the topographic change process in the Yangtze Estuarine Channel. Once the sandspits is confirmed by field observation, the control of them will become a simple and direct way to maintain the channel morphology in our study area, which will also become an efficient method for navigation channel management.

Acknowledgements

First and foremost, I would like to express my deepest gratitude to my supervisor, Professor Ishikawa for his guidance, support and encouragement throughout my study at Tokyo Institute of Technology. Numerous meetings and discussions are the origins of the research ideas and the directions of the way going forward. Without your guidance and persistent help, this dissertation would not be possible. Your attitude for the research will lead me further in my future career.

I would like to thank Dr. Nakamura and Dr. Kinouchi for their sincerely care to both my study and life. I am always encouraged by your refreshing thought and ideas provided in research seminars and other occasions. Your knowledge and virtue are always worthy of my respect.

Dr. Akoh and Dr. Yoshida really gave me great help when I first involved into the numerical calculation. I am grateful for your patience and tolerance in my model study and the subsequent analysis. Your assistance and friendship meant more to me than I could ever express.

I would also like to express my appreciation to all the members in Ishikawa Lab as well as Nakamura and Kinouchi Lab. Dr. Liu, Dr. Kojima, Dr. Kawachi and Dr. Minoura helped me overcome the most difficult time since I start my study in Japan. Dr. Liu and Dr. Xu always gave valuable advises in both study and life. Many thanks are given to Ms. Li, Ms. Lin, Mr. Zeng, Mr. Gao and other members in Ishikawa-Nakamura-Kinouchi Joint Lab for your encouragement, support and friendship during the study. The days with you is the most precious memory in my rest life.

Last but not least, I would like to thank my parents, my uncle, auntie and cousin for your continuous encouragement and care in my life. Endless love devote to my husband and baby boy. Your unconditional love and support inspire me to continue this journey. I hope this work will make you proud.